Middle East Journal of Science

Copyright © 2024

Hadice Budak GÜMGÜM
Field: Atomic and Molecular Physics, NMR Spectroscopy
(Prof.Dr., Dicle University, Faculty of Science, Dep. of Physics, TURKEY) hbudakg@gmail.com

Hüseyin ALKAN
Field: Protein Separation Techniques, Pharmacy
(Assoc.Prof.Dr., Dicle UniversityFaculty of Pharmacy, Department of Biochemistry, TURKEY)
mhalkan@dicle.edu.tr

Ishtiaq AHMAD
Field: Numerical Analysis, Computer Engineering
(PhD., Austrian Institute of Technology, Austria) ishtiaq.ahmad.fl@ait.ac.at

İlhan DAĞADUR
Field: Mathematics, Analysis and Functions Theory
(Prof.Dr., Mersin University Faculty of Arts and Sciences, Dep. of Mathematics, Turkey)
ilhandagdur@yahoo.com; idagadur@mersin@edu.tr

İsmail YENER
Field: Analytical Techniques, Pharmacy
(PhD., Dicle University, Faculty of Pharmacy, Department of Analytical Chemistry, Turkey)
ismail.yener@dicle.edu.tr

Javier FOMBONA
Field: Science Education
(Prof.Dr., University of Oviedo, Spain) fombona@uniovi.es

Jonnalagadda Venkateswara RAO
Field: Algebra, General Mathematics
(Prof.Dr., School of Science & Technology, United States International University, Nairobi, KENYA)
drjvenkateswararao@gmail.com

Lotfi BENSAHLA-TALET
Field: Ecology, Hydrobiology
(Assoc. Prof.Dr.,.Department of Biology, Faculty of Natural Sciences and Life, University Oran1-Ahmed
BENBELLA, Algeria) btlotfi1977@gmail.com

M.Aydın KETANİ
Field: Veterinary, Histology and Embryology
(Prof.Dr., Dicle University, Fac. of Veterinary, Dep. of Histology and Embryology, TURKEY)

Mohammad ASADI
Field: Agriculture, Entomology, Pesticides toxicology
(Dr., Department of Plant Protection, Faculty of Agriculture and Natural Resources,
University of Mohaghegh Ardabili, Ardabil, IRAN) assadi20@gmail.com

Mukadder İĞDİ ŞEN
Field: Astronautics Engineering
(Dr., Trakya University, Edirne Vocational College of Technical Sciences, Turkey)
mukaddersen@trakya.edu.tr

Murat AYDEMİR
Field: Inorganic Chemistry
(Prof.Dr., Dicle University, Faculty of Science, Dep. of Chemistry, TURKEY) aydemir@dicle.edu.tr

Murat HÜDAVERDİ
Field: High Energy and Plasma Physics
(Dr., Yıldız Technical University, Faculty of Science and Letters, Dep. of Physics, TURKEY) hudaverd@yildiz.edu.tr

Müge SAKAR
Field: General Mathematics
(Assoc.Prof.Dr., Dicle University, Turkey) mugesakar@hotmail.com

Mustafa AVCI
Field: General Mathematics
(Assoc.Prof.Dr., Batman University, Turkey) mustafa.avci@batman.edu.tr

Nuri ÜNAL
Field: High Energy and Plasma Physics
(Retired Prof.Dr., Akdeniz University, Faculty of Science, Turkey) nuriunal@akdeniz.edu.tr

Özlem GÜNEY
Field: Mathematics, Analysis and Functions Theory
(Prof.Dr., Dicle University, Faculty of Science, Dep. of Mathematics, Turkey) ozlemg@dicle.edu.tr

Petrica CRISTEA
Field: Computational Physics, Condenced Matter Physics, Electromagnetism
(Assoc.Prof.Dr., University of Bucharest, Faculty of Physics, Romania) pcristea@fizica.unibuc.ro

Sanaa M. AL-DELAIMY
Field: Atomic and Molecular Physics, General Physics
(Ph.D., Physics Department, Education College for Pure Sciences, Mosul University, Mosul, Iraq) sadelaimy@yahoo.com

Selahattin GÖNEN
Field: Physics Education, Science Education
(Prof.Dr., Dicle University, Faculty of Education, Turkey) sgonen@dicle.edu.tr

Şemsettin OSMANOĞLU
Field: Atomic and Molecular Physics, ESR Spectroscopy
(Retired Prof.Dr., Dicle University, Faculty of Science, Dep. of Physics) sems@dicle.edu.tr

Sezai ASUBAY
Field: Solid State Physics
(Prof.Dr., Dicle University, Faculty of Science, Dep. of Physics, Turkey) sezai.asubay@gmail.com

Süleyman DAŞDAĞ
Field: Biophysics
(Prof.Dr., İstanbul Medeniyet University, Faculty of Medicine, Dep. of Biophysics, Turkey) sdasdag@gmail.com

Tamraz H. TAMRAZOV
Field: Biological Sciences
(Assoc.Prof.Dr., Department of Plant Physiology and Biotechnology, Research Institute of Crop Husbandry, Ministry of Agriculture of the Republic of Azerbaijan)
tamraz.tamrazov@mail.ru

Yusuf ZEREN

Field: Mathematics, Topology

(Assoc.Prof.Dr., Yıldız Technical University, Faculty of Science and Letters, Dep. of Mathematics, TURKEY)

yzeren@yildiz.edu.tr

Z. Gökay KAYNAK

Field: Nuclear Physics

(Retired Prof.Dr., Uludag University, Faculty of Science, Dep. of Physics, Turkey) kaynak@uludag.edu.tr

CONTENTS

Middle East Journal of Science

Research Article

PHYTOCHEMICAL PROFILING BY LC-ESI-MS/MS AND DETERMINATION OF ANTIOXIDANT, ANTI-ALZHEIMER AND ANTITYROSINASE ACTIVITIES OF TWO ASPARAGACEAE SPECIES: *Scilla hyacinthoides* L. AND *Scilla ingridiae* SPETA

Alevcan KAPLAN[1]

[1]Department of Crop and Animal Production, Sason Vocational School, Batman University, Batman, Türkiye
*Corresponding author's e-mail:kaplanalevcan@gmail.com

Abstract: *In this study, in vitro antioxidant, antialzheimer and antityrosinase activity, total phenolic and flavonoid components, phytochemical profiling, identified by Liquid chromatography-electrospray ionization-mass spectrometry (LC-ESI-MS/MS) analysis and also chemometric analysis, of two different parts of Scilla species (Scilla hyacinthoides L. and Scilla ingridiae Speta) were determined in detailed perspective. The highest contents of total phenolics (TPC) and total flavonoids (TFC) were determined in S1TU (S. hyacinthoides aerial parts) extract (11.72±0.00 µg GAE/mg) and S2TU (S. ingridiae aerial parts) extract (31.53±0.21 µg QE/mg). The highest ABTS and CUPRAC activities were found in S1TU and S2TU extracts. The inhibitory activities of the extracts on the enzyme acetylcholinesterase were investigated. S1TU and S2TU extracts again showed the highest activity. Although the antityrosinase enzyme inhibitory activities of the extracts were generally similar and high, the S2TA extract (S. ingridiae corm parts) showed the highest activity. LC-ESI-MS/MS was used to determine the content of phenolic components of the extracts. Fourteen different bioactive components were determined in the analyzes and their amounts were measured. The data obtained were analyzed chemometrically such as principal component analysis (PCA), hierarchical component analysis (HCA) and their relationships to each other were supported visually and numerically with Pearson correlation graphs, heat maps, etc. The research results have shown that the various components of the plant have a good effect on various biological activities, so that it can be used for various purposes in the future (especially with a good degree of antityrosinase activity), taking into account the results. The biological activities demonstrated here can rationalize the use of the plant in traditional medicine.*

Key words: *Antioxidant activity, enzyme inhibition, multivariate analysis, Pearson correlation, phytochemical profiling*

1. Introduction

The concept of herbal medicine is defined as "botany or phytotherapy" and refers to the use of biological material containing parts of a plant, such as seeds, fruits, leaves, bulbs, tubers, roots, bark or flowers, for medicinal purposes, where the different parts of a plant are used individually or in combination and sold as various shape (tablets, capsules, powders, teas, extracts, and fresh or dried plants). People use conventional herbal products to maintain or develop their health [1]. Products made from herbal substances that are used to protect or promote health may be referred to as herbal products, or herbal medicines. Herbal treatments can be used as personal care medicine in cases such as sleep, flu and psychological disorders, digestive disorders, flu infections and stress. Traditional herbal medicines are also used to treat irritable bowel syndrome, eczema, premenstrual syndrome,

migraines, menopausal symptoms, rheumatoid arthritis, chronic fatigue syndrome, asthma, and cancer. Herbal complements are best taken under the advice of a trained healthcare provider. A study mentions that 90% of arthritis patients are treated with alternative treatments such as herbal medicines [2]. In the medical world, medicinal plants are now recognized as a complementary treatment method. This shift in opinion has not only increased the use of herbal medicines, but has also contributed to an increase in pharmacological and toxicological research on herbal medicines to prove their efficacy [3].

Throughout their lives, all plants synthesize various chemical compounds as an indispensable part of their normal metabolic activities. Primary metabolites consist of macromolecules such as proteins, fats, sugars and carbohydrates, which are found in all plant organisms. Primary metabolites play an important role in vital functions such as metabolism, reproduction and growth. SM*s* (secondary metabolites) are a group of biosynthetically produced primary metabolites that occur in a small number of plants and fulfill a more vital function, mainly phenolic compounds, alkaloids, terpenes, steroids and derivatives of sulfur compounds. Secondary metabolites play a more important role in protecting and maintaining health, such as toxins to deter predators and pheromones that attract insects for pollination [4-6]. Some types of secondary compounds that are particularly important in pharmacy today are thought to have hypolipidemic, antioxidant, hypoglycemic, and anti-inflammatory effects. In addition, some secondary compounds are also said to protect against thrombosis and cancer. Due to these properties, it is assumed that phytochemicals can protect against some diseases such as obesity, diabetes, metabolic syndrome, dyslipidemia, cardiovascular diseases and cancer [6].

The genus *Scilla* is exemplified by 14 taxa in Türkiye [7-9]. The pharmacopoeias of many countries list the uses of the corms; for example, the corms of this genus (*Scillae* corms) are used for their diuretic and cardiotonic features [10, 11]. The literature search revealed that only a few studies have been conducted on the species growing in Türkiye. The literature search revealed that few studies have been conducted on the species growing in Türkiye. Tanış [12] investigated the antioxidant capacity of *Scilla bifolia* L., Aktepe et al. [13] investigated the biochemical constituents, enzyme inhibition properties, antioxidant and antimicrobial properties of endemic *Scilla mesopotamica* Speta. Coşkun [14] conducted studies on the reproductive biology of *Scilla autumnalis* L. and obtained valuable results. Considering the prepotency of medicinal plants and the rare chemical and biological investigation of these species, this study was essential.

The sole aim of this work was to explore the phytochemical constituents of the species *S. hyacinthoides* and *S. ingridiae*, to show their biological capabilities, to explain them with chemometric approaches, to model them with correlation methods and to present them to scientists working in different disciplines. On the other hand, this study is also significant in many ways with respect to the species and parameters studied.

2. Materials and Methods

2.1. Plant Materials

S. hyacinthoides was collected in an oak area along the 40. km Hani road in Diyarbakır (26.05.2023). *S. ingridiae* was collected in a mountainous area in Sason district in Batman (06.05.2023). The plants was assigned by Dr. Alevcan Kaplan and provided with voucher specimens Batman 2023/27 and Batman 2023/28, which are kept at Batman University.

2.2. Preparation of Plant Extracts for Biological Activity and Phytochemical Profiling

The species collected in the field were separated into aerial parts and corms and dried in an airy room protected from sunlight. The corms were cut in half and dried to prevent mold growth. The dried plants were then cut into small pieces, weighed and coded according to the plant parts. The aerial parts

(flowers, stems, and leaves) of the species *S. hyacinthoides* were labeled with S1TU, the corms with S1T2, the aerial parts of the species *S. ingridiae* with S2TU and the corms with S2TA. Then the plant parts were weighed, briefly, S1TU-63 g, S1TA-87.1 g and S2TU-25 g, S2TA 23.5 g were weighed and extraction procedures were performed with ethanol, the solvents were evaporated until the plants were completely dried under the fume hood to ensure that there was no solvent left in the plants. Finally, the tares of the dried extracts were taken and the % (percentage) yield was calculated. The extracts were stored in closed containers until analysis.

2.3. Phytochemical Profiling via LC-ESI-MS/MS Methods

The LC-ESI-MS/MS method was used to analyze the phytochemical constituents of the plants. A previously ingrained and developed LC-ESI-MS/MS method was used to identify the phenolic content of *Scilla* species in the study [15].

2.4. Evaluation of TPC and TFC Contents

The TPC of plants was expressed as pyrocatechol and TFC content or quercetin equivalent [16-18]. The following equations were used to calculate the TPC and TFC of the extracts:

PE*s*. pyrocatechol equivalents (Absorbance = 0.032x + 0.0445 pyrocatechol (µg)   (R^2 = 0.9947)

QEs. quercetin equivalents (Absorbance = 0.0288x + 0.0352 quercetin (µg)   (R^2 = 0.9951)

2.5. Antioxidant Activity

To appraise the antioxidant activity of the extracts, the methods of the radical scavenger DPPH and the ABTS cation radical scavenger as well as the reducing antioxidant capacity of copper (CUPRAC) were used [19-22].

2.6. Anticholinesterase Inhibiton Activity

A spectrophotometric method improved by Ellman et al. [23] was used to determine the acetyl and butyryl cholinesterase inhibitory activities.

2.7. Tyrosinase Inhibiton Activity

The tyrosinase inhibition experiments were conducted according to the protocol of Hearing and Jiménez [24].

2.8. Chemometric and Statistical Analysis

Chemometrics is essentially the statistical analysis of data obtained through chemical processes. Multivariate data analyzes are processed and interpreted using chemometric algorithms [25]. To perform chemometric analyzes, the results obtained from the experiments were transferred to programs such as OriginPro 2024b Academic edition, Graphad Prism 5, and Xlstat 2024 after their calculation and the data were analyzed. The results of TPC and TFC, antioxidant, tyrosinase inhibitory and anticholinesterase activities were expressed as mean values ± S.E (standard error). The outcomes were analyzed using an unpaired *t*-test and one-way analysis of variance ANOVA. Differences were considered statistically significant at $p < 0.05$.

3. Results and Discussion

For a thousand of years, nature has been the source of medicines, and an astonishing number of modern treatments have been defined from natural sources. Most of plants have long been used as herbal folk remedies to treat different conditions, and their diverse NP*s* have inspired the improvement of new medicines. With the discovery of new molecular targets (MT*s*) based on proteins, the need for new structural and chemical diversification in screening is growing. NP*s* will play a critical role in meeting this need through the continued detection of the world's biodiversity, much of which remains undiscovered. While drug development from medicinal plants (MP*s*) remains an significant source of new therapeutics, there are several obstacles, including defining and conducting appropriate HTS (high-throughput screening) experiments, increasing the supply of biologically active molecules and sourcing plant material. Exploration of these natural resources requires multidisciplinary, nationwide and international partnerships in many process (synthesis, discovery, and design drug) improvement practices [26]. Such studies are innovative and intriguing given the strategies to incorporate the therapeutic agents use of plant NP*s* worldwide to support future drug exploration from plant sources [26].

In this regard, the phytochemical components and biological abilities of the species with the common names "dağ soğanı" (*S. hyacinthoides*) and "ala sümbül" (*S. ingridiae*) in Türkiye were studied and evaluated. First, the efficacy of solvent on extraction yield was investigated. The effect of solvent on the percentage yield is shown in Table 1, Figure 1, and Figure 2. The highest yield was found to be 4.77 % for S2TA. The other tree extracts showed almost similar percentage yields. Extraction is the most important step to obtain and isolate bioactive phytochemicals from different plant materials. The extraction adequacy is affected by the chemical nature of the phytochemicals, the extraction technique used, the particle size of the sample, the solvent used and the presence of solvent-insoluble substances. The extraction efficiency depends on the polarity of the solvent, pressure, extraction method, T °C (temperature), E_t (extraction time), pH, and combination of the sample [27-29]. Aydın et al. [30] documented that the yield of methanol extracts from tuber, leaf and flower of *Scilla siberica* subsp. *armena* (Grossh.) Mordak species were 1.27 g, 1.80 g and 1.04 g, respectively. Mulholland et al. [31] extracted the species *Scilla zebrina* Baker with dicholoromethane and reported an extraction yield of 7.28 g. Yaman et al. [29] assumed that the variations in extract yield were due to differences in species, location, harvest time and extraction methods.

Table 1. Effect of solvent types on extract yield of two *Scilla* species

Plant samples	Extraction yield (%)
S1TU	3.28±0.3
S1TA	3.22±0.09
S2TU	3.06±0.12
S2TA	4.77±0.29

[†]It indicates the mean value and standard deviation
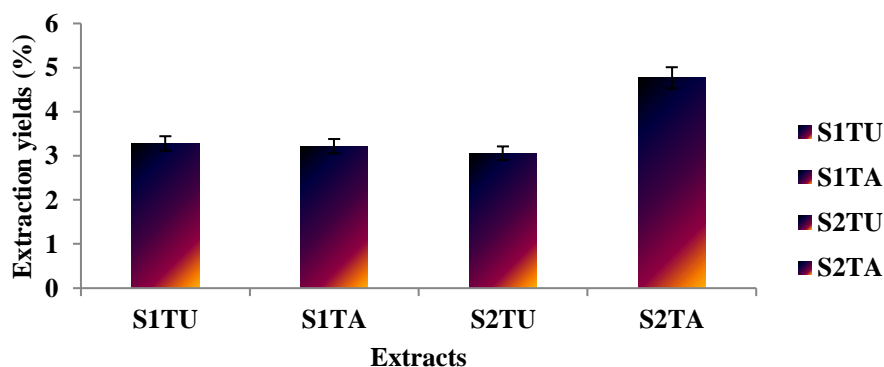
Figure 1. Extraction yields of two *Scilla* species
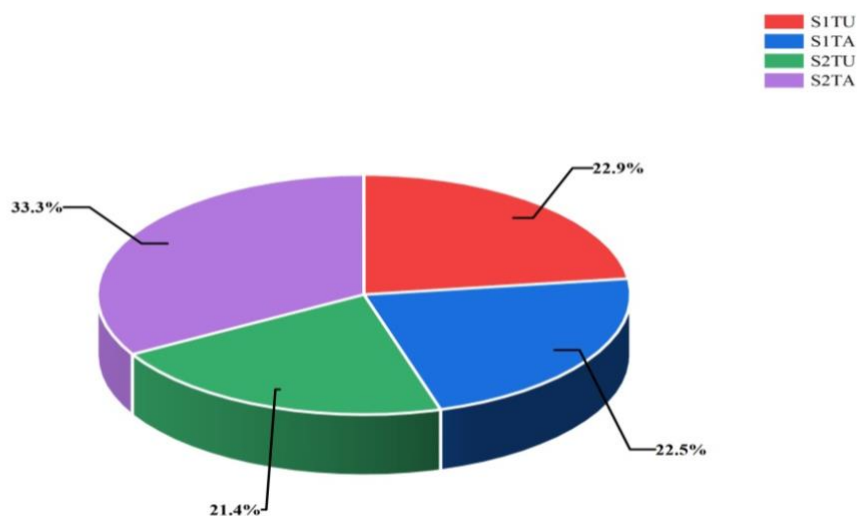
Figure 2. Visualization of % yields of extracts of two different *Scilla* species with pie chart

For the identification, pathological characteristics analysis and remedy of numerous diseases, sensitive and specific methods are required for the determination and characterization of endogenous level of these steroids in body tissues or, fluids as well as for their quantification and content in phytochemical analyses. More recently, LC-ESI-MS/MS has gained acceptance for these objectives due to its specificity and sophistication [32]. The chromatograms of the phytochemical constituents are shown in Figure 3. The content and amounts of these phytochemicals are summarized in Table 2. The correlations of the phytochemicals with each other are shown in Figure 4, and the correlations of the extracts with each other according to their content are depicted in Figure 5. As can be clearly shown in Table 2, a total of 14 phytochemicals were identified. The number of ingredients was determined as follows: S1TU (n=13), S2TA (n=12), S1TA = S2TU (n=11), from most to least. It can be said that the most important chemical compound is vanillic acid (VA). However, the S1TU extract contains shikimic acid, which is not present in the other extracts and not in this quantity. VA (4-hydroxy-3-methoxybenzoic acid) is a derivative of hydroxybenzoic acid, which is mainly used as a flavouring agent. It is also formed as an intermediate in the production of vanillin from ferulic acid [33,34]. In addition to its use as a food additive, it is thought to have anticoagulant, antioxidant, antimicrobial, antioxidant, anti-inflammatory, anti-venous, cardioprotective, hepatoprotective and neuroprotective effects, as well as anti-inflammatory effects by lowering the pain threshold [34-37]. In addition, VA has also been used in wound healing by suppressing the expression of MITF (microphthalmia-associated transcription factor) and melanogenic enzyme sinB16F10 in cells and decreasing melanin

levels and tyrosinase activity with or without MSH (melanocyte-stimulating hormone) stimulation [38,39]. It also inhibited inflammatory pain by activating nuclear factor Kappa B (NF-κB) and inhibiting cytokine production, oxidative stress, and neutrophil recruitment [39,40]. Vanillic acid also showed anti-cancer effects by inhibiting tumor growth. It treated acute myocardial injury by hypoxia/reoxygenation by reducing oxidative stress of H9c2 cells [39, 41]. It also controlled lipopolysaccharide-induced neurotoxicity in mice by regulating c-Jun N-terminal kinase in the brain [36, 39]. SA (shikimic acid) is properly distributed in many herbal species and is known to exhibit various bioactivities, including antioxidant, analgesic, anti-inflammatory, and antithrombotic effects as well as activities against biofilms [42, 43]. The richness of the species in such valuable secondary metabolites confirms the parameters of the study. To look at the data obtained in the study from a different angle and to civilize the data, the heat map was created using the Pearson correlation matrix and shown in Figure 3. There is a strong positive correlation between protocatechuic acid and hydroxybenzaldehyde, vanillic acid, caffeic acid, syringic acid, protocatechuic acid ethyl ester and naringenin. With the exception of chlorogenic acid and shikimic and trans-cinnamic acid, moderate correlations were generally observed. there is a strong positive correlation between hydroxybenzaldehyde and protocatechuic acid, vanillic acid, caffeic acid, syringic acid, protocatechuic acid ethyl ester and naringenin. there is a strong positive correlation between vanillic acid and protocatechuic acid, hydroxybenzaldehyde, caffeic acid, syringic acid, protocatechuic acid ethyl ester and naringenin. there is a strong positive correlation between *p*-coumaric acid and vanillin and salicylic acid. there is a strong positive correlation between salicylic acid and *p*-coumaric acid, vanillin. Scutellarin showed a close to strong to moderate correlation with chlorogenic acid. there is a strong positive correlation between protocatechuic acid ethyl ester and protocatechuic acid, hydroxybenzaldehyde and protocatechuic acid, vanillic acid, caffeic acid, syringic acid and naringenin. a moderate to strong correlation exists only between *trans*-cinnamic acid and vanillin. A strong correlation was found between naringenin and protocatechuic acid, protocatechuic acid, vanillic acid, caffeic acid, syringic acid and protocatechuic acid ethyl ester. Surprisingly, protocatechuic acid, hydroxybenzaldehyde, vanillic acid, protocatechuic acid ethyl ester and naringenin always showed a high correlation with each other. This correlation suggests that they may play a common role in the biological activities of the plant. Aktepe et al. [13] detected chicory (0.564 µg/mL), transferulic acid (0.501 µg/mL), caffeic acid (0.165 µg/mL) and chlorogenic acid in the chloroform extract as a result of LC-MS/MS analysis of *S. mesopotamica*. They found that the levels (0.158 µg/mL) were again quite high compared to other extracts. The same researcher found from the LC-MS/MS results that the amounts of caffeic acid, *p*-coumaric acid, transferferulic acid, kaempferol and gentisic acid in the ethyl acetate extract were quite high (1.933 µg/mL, 0.301 µg/mL, 0.295 µg/mL, 0.229 µg/mL, and 0.162 µg/mL, respectively). However, the LC-MS/MS results of the methanol extract of *S. mesopotamica* Speta showed high levels of chichoric acid, vanillic acid, chlorogenic acid and citric acid (0.559 µg/mL, 0.228 µg/mL, 0.159 µg/mL and 0.111 µg/mL), ascorbic acid, 4-hydroxybenzoic acid, epicatechin, transferulic acid, fumaric acid and catechin were lower (0.08 µg/mL, 0.052 µg/mL, 0.047 µg/mL, 0.047 µg/mL, 0.041 µg/mL, 0.037 µg/mL, and 0.036 µg/mL, respectively) [13]. These results show that plants, even if they belong to the same genus, can synthesize many different bioactive secondary metabolites. Figure 5 shows the evaluation of the extracts in terms of their content. In this respect, a strong correlation was found between S2TU and S1TA, between S1TA and S1TU and a moderately positive correlation between S2TA and S2TU. This can also be seen as an indicator of the parallelism between the ingredients and the extract results.
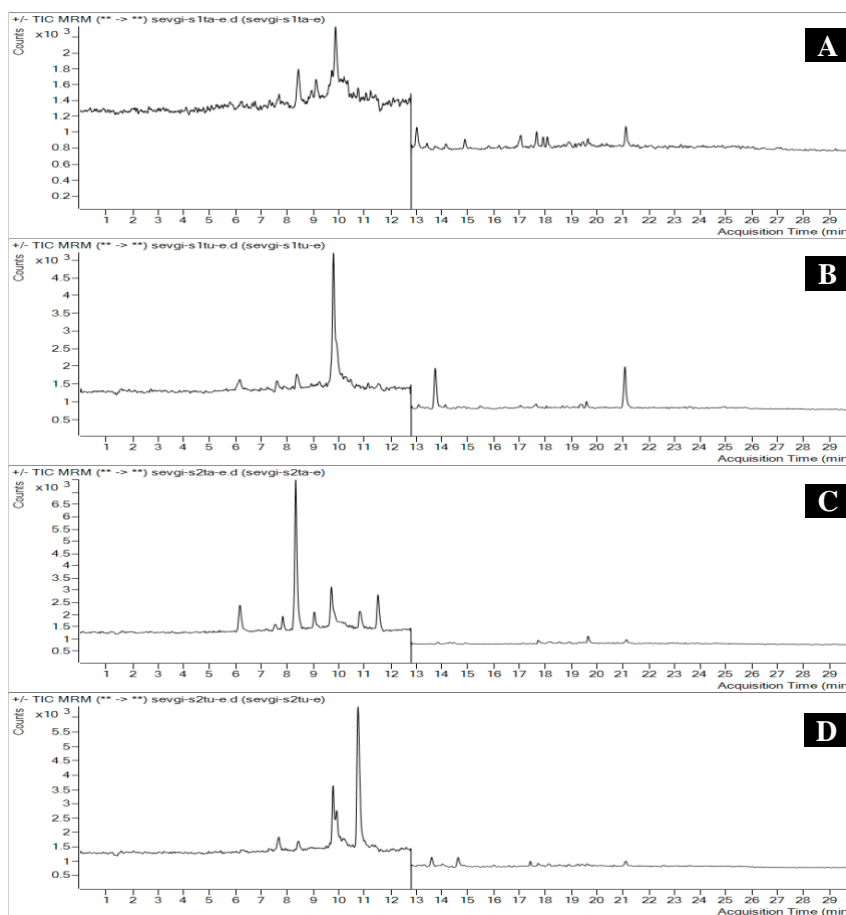
Figure 3. Overlapped two *Scilla* species extract samples chromatogram from LC-ESI-MS/MS analysis, **A-**S1TA, **B-**S1TU, **C-**S2TA, **D-**S2TU

Table 2. LC- ESI-MS/MS profiling of two different parts of two different *Scilla* species

Analytes	RT (min.)	R²	Quantitative results (ng analyte/mL extract)			
			S1TA	S1TU	S2TA	S2TU
Shikimic acid	1.53	0.99	n.d	**841.9**	n.d	n.d
Protocatechuic acid	6.30	0.99	7.1	40.2	141.7	9.5
Chlorogenic acid	7.93	0.99	7.0	9.1	13.2	13.9
Hydroxybenzaldeyde	8.40	0.99	13.0	13.7	32.7	16.4
Vanillic acid	7.95	0.99	**325.1**	**285.5**	**3709.4**	**205.3**
Caffeic Acid	8.45	0.99	29.8	18.4	473.9	12.4
Syringic acid	9.12	0.99	18.8	12.4	30.3	14.2
Vanillin	9.72	0.99	10.8	104.6	45.7	54.2
p-coumaric acid	9.89	0.99	136.8	161.7	151.3	162.3
Salicylic acid	10.21	0.99	61.4	148.6	126.2	127.7
Scutellarin	10.68	0.99	0.4	0.5	16.7	114.8
Protocatehuic ethyl ester	11.43	0.99	6.1	8.9	81.2	9.0
Trans-cinnamic acid	14.04	0.99	n.d	106.9	n.d	n.d
Naringenin	15.09	0.99	n.d	n.d	27.8	n.d

Figure 4. Heatmap with Pearson correlation matrix of two different *Scilla* species phytochemical component
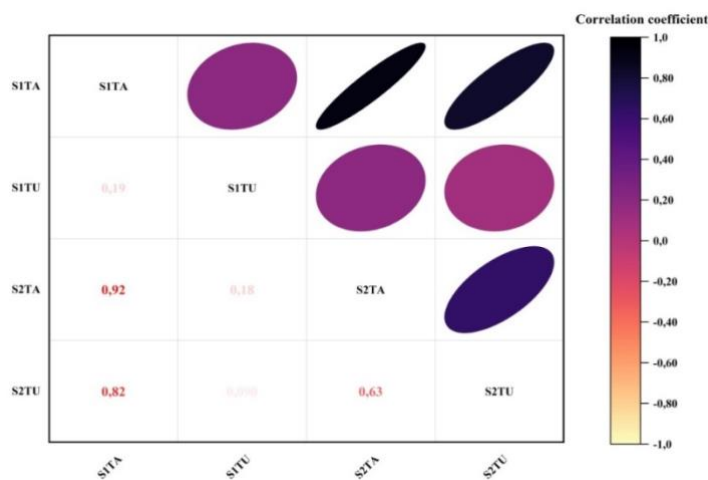
Figure 5. Correlation plot analysis of different parts extracts of two *Scilla* species

In the present study, the TPC and TFC as well as the antioxidant features of the extracts acquired from the plant were investigated and negotiated. S1TU (11.72±0.00 μg PE*s*/mg extract), S1TA (7.03±0.00 μg PE*s*/mg extract)=S2TA(7.03±2.21μg PE*s*/mg extract), S2TU (5.99±0.90 μg PE*s*/mg extract) demonstrated the highest total phenolic content, while S2TU (31. 53±0.21 μg QE*s*/mg extract), S1TU (22.04±0.22 μg *QEs*/mg extract), S2TA (6.41±0.20 μg QE*s*/mg extract), S1TA (5.41±0.35 μg QE*s*/mg extract). Interestingly, the extracts were not active in DPPH activity in the antioxidant activity method. On the other hand, S1TU (IC$_{50}$: 425.66±4.13 μg/mL) proved to be the most active extract in the ABTS method, while S2TU (IC$_{50}$: 185.88±0.30 μg/mL) showed the highest activity in the CUPRAC method (Table 3). Phenolic compounds that contribute to antioxidant capacity

are among the most important compounds found in plants [44]. Flavonoids have many antioxidant properties, such as scavenging radicals and activating enzyme systems [45]. It can be said that the reason why very high antioxidant activity results were not obtained in the work is due to the relatively low amount of phenols and flavonoids. However, the S2TU extract with the highest flavonoid content demonstrated the highest CUPRAC activity, which confirms the known theories of this method. Tanış [12] calculated the TPC and TFC in the methanolic extract of *S. bifolia* as 21.56 mg GAE/g and 27.70 mg RE/g. The DPPH radical scavenging feature of the methanol extract of *S. bifolia* was recorded to be 31.91 ± 0.27 mg TE/g. The ABTS radical scavenging feature was found to be 37.99 ± 1.98 mg TE/g. They reported that the plant extract had a stronger scavenging effect on ABTS radicals. In the FRAP and CUPRAC tests, which are reducing power tests, 31.39 mg TE/g and 83.62 mg TE/g were detected, respectively. The copper reducing power of the plant extract is higher than the iron reducing power. Although differences in terms of the solvent used and the type of solvent were considered, the reducing power is similar to this work. It was noteworthy that the extracts showed antioxidant activity proportional to their high reducing power. Yasuda et al. [46] investigated the antioxidant activity of the MeOH (methanolic) extract of *S. scilloides* (Lindl.) Druce corms using $ABTS^{\bullet+}$ and DPPH methods. The authors of the paper stated that, the $ABTS^{\bullet+}$ and $DPPH^{\bullet}$ clearance abilities were determined as EC_{50} of 51.2 µg/mL and 1.039 µg/mL, respectively. In another research, the total phenolic content of *S. siberica* subsp. *armena* was determined as leaf extract (53.59.59211 µg GAE/mg extract), flower extract (43.88158 µg GAE/mg extract), tuber extract (38.05263 µg GAE/mg extract) and BPE (blue pollen extract) (34.77.632 µg GAE/mg extract) [30]. As a result of the $DPPH^{\bullet}$ and $ABTS^{\bullet+}$ trials, they found that the leaf extract demonstrated the best activity ($IC_{50}=949.81$ µg/mL and $IC_{50}=94.07$ µg/mL, respectively) compared to the standards. In their study, extracts from the aerial parts of *Scilla* species were found to be more efficient than extracts from the corm [30]. This result is consistent with presented study.

Table 3. TPC, TFC, and antioxidant activity results of two *Scilla* species

Treatments	TPC	TFC	IC_{50} values (µg/mL)[c]		$A_{0.5}$ values (µg/mL)[d]
Samples	(µg *PEs*/mg extract)[a]	(µg QE*s*/mg extract)[b]	DPPH Free Radical	ABTS Cation Radical	CUPRAC
S1TU	11.72 ± 0.00	22.04 ± 0.22	>1000	425.66 ± 4.13	202.87 ± 0.04
S1TA	7.03 ± 0.00	5.14 ± 0.35	>1000	713.59 ± 5.05	352.46 ± 3.34
S2TU	5.99 ± 0.90	31.53 ± 0.21	>1000	>1000	185.88 ± 0.30
S2TA	7.03 ± 2.21	6.41 ± 0.20	>1000	$519.09 \pm 5.24.$	245.06 ± 0.53
BHA[e]	-	-	3.22 ± 0.08	2.74 ± 0.03	4.14 ± 0.17
α-TOC[e]	-	-	1.41 ± 0.04	8.48 ± 0.43	13.64 ± 0.32
BHT[e]	-	-	16.71 ± 0.80	4.44 ± 0.30	3.93 ± 0.24

[†]Values expressed are means ± standard deviation of three parallel measurements ($p<0.05$)

[a] *PEs*. pyrocatechol equivalents (y = 0.032x + 0.0445 $R^2 = 0.9947$)

[b] QE*s*. quercetin equivalents (y = 0.0288x + 0.0352 $R^2 = 0.9951$)

[c] Values were given as IC_{50} for DPPH free and ABTS cation radical scavenging activities

[d] Values were given as $A_{0.5}$ for CUPRAC activity

[e] Standart compounds

The anticholinesterase and antityrosinase abilities of the extracts are shown here (Table 4). The most active extracts in terms of AChE inhibition are S1TU (23.90 ± 0.46 % inhibition) and S2TU (23.90 ± 0.75% inhibition) at 200 µg/mL concentration. For BChE inhibition, S1TU (23.04 ± 0.01 % inhibition) and S2TU (21.49 ± 0.87 % inhibition) were identified at 200 µg/mL concentration. In the

tyrosinase inhibition assay, all extracts showed activity above 50%, with the most successful extracts identified as S2TA (57.30±1.68 % inhibition) and S1TA (54.17±1.07 % inhibition) at 200 μg/mL concentration. As a result, the aerial parts were found to be more successful in anticholinesterase activity, while the tubers were more successful in antityrosinase activity. As mentioned above, the main compound of the extracts was reported as VA. In support of the enzyme results, previous studies have reported that vanillic acid is also used in wound healing by suppressing the expression of MITF (microphthalmus-associated transcription factor) and melanogenic enzyme sinB16F10 in cells and reducing melanin levels and tyrosinase activity with or without MSH (melanocyte-stimulating hormone) stimulation [38,39]. In another study, it was found to have a neuroprotective effect [37]. Aktepe et al. [13] showed that all extracts of *S. mesopotamica* were efficient in inhibiting AChE. The authors of the paper documented that the main phenols defined in the extracts of *S. mesopotamica* act as AChE inhibitors. Not many studies were found in the literature review, with the exception of Aktepe et al. [13] on the enzyme inhibition of plants belonging to the genus *Scilla* on the acetylcholinesterase activity of *S. mesopotamica* and Aydın et al. [30] on the antidiabetic activity of *S. siberica* subsp. *armena*. In this case, the data were presented in the study. The authors of the paper have been reviewed and presented for the first time and have helped to enhance the value and originality of this study.

Table 4. Enzyme inhibition activities results of two *Scilla* species

Treatments	Inhibition % (μg/mL)		
Samples	AChE	BChE	Tyrosinase
S1TU	23.90±0.46	23.04±0.01	50.83±0.31
S1TA	12.30±0.76	8.64±0.02	54.17±1.07
S2TU	23.90±0.75	21.49±0.87	51.47±1.08
S2TA	18.77±0.76	4.56±0.01	57.30±1.68
Galanthamin[a]	91.01 ±0.22	80.46±0.18	-
Kojic acid[b]	-	-	95.05±0.37

[†]Values are means of three parallel measurment ± standard deviation (*n*= 3)
[a]Standard compound for AChE and BChE
[b]Standard compound for tyrosinase

At this point in the study, the data obtained in the biological activity experiments were analyzed chemometrically and subjected to correlation tests, and an attempt was made to uncover the correlations of the results by testing their accuracy. The diagrams of PCA and HCA are depicted in Figure 6 and Figure 7, respectively. Figure 8 shows a heat map of the triangle with the Pearson correlation matrix. As can be seen in Figure 6, PC1 explains 52.90% of the data and PC2 explains 30.81%. To elucidate the PC2 components, ABTS, CUPRAC, and TFC activities contribute in the negative squares and comprise the S1TU and S1TA extracts of the plant. DPPH remained in the center as no extract showed activity. It also contributed to the elucidation of PC1 components in the positive quadrature comprising the S2TU and S2TA extracts of the plant and with TPC, AChE, BChE, and anti-tyrosinase activities. However, as can be seen in Figure 7, the dendrogram is divided into two branches with two separate groups, one containing S2TU and the other S1TA and S2TA branching from the same node to which S2TA is connected. A correlation analysis was performed to obtain further knowledge on the relationship between chemical combination and biological activities. Figure 8 shows the triangle heat map with Pearson correlation matrix diagram of the phytochemical compositions and biological activities contained in the extracts to illustrate their relationship. The closer the values are to +1, the higher the correlation is, but the lower this value is, the lower the

correlation relationship is, which is illustrated by the coloring of the heat map (the more the color goes towards black, the stronger the correlation, while the more the color goes towards yellow, the lower the correlation). TPC showed a strong positive correlation with transcinnamic acid, vanillin and shikimic acid. TFC showed a high correlation with naringenin, scutellarin and *p*-coumaric acid. The antioxidant ABTS activity showed a strong positive correlation with the CUPRAC method. However, other phytochemicals showed weak or negative correlations at different levels. Öztürk et al. [47] found in the multivariate analysis of *Alcea fasciculiflora* Zohary species that the secondary metabolites that showed high positive correlation with the phytochemical content of the species and the antioxidant activity methods (ABTS, DPPH, MCA, PPBD), *p*-coumaroylhexaric acid isomer, luteolin, apigenin, *p*-coumaroylhexaric acid, *p*-coumaroylhexaric acid isomer, *p*-coumaroylhexaric acid isomer, feruloylhexaric acid, feruloylhexaric acid isomer, feruloylhexaric acid isomer, feruloylhexaric acid isomer. Intriguingly, AChE activity showed the strongest positive correlation with protocatechuic acid ethyl ester ($n=1$), while hydroxybenzaldehyde ($n=0.98$), caffeic acid ($n=0.99$), syringic acid ($n=0.89$), vanillic acid ($n=0.99$), protocatechuic acid ($n=0.99$) and anti-tyrosinase activity ($n=0.8$), which belong to biological activities, showed strong positive correlations. BChE activity is protocatechuic acid ethyl ester ($n=0.99$), hydroxybenzaldehyde ($n=0.99$), caffeic acid ($n=0.97$), syringic acid ($n=0.86$), vanillic acid ($n=0.98$), protocatechuic acid ($n=0.98$).) showed strong positive correlations with biological activities and anti-tyrosinase activity ($n=0.76$). The tyrosinase inhibition activity of protocatechuic acid ethyl ester ($n=0.85$), hydroxybenzaldehyde ($n=0.82$), caffeic acid ($n=0.88$), syringic acid ($n=0.98$), vanillic acid ($n=0.88$) and protocatechuic acid ($n=0.76$) showed strong positive correlations. The reason why there are no clear or high correlations in the antioxidant activity results suggests that the amounts, types and combinations of total phenolic and flavonoid substances have little influence as shown and expressed in Table 1. Öztürk et al. [47] showed that AChE activity was determined by the secondary metabolites of *A. fascuculifolia* species such as luteolin, tiliroside, kaempferol-O-p-coumaroyl-O hexoside, apigenin, kaempferol, N-feruloyltyramine. Authors of the paper documented that it was significantly positive with presented study. In this section, which contains the most striking part of the study, it should be emphasized and underlined that the secondary metabolites responsible for enzyme inhibition are protocatechuic acid ethyl ester, hydroxybenzaldehyde, caffeic acid, syringic acid, vanillic acid and protocatechuic acid.
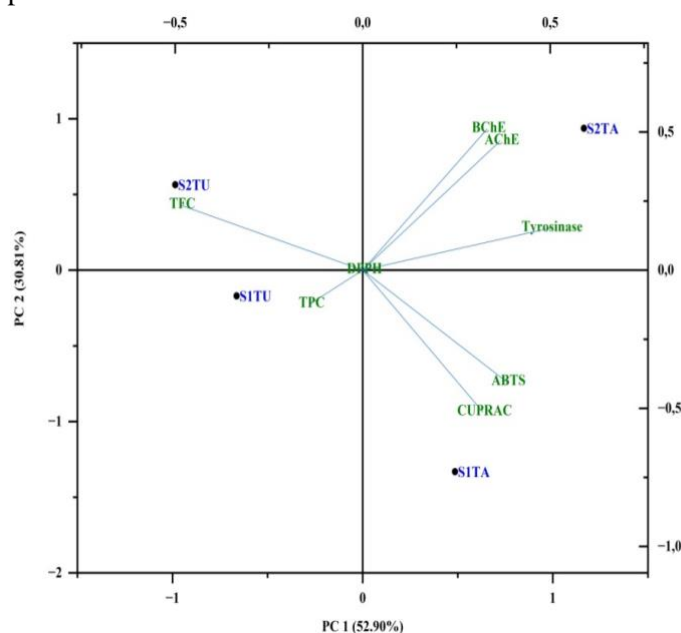
Figure 6. Principal component analysis of biological activity profiles of two *Scilla* species extracts in Table 3, and Table 4
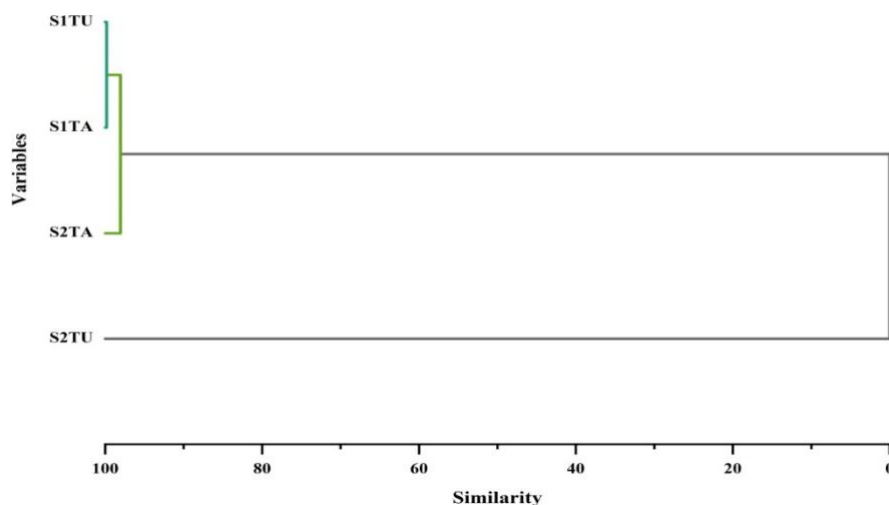
Figure 7. Hierarchial component analysis dendrogram of two *Scilla* species extracts displayed in Table 3, and Table 4
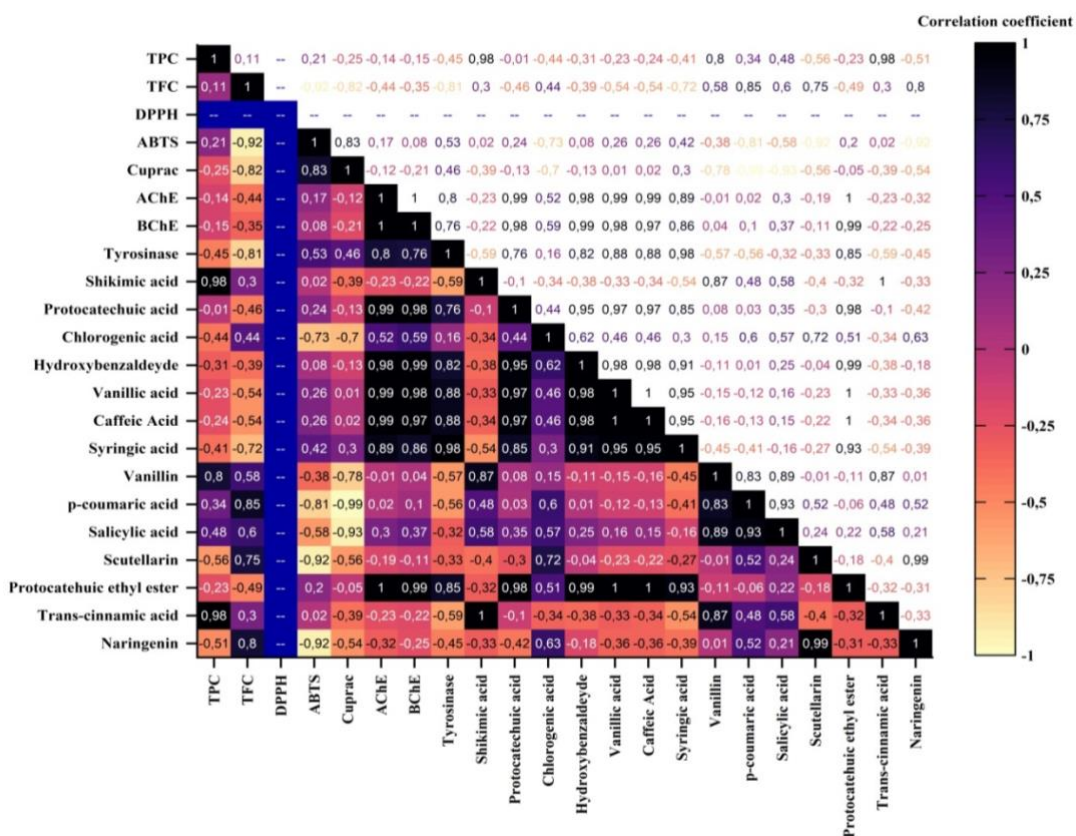
Figure 8. Triangle heat map with Pearson correlation matrix with secondary metabolites and biological activities displayed in Table 2, Table 3, and Table 4

4. Conclusion

In this work, the ethanol extracts of *S. hyacinthoides* and *S. ingridiae* species were found to contain important phytochemical compounds (the most important compound is vanillic acid), and although the total amount of phenols and flavonoids was low, they showed antioxidant activity in different amounts, and the ability to inhibit enzymes was quite successful. Remarkably, in agreement with the results of chemometric data and correlation analysis, it is underlined and emphasized that the secondary metabolites responsible for enzyme inhibition could be protocatechuic acid ethyl ester, hydroxybenzaldehyde, caffeic acid, syringic acid, vanillic acid and protocatechuic acid. These valuable and very important results of the study are supported by many researchers. It is expected to broaden its horizons and vision. The cosmetics, pharmaceutical and medical industries in particular will benefit from the results, as they are at the forefront of the sectors in which they are used. This makes the research results promising candidates for new therapeutic applications in the biomedical field.

Ethical statement

The author declares that this document does not require an ethics committee approval or any special permission. This study does not cause any harm to the environment.

Conflict of Interest

No conflict of interest or common interest has been declared by the author.

Authors' Contributions

A.K: Conceptualization, Methodology, Formal analysis, Writing - Original draft preparation
A.K.: Conceptualization, Methodology, Resources, Investigation
A.K: Methodology, Formal analysis, Writing
A.K: Conceptualization, Methodology, Formal analysis, Writing - Original draft preparation
Author read and approved the final manuscript.

References

[1] Ernst, E., "Harmless herbs? A review of the recent literature", *The American Journal of Medicine*, 104(2), 170-178,1998.

[2] Lichterman, B.L., "Aspirin: the story of a wonder drug", *British Medical Journal*, 329,1408, 2004.

[3] Baytop, T., "*Türkiye'de Bitkiler ile Tedavi-Geçmişte ve Bugün*",second ed. Nobel Tip Kitabevleri, Istanbul, Türkiye, 1999.

[4] Meskin, M.S., "*Phytochemicals in nutrition and health*". CRC Press, Boca Raton, FL, pp. 123, 2002.

[5]   Springbob, K., Kutchan, T., "*Introduction to the different classes of natural products*", In: Lanzotti V (ed) Plant-derived natural products: synthesis, function, and application", Springer, New York, pp. 3, 2009.

[6]   Ülger, T.G., Ayhan, N.Y., "Bitki sekonder metabolitlerinin sağlık üzerine fonksiyonel etkileri", *Acıbadem Üniversitesi Sağlık Bilimleri Dergisi*, 3, 384-390, 2020.

[7]   Mordak, E.V., "*Scilla* L." In: Davis PH (ed.), Flora of Turkey and the East Aegean Islands, Edinburgh University Press, Edinburgh, 8, pp.214-224,1984.

[8]   Speta, F., "Zwei neue Scilla-Arten (Hyacinthaceae) aus der S-Türkei (Two new *Scilla* species from South Turkey)", *Willdenowia*, 21, 157-166,1991.

[9]   Özhatay, N., "*Scilla* L." In: Güner, A, Özhatay N, Ekim T, Başer, KHC, Flora of Turkey and the East Aegean Islands", Edinburgh University Press, Edinburgh, II,pp. 233, 2000.

[10] Iizuka, M., Warashina, T., Noro, T., "Bufadienolides and a new lignan from the bulbs of *Urginea maritime*", *Chemical and Pharmaceutical Bulletin*, 49, 282-286, 2001.

[11] Đorđević, M.R., Zlatković, D.B., and Radulović, N.S., "*Scilla bifolia* Wax as a Source of Diverse Long-Chain Resorcinols and Alkane-1,3-diols", *Chemistry & Biodiversity*, 18,e2000811, 2021.

[12] Tanış K., "*Scilla bifolia*'nın metanolik özütünün antioksidan kapasitesi", Yüksek Lisans Tezi, Selçuk Üniversitesi, Fen Bilimleri Enstitüsü,Konya, 2023.

[13] Aktepe, N., Keskin, C., Baran, A., Atalar, M. N., Baran, M. F., Akmeşe, Ş., "Biochemical components, enzyme inhibitory, antioxidant and antimicrobial activities in endemic plant *Scilla mesopotamica* speta", *Journal of Food Processing and Preservation*,00(e15980),1-13, 2021.

[14] Coşkun, Z.M., "*Scilla autumnalis* L.'nin üreme biyolojisi",Yüksek Lisans Tezi, Marmara Üniversitesi,Fen Bilimleri Enstitüsü, İstanbul, 2007.

[15] Demirtaş, İ., Özen, T., Marah, S., Mutlu, D., Arslan, Ş., Gül, F., "Functional food components and activities of *Pinus nigra* and *Pinus sylvestris* barks as food supplements", *International Journal of Chemistry and Technology*, 7(2), 229-238, 2023.

[16] Slinkard, K., Singleton, V.L., "Total phenol analyses: automation and comparison with manual methods", *American Journal of Enology and Viticulture*, 28, 49-55, 1977.

[17] Moreno, M.I.N., Isla, M.I., Sampietro, A.R., Vattuone, M.A., "Comparison of the free radical-scavenging activity of propolis from several regions of Argentina", *Journal of Ethnopharmacology*, 71, 109-114, 2000.

[18] Ersoy, E., Eroğlu Özkan, E., Boğa, M., and Mat, A., "Evaluation of *in vitro* biological activities of three *Hypericum* species *H. calycinum H. confertum* and *H. perforatum* from Turkey," *South African Journal of Botany*, 130, 141-147, 2020.

[19] Blois, M.S., "Antioxidant determinations by the use of a stable free radical", *Nature*, 181, 1199-1200, 1958.

[20] Re, R., Pellegrini, N., Proteggente, A., Pannala, A., Yang, M., Rice-Evans, C., "Antioxidant activity applying an improved ABTS radical cation decolorization assay", *Free Radical Biology and Medicine*, 26, 1231-1237, 1999.

[21] Ersoy, E., Özkan, E. E., Boğa, M., Yilmaz, M. A., Mat, A., "Anti-aging potential and anti-tyrosinase activity of three *Hypericum* species with focus on phytochemical composition by LC–MS/MS", *Industrial Crops and Products*, 141, 111735, 2019.

[22] Apak, R., Güçlü, K., Özyürek, M., Karademir, S.E., "Novel total antioxidant capacity index for dietary polyphenols and vitamins C and E, using their cupric ion reducing capability in the presence of neocuproine: CUPRAC method", *Journal of Agricultural and Food Chemistry*, 52, 7970-7981, 2004.

[23] Ellman, G.L., Courtney, K.D., Andres, V., Featherstone, R.M., "A new and rapid colorimetric determination of acetylcholinesterase activity", *Biochemical Pharmacology*, 7, 88-95, 1961.

[24] Hearing, V.J., Jiménez, M., "Mammalian tyrosinase-the critical regulatory control point in melanocyte pigmentation", *International Journal of Biochemistry*, 19, 1141-1147, 1987.

[25] Şenol, O., "Erzurum Bölgesinde Yetişen *Betula pendula* Yapraklarının Antioksidan Kapasitelerinin Belirlenmesi ve Kemometrik Karakterizasyonu", *Bartın Orman Fakultesi Dergisi*, 21 (1), 147-154, 2019.

[26] Chaachouay, N.; Zidane, L., "Plant-Derived Natural Products: A Source for Drug Discovery and Development". *Drugs Drug Candidates*, 3, 184-207, 2024.

[27] Stalikas, C.D., "Extraction, separation, and detection methods for phenolic acids and flavonoids", *Journal of Separation Science*, 30(18), 3268-3295, 2007.

[28] Prasad, K.N., Kong, K.W., Ramanan, R.N., Azlan, A., Ismail, A., "Determination and optimization of flavonoid and extract yield from brown mango using response surface methodology", *Separation Science and Technology*, 47(1), 73-80, 2012.

[29] Yaman, C., Ulukuş, D., Tugay, O., "*Haplophyllum suaveolens* Varyetelerinin Antioksidan Aktivitesi ve Sekonder Metabolitleri Üzerine Farklı Çözücülerin Etkisi", *Türkiye Tarımsal Araştırmalar Dergisi*, 6(3), 277-284, 2019.

[30] Aydın, B., Yuca, H., Karakaya, S., Ekşi Bona, G., Göğer, G., Tekman, E., Acar Şahin, A., Sytar, O., Civas, A., Canlı, D., Pınar, N.M., Güvenalp, Z., "The anatomical, morphological features, and biological activity of *Scilla siberica* subsp. *armena* (Grossh.) Mordak (Asparagaceae)", *Protoplasma,* 260(2),371-389, 2023.

[31] Mulholland, D.A., Crouch, N.R., Koorbanally, C., Moodley, N., Pohl, T., "Infraspecific chemical variation in *Scilla zebrina* (Hyacinthaceae)", *Biochemical Systematics and Ecology*, 34 (251e255), 1-5, 2006.

[32] Higashi, T., Ogawa, S., "Chemical derivatization for enhancing sensitivity during LC/ESI-MS/MS quantification of steroids in biological samples: a review", *The Journal of Steroid Biochemistry and Molecular Biology*, 162, 57-69, 2016.

[33] Walton, N.J., Mayer, M.J., Narbad, A., "Vanillin", *Phytochemistry*, 63, 505-515, 2003.

[34] Demir, T., Akpınar, Ö., "Biological Activities of Phytochemicals in Plants", *Turkish Journal of Agriculture - Food Science and Technology*, 8(8), 1734-1746, 2020.

[35] Lv, P.C., HQ, Li., Xue, J.Y., Shi, L., Zhu, H.L., "Synthesis and biological evaluation of novel luteolin derivatives as antibacterial agents", *European Journal of Medicinal Chemistry*, 44, 908-914, 2009.

[36] Ullah, R., Ikram, M. , Park, T.J., Ahmad ,R., Saeed, K., Alam, S.I., Ur Rehman, I., Khan,A., Khan,I. , Jo, M.G., Ok, M.K., "Vanillic Acid, a Bioactive Phenolic Compound, Counteracts LPS-Induced Neurotoxicity by Regulating c-Jun N-Terminal Kinase in Mouse Brain", *International Journal of Molecular Sciences*, 22(1),361, 2020.

[37] Matejczyk, M., Ofman, P., Juszczuk-Kubiak, E., Swis´ łocka, R., Shing, W. L., Kesari, K. K., Prakash, B., Lewandowski, W., "Biological effects of vanillic acid, iso-vanillic acid, and orto-vanillic acid as environmental pollutants", *Ecotoxicology and Environmental Safety*, 277 (116383),1-11, 2024.

[38] Park, J., Cho, S.Y., Kang, J., Park, W.Y., Lee, S., Jung, Y., Kang, M.W., Kwak, H.J., Um, J.Y., "Vanillic Acid Improves Comorbidity of Cancer and Obesity through STAT3 Regulation in High-Fat-Diet-Induced Obese and B16BL6 Melanoma-Injected Mice", *Biomolecules*, 10, 1098, 2020.

[39] Alamri, E.S., El Rabey, H.A., Alzahrani, O.R., Almutairi, F.M., Attia, E.S., Bayomy, H.M., Albalwi, R.A., Rezk, S.M., "Enhancement of the Protective Activity of Vanillic Acid against Tetrachloro-Carbon (CCl$_4$) Hepatotoxicity in Male Rats by the Synthesis of Silver Nanoparticles (AgNP*s*)", *Molecules*, 27, 8308, 2022.

[40] Calixto-Campos, C., Carvalho, T.T., Hohmann, M.S.N., Pinho-Ribeiro, F.A., Fattori, V., Manchope, M.F., Zarpelon, A., Baracat, M.M., Georgetti, S.R., Casagrande, R., Verri Jr, W.A., "Vanillic Acid Inhibits Inflammatory Pain by Inhibiting Neutrophil Recruitment, Oxidative Stress, Cytokine Production, and NFκB Activation in Mice", *Journal of Natural Products*, 78, 1799-1808, 2015.

[41] Yao, X., Jiao, S., Qin, M., Hu, W., Yi, B., Liu, D., "Vanillic Acid Alleviates Acute Myocardial Hypoxia/Reoxygenation Injury by Inhibiting Oxidative Stress", *Oxidative Medicine and Cellular Longevity*, 2020 (8348035), 2020.

[42] Bai, J.R., Zhong, K., Wu, Y.P., Elena, G., Gao, H., "Antibiofilm activity of shikimic acid against *Staphylococcus aureus*", *Food Control*, 95, 327-333, 2019.

[43] Chen, F. L., Hou, K. X., Li, S. Y., Zu, Y. G., & Yang, L., "Extraction and chromatographic determination of shikimic acid in Chinese conifer needles with 1-Benzyl-3- methylimidazolium bromide ionic liquid aqueous solutions", *Journal of Analytical Methods in Chemistry*,3, 256473, 2014.

[44] Apak, R., Güçlü, K., Demirata, B., Özyürek, M., Çelik, S. E., Bektaşoğlu, B., Berker, K. I. & Özyurt, D., "Comparative evaluation of various total antioxidant capacity assays applied to phenolic compounds with the CUPRAC assay", *Molecules*, 12(7), 1496-1547, 2007.

[45] Handique, J.G., Baruah, J.B., "Polyphenolic compounds: an overview", *Reactive and Functional Polymers*, 52,163-188, 2002.

[46] Yasuda, S., Nishida, Y., Wada, K., Akiyama, D., Toyohisa, D., Tanaka, T., Igoshi, K., Ono, M., "Anti-inflammatory and antioxidative effects of a methanol extract from bulbs of *Scilla scilloides*", *Bioscience, Biotechnology, and Biochemistry*, 77(1),1569-1571,2013.

[47] Özturk, R.B., Zengin, G., Sinan, K.I., Montesano, D., Zheleva-Dimitrova, D., Gevrenova, R., Uba, A.I., Çakılcıoğlu, U., Kaplan, A., Jugreet, S., Dall'Acqua, S., Mahomoodally, M. F., "Which Extraction Solvents and Methods Are More Effective in Terms of Chemical Composition and Biological Activity of *Alcea fasciculiflora* from Turkey?", *Molecules*, 27, 5011, 2022.

Middle East Journal of Science

Research Article

BIOPHYSICAL INVESTIGATION OF MOLECULAR INTERACTIONS BETWEEN ALLIIN AND ANIONIC DMPG MODEL MEMBRANE: AN FTIR STUDY

Nazli EZER OZER [1]   *Burcu KARAGOZ TOPTAS*[2]   *Ipek SAHIN*[2*]

[1]Istanbul Medipol University, International School of Medicine, Department of Biophysics, Istanbul, Turkiye
[2]Ege University, Faculty of Science, Department of Physics, Izmir, Turkiye
*Corresponding Author: ipek.sahin@ege.edu.tr

Abstract *Garlic, which contains bioactive compound alliin, is a medicinal herb that has been traditionally utilized for its therapeutic properties against a range of illnesses. Our aim is to investigate the interactions between alliin and anionic dimyristoyl phosphatidylglycerol (DMPG) multilamellar vesicles (MLVs) at various temperatures and alliin concentrations (1, 3, 6 and 9 mol%) using Fourier transform infrared (FTIR) spectroscopy. The PerkinElmer Frontier spectrometer was used to collect spectra within the region of 4000-1000 cm^{-1}. The specimens were subjected to scanning within a temperature range of 0 to 40 $°C$ using the Specac temperature control device. The analyses were conducted utilizing the Spectrum v10.3.7 program. By introducing both low and high concentrations of alliin to DMPG MLVs, the wavenumber values of the CH_2 antisymmetric stretching band decreased, while the bandwidth values increased, both in the gel and liquid crystal phases. During the gel phase, the presence of alliin resulted in a downward shift of the C=O stretching bands' wavenumber values. Opposite evidence occurred in the liquid crystal phase. The wavenumber values of the PO_2^- antisymmetric stretching band exhibited a shift towards lower values both in the gel and liquid crystal phases. In the present study, we investigated the biophysical effects of alliin on DMPG model membranes using parameters such as lipid order, dynamics and hydrogen bonding ability. The addition of alliin altered the physical characteristics of the DMPG MLVs by ordering the system, enhancing its dynamics, and promoting hydrogen bond interactions between the phosphate group of DMPG and alliin or water molecules, both in the gel and liquid crystalline phases. Moreover, alliin enhanced the strength of hydrogen bonding in proximity to carbonyl groups in the gel phase.*

Keywords: *Alliin, DMPG, MLV, FTIR, Model membrane*

1. Introduction

The use of model membranes that mimic the complex and dynamic structure of biological membranes to investigate the pharmacological action mechanisms of drugs is frequently seen in the literature [1-3]. Garlic has been used for centuries in all cultures as a therapeutic agent on bacterial infections, cardiovascular diseases, diabetes, and even cancer thanks to its antibacterial, antioxidant, antidiabetic, and anticancer properties [4-8]. Alliin, which we used in our study, is one of the bioactive organosulfur compounds that promote the clinical use of garlic. When garlic is damaged for various reasons, alliin turns into allicin, another bioactive component of garlic [9].

It is possible to investigate the impact of drugs on membrane localization, membrane phase transition, order, and dynamics in the light of the unique data that can be obtained by examining the spectral bands belonging to the functional groups in certain biomolecules using FTIR spectroscopy. In this manner, the structural and functional properties of garlic as well as its clinical effects have been

investigated in the literature by Raman and FTIR spectroscopies [10-12]. However, there are only a few studies examining the interaction of alliin with biological membranes, which are the target systems of drugs, or with model membranes that are structurally and functionally remarkably similar to biological membranes. Allicin has been preferred in both clinical, physiological, and pharmacological studies [13-15]. For example, a reference noted the antioxidant effect of alliin by stabilizing the membrane in isoproterenol-induced myocardial infarction in male mice [16]. In a study examining the antiproliferative effect of alliin, it was reported that alliin inhibited the proliferation of gastric adenocarcinoma cells and caused a slight decrease in mitochondrial membrane potential [17]. Alliin has been reported to significantly reduce nuclear membrane damage in oogenesis cells in X-ray irradiated white mice [18]. Furthermore, one study showed that alliin and other sulphur compounds reduced the fluidity of tumour cell and platelet model membranes prepared with cholesterol and phospholipids, as well as candida cell model membranes prepared with ergosterol and phospholipids [19].

In our previous study [20], where we investigated the physical interactions between alliin and DMPC model membrane as a function of alliin concentration and temperature using FTIR spectroscopy, we revealed the regulatory effect of alliin on many parameters such as lipid order, dynamics, and hydrogen bonding capacity. To check whether these parameters change depending on the head group charge of the model membranes, in this study we examined the changes in the above-mentioned parameters caused by different alliin concentrations in the negatively charged DMPG model membrane, depending on temperature, using FTIR spectroscopy.

2. Materials and Methods

2.1. Chemicals

Alliin and DMPG were acquired from Sigma (St. Louis, MO, USA) and utilized without additional purification.

2.2. Sample preparation

The specimens for the FTIR investigation were prepared following the procedure identified by Severcan et al. [21]. To form liposomes, firstly 5 mg of DMPG solution was dissolved in chloroform and dry lipid films were obtained. It was then treated with nitrogen gas to remove excess chloroform from the solution. The additional solution was dried using a Christ LT-105 spin vacuum apparatus for 2 hours. The thin films were hydrated by adding 25 µl of a 10 mM phosphate buffer solution with a pH of 7.4. The formation of multilamellar liposomes was achieved by subjecting the mixture to vortex for a duration of 30 minutes at a temperature that was 20 °C higher than the main transition temperature [T_m] of DMPG, which is 43 °C. To create liposomes containing alliin, a certain quantity of alliin from the stock solution was first poured into the sample tube. To conduct FTIR measurements, a volume of 20 µl of liposomes was positioned between CaF_2 windows, resulting in a sample thickness of 12 µm.

2.3. FTIR studies and spectral analysis

The spectra were obtained using a PerkinElmer Frontier FTIR spectrophotometer. The fingerprint region is analyzed within the range of 4000-400 cm^{-1} using an FTIR spectrometer. Nonetheless, the utilization of the CaF_2 window restricts the wavenumber range that can be investigated. For this reason, a temperature ranges of 0-40 °C was used to scan the mid-infrared reagion of 4000-1000 cm^{-1}. The temperature was monitored using a Specac digital temperature controller. The samples were subjected to incubation at each temperature for a duration of 5 minutes prior to scanning the spectrum. The interferograms were combined by taking the average of 50 scans, with a resolution of 2 cm^{-1}. The water absorption bands in the range of 3050-2800 and 1700-1500 cm^{-1} strongly overlap with the corresponding

bands from lipid functional groups [1-3,20,21]. To enhance the clarity of the bands, the water bands were eliminated from the spectra using PerkinElmer Spectrum v10.3.7 software. The spectra were normalized in 3000-2800 cm^{-1} regions using the same software to visually represent and compare changes. FTIR experiments were repeated 3 times and the same results were observed.

3. Results

The current research used FTIR spectroscopy to examine the temperature dependence of DMPG MLVs with and without alliin concentrations ranging from 1 to 9 mol%. The examination of FTIR spectra focused on the investigation of CH_2 antisymmetric stretching, C=O stretching, and PO_2^- antisymmetric double stretching bands. The experiments were replicated a total of three and consistent patterns were detected on each occasion.

Normalized average FTIR spectrum of the DMPG liposomes with and without 9 mol% alliin in the gel (15 °C) and liquid crystal (35 °C) phases were shown in Figures 1(a) and (b), respectively. Visual representations of average spectra were used to demonstrate and compare the alterations in frequency, intensity, and bandwidth of particular bands of focus in the lipid with and without alliin.
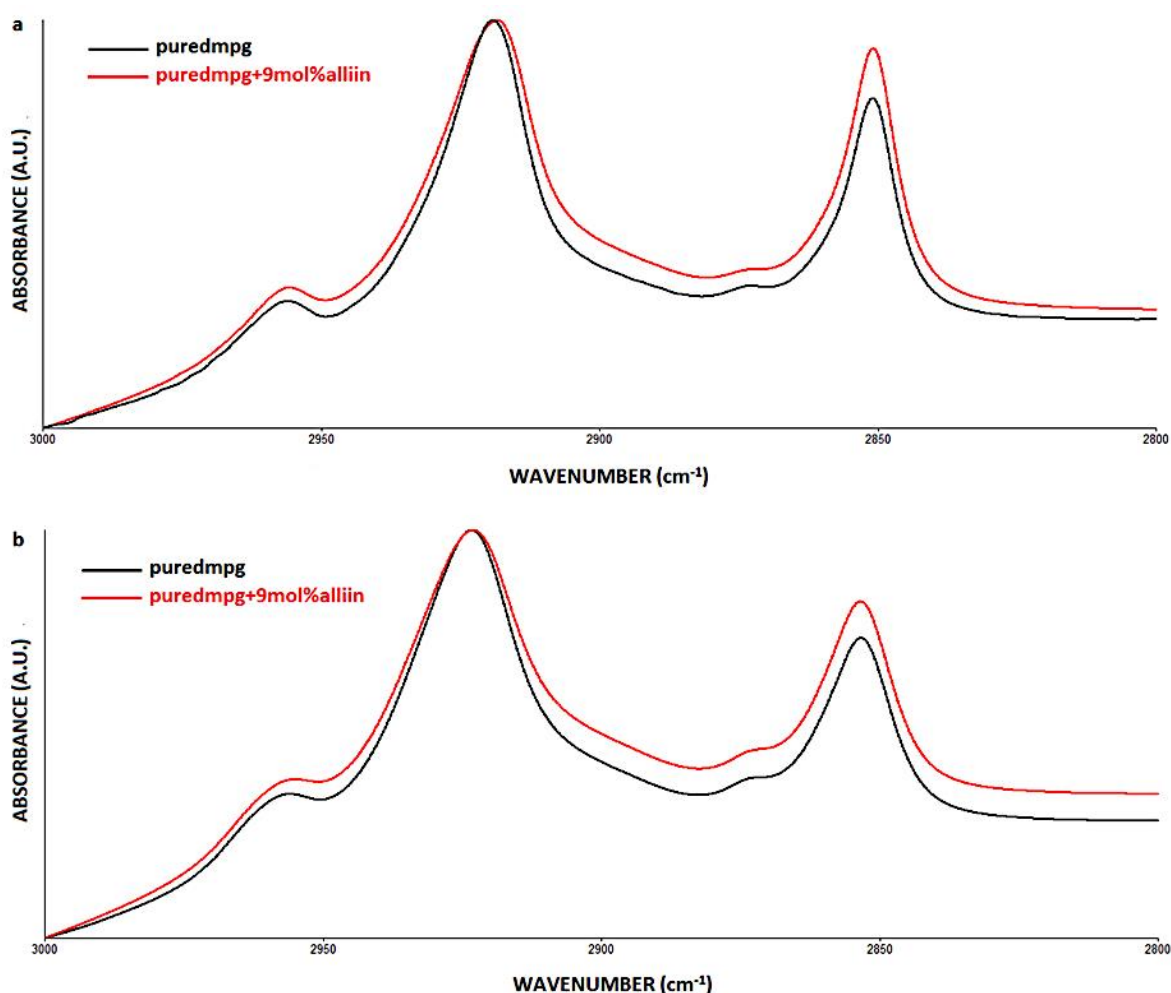
Figure 1. FTIR spectra of DMPG model membranes in the C-H stretching region at **(a)** 15 °C and **(b)** 35 °C with and without 9 mol% alliin.

Figure 2 illustrated the relationship between temperature and the frequency of the CH_2 antisymmetric stretching band of DMPG MLVs including data for both the absence and presence of

various doses of alliin. We conducted a frequency analysis of the CH_2 antisymmetric stretching band to acquire comprehensive insights into the phase transition behaviour and order-disorder condition of the system [2,3]. The main phase transition temperature (T_m) of the pure DMPG model membrane was determined at 23 °C, as in the DMPC model membrane, and the pre-phase transition temperature was determined at 15 °C (Figure 2). The gel phase is the state in which the lipid acyl chains are in a regular and tightly packed structure at temperatures below the main phase transition temperature whereas the liquid crystal phase is the state in which the lipid acyl chains are in a disordered and completely melted structure [1,2]. Our observation revealed that with an increase in alliin concentration, the frequency of the CH_2 antisymmetric stretching band decreased, leading to an enhancement in the trans configuration and order of the system in both the gel and liquid crystal phases.
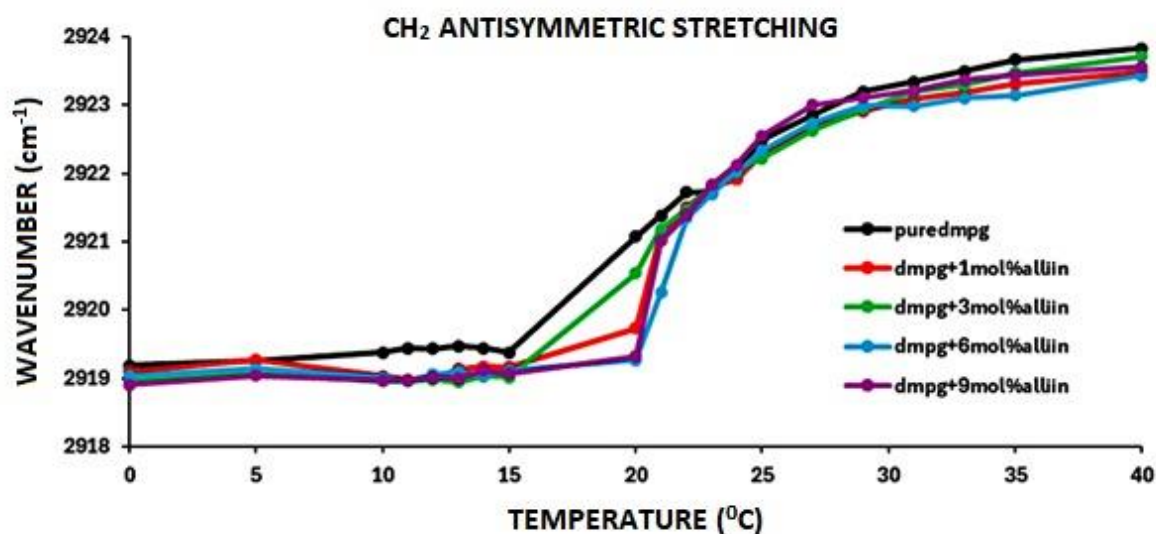
Figure 2. The frequency changes of CH_2 antisymmetric stretching modes of DMPG model membranes as a function of temperature, both in the presence and absence of varying doses of alliin.

Figure 3 displayed the variations in the bandwidth of CH_2 antisymmetric stretching in DMPG model membranes resulting from the introduction of alliin at varying concentrations, depending on the temperature. The bandwidth parameter provides information regarding the fluidity of the membrane, namely the movement of lipid acyl chains. The relationship between bandwidth and fluidity in a system is such that as bandwidth increases, system fluidity also increases. Conversely, as bandwidth values decrease, membrane fluidity decreases [2,3]. Adding alliin concentrations of 3, 6, and 9 mol% to DMPG MLVs demonstrated a rise in membrane fluidity in both the gel and liquid crystal phases. The inclusion of 1 mol% alliin concentration resulted in a notable reduction in membrane fluidity in both the gel and liquid crystal phases, thereby stabilizing the system (Figure 3).
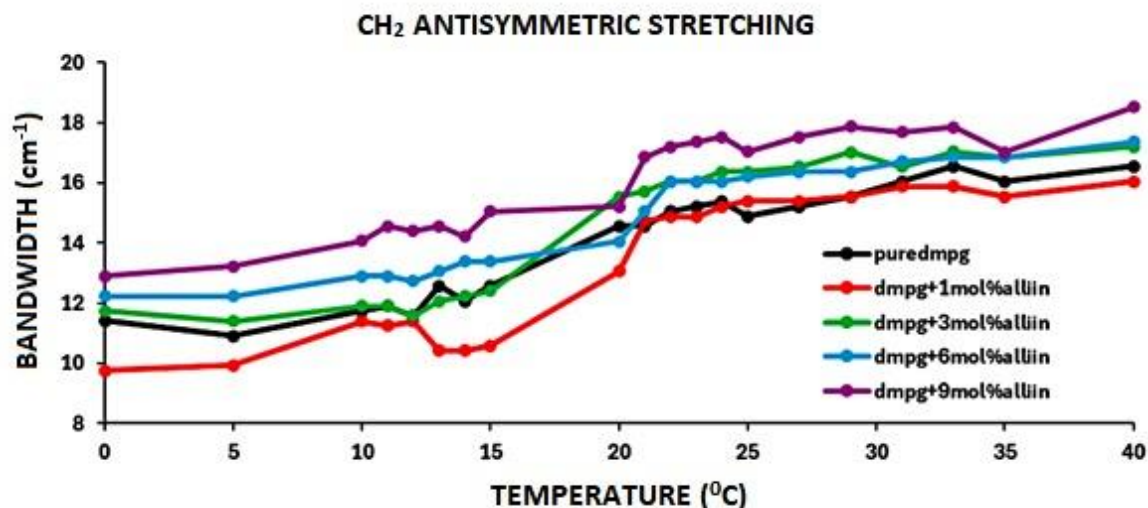
Figure 3. Temperature-dependent changes of the bandwidth of CH_2 antisymmetric stretching modes of DMPG model membranes in the presence and absence of varying concentrations of alliin.

Figure 4 demonstrated the variation in the frequency of the C=O stretching band as a function of temperature. Our study yielded contrasting outcomes about the alteration in the frequency of the C=O stretching band between the gel and liquid crystalline phases. While the presence of alliin in the gel phase resulted in a decrease in frequency, it had the opposite effect in the liquid crystal phase, causing an increase in frequency (Figure 4). This suggested that during the gel phase, alliin formed a robust hydrogen bond with the glycerol backbone near the head group of DMPG phospholipids in the interfacial area. In the liquid crystal phase, it revealed the presence of unbound carbonyl groups at the system [22].
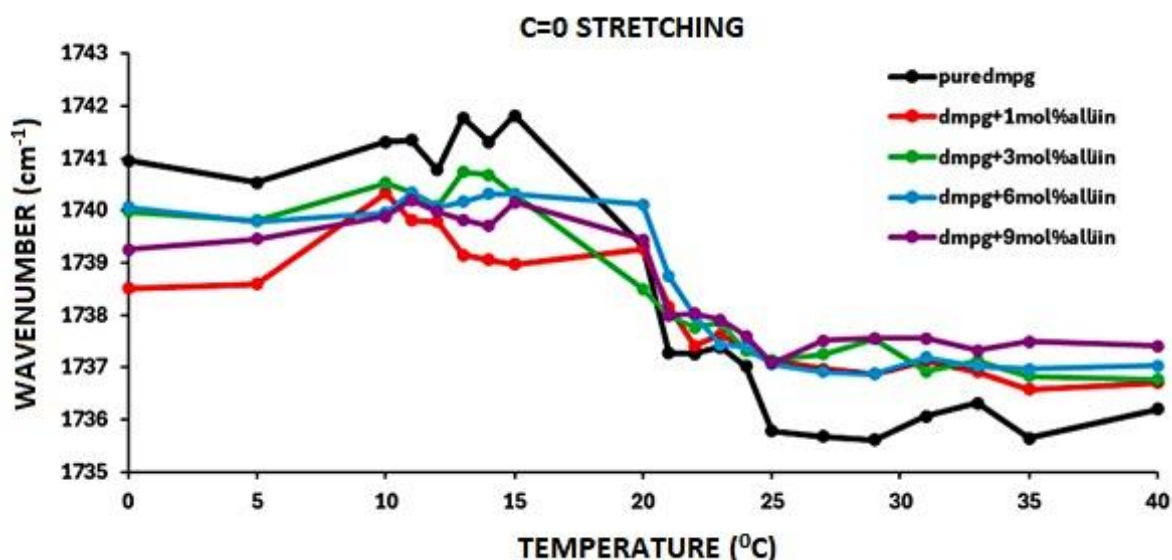
Figure 4. Changes of the frequency of C=O stretching modes of DMPG model membranes as a function of temperature, both in the presence and absence of low and high doses of alliin.

Figure 5 illustrated the change in frequency of the PO_2^- antisymmetric stretching band for DMPG MLVs both with and without varied amounts of alliin as a function of temperature. As depicted

in the diagram (Figure 5), the frequency decreased when alliin was added at both low and high concentrations. The impact was particularly significant in the gel phase, as it leaded to the reinforcement of the hydrogen bonding between the phosphate group of liposomes and the adjacent alliin or water molecules [1].
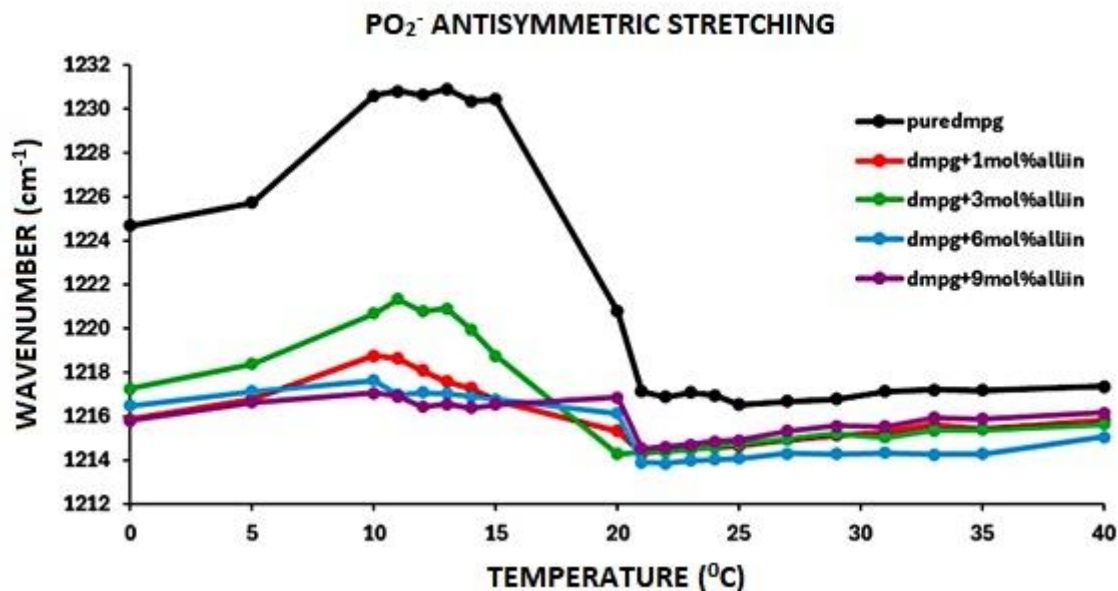
Figure 5. Changes of the frequency of PO_2^- stretching modes of DMPG model membranes as a function of temperature, both in the presence and absence of low and high doses of alliin.

4. Discussion

FTIR spectroscopy is based on the principle of measuring the vibration of chemical bonds by applying electromagnetic radiation at infrared wavelengths. The changes in the vibrations of chemical bonds in the infrared region and the absorption properties provide the formation of spectral peaks [23]. In the literature, the use of infrared spectroscopy to elucidate the therapeutic effect mechanism of drugs is increasing day by day [24]. If it is desired to investigate the changes caused by many bioactive compounds such as vitamins, minerals, hormones, etc. in model membranes, it is sufficient to examine the bands corresponding to different functional groups in FTIR spectra [1-3,20-22]. For example, the shift in the frequency value of the CH_2 antisymmetric stretching mode provides detailed information about the structure of the membrane, and the bandwidth provides detailed information about the mobility of lipid acyl chains [23].

In our study, analysis of CH_2 antisymmetric stretching vibrations showed that alliin reduced the acyl chain flexibility of DMPG liposomes in both gel and liquid crystalline phases, indicating an increase in the ordering of phospholipids. The chain order of membrane lipids has a significant effect on permeability. Increasing the order of lipid bilayers reduces agent diffusion [25]. Xiang and Anderson [26] studied the permeability of monocarboxylic acids in gel and liquid crystal phases of dipalmitoyl phosphatidylcholine (DPPC) model membranes with nuclear magnetic resonance (NMR) spectroscopy depending on lipid order and showed that membrane permeability depends on the cross-sectional area of the agent. In a study measuring water permeability using model membranes with different head groups, chain lengths and unsaturation, Mathai et al. [27] showed that membrane permeability is affected

by area/lipid and membrane thickness. In contrast, Gruhlke and colleagues [28] found that allicin increased membrane permeability, whereas Miron and colleagues [29] observed no effect.

An additional factor that must be scrutinized in order to comprehend the impact of a drug on membrane structure and function is the thickness parameter. Increased lipid order was experimentally associated with greater membrane thickness in a study by Kučerka et al. [30], in which cholesterol-model membrane interactions were examined by neutron diffraction methods. In addition, Balakrishnan and Kenworthy [31] observed that peroxidation, one of the properties that changes the structure and proper functioning of lipids, also leads to a decrease in the thickness of the bilayer and an increase in membrane permeability. According to our results, the antioxidant effects of alliin, which are widely commented in the literature [32-34], can be attributed to its ability to defend against lipid peroxidation, which may lead to membrane thickening and a decrease in permeability.

The fluidity of model membranes can be modified by the lipid composition and consequently alter the functional properties of the membrane [35]. We reported that the administration of alliin at varying doses increased the dynamics of negatively charged DMPG model membranes. This result is consistent with the results of our study conducted in our laboratory in 2017. We found that alliin also increased the mobility of zwitterionic DMPC model membranes [20]. Unexpectedly, the fluidity of the negatively charged DMPG membrane was reduced when 1 mol% alliin was introduced. This phenomenon could be attributed to the hydrophobic interactions occurring between alliin molecules and the acyl chains of DMPG MLVs. Consistent with our findings, a study employing electron paramagnetic resonance spectroscopy discovered that garlic extract caused a rise in the pliancy of red blood cell membranes [36]. A study conducted in 2008 by Tsuchiya et al. [37] demonstrated that sulphur compounds present in garlic caused an increase in fluidity and thickness of DPPC and DPPC: cholesterol MLVs. Pinilla et al. [38] found that the presence of phosphatidylcholine, oleic acid, and garlic extract resulted in an elevation of membrane rigidity under heat exposure.

Another factor that decreases the flexibility of the DMPG model membrane could be linked to the development of new hydrogen bonds or the reinforcement of existing hydrogen bonds between the hydroxyl groups of alliin and the carbonyl groups of DMPG [39]. Examining the C=O and PO_2^- functional groups allowed us to observe the changes that alliin produces in the interface and polar head group region of DMPG MLVs. Based on our findings, we observed that different concentrations of alliin in the gel phase resulted in an increase in the number of H-bonded carbonyls. However, in the liquid crystal phase, the C=O groups remained in their free form. The decrease in wavenumber values of the PO_2^- antisymmetric stretching band, upon the addition of alliin, suggests an increase in H-bond interactions between the phosphate group of DMPG and the surrounding alliin or water molecules [20].

Model membranes consist of lipids with diverse head groups and alkane chains. DMPG, an essential constituent of biological membranes, has a negative charge at the phosphate group. Consequently, the characteristics of the DMPG bilayer may be influenced by the counterion present [40]. One of the intermolecular attractive forces is the ion-dipole interaction between a charged ion and polar molecules, which can be attributed to the molecular interaction between alliin and DMPG. Consistent with our expectations, our research confirms that the charge status of the phospholipid head group determines the action mechanism of alliin with model membranes. Repulsion of negative charges in the head group of DMPG MLVs may have caused the acyl chains to interact less frequently, which explains this situation [3]. In addition, our agent is thought to localize in the DMPG lipid membrane's more polar or near-polar areas [22].

Within the scope of this research, we aimed to determine the biophysical effects of alliin, a bioactive component of garlic, on negatively charged DMPG liposomes using FTIR spectroscopy and to offer an alternative to the therapeutic mechanism of action. We examined the interactions of alliin with DMPG MLVs through structural and functional parameters and compared them with our previous

study. We showed that it may be possible to alter the membrane response and sensitivity of alliin depending on the charge difference in the head group region of the phospholipids. Given the variation in lipid content across different parts in the human body, comprehending medication-lipid interaction can aid in assessing the potential impacts of the medicine on actual biological systems. This work aims to biophysically analyse the molecular alterations induced by medicines in model membranes, with the goal of providing insights about the impact of garlic on biological systems.

Ethical Statement

The authors declare that this study does not require ethics committee approval.

Conflict of Interest

The authors have no conflicts of interest to declare.

Author Contributions

Concept: İ.S., Literature Review: N.E.O., İ.S., Design: N.E.O., İ.S., Data acquisition: N.E.O., B.K.T., Analysis and interpretation: N.E.O., B.K.T., Writing manuscript: N.E.O., Critical revision of manuscript: N.E.O., İ.S.

Financial Disclosure

Authors declared no financial support.

References

[1]   Korkmaz, F., Severcan, F., "Effect of progesterone on DPPC membrane: Evidence for lateral phase separation and inverse action in lipid dynamics", *Archives of Biochemistry and Biophysics*, 440(2), 141-147, 2005. Doi: 10.1016/j.abb.2005.06.013.

[2]   Aleskndrany, A., Sahin, I., "The effects of Levothyroxine on the structure and dynamics of DPPC liposome: FTIR and DSC studies", *Biochimica et Biophysica Acta (BBA) – Biomembranes*, 1862(6), 183245, 2020. Doi: 10.1016/j.bbamem.2020.183245.

[3]   Bilge, D., Kazanci, N., Severcan, F., "Acyl chain length and charge effect on Tamoxifen–lipid model membrane interactions", *Journal of Molecular Structure*, 1040, 75-82, 2013. Doi: 10.1016/j.molstruc.2013.02.031.

[4]   Banerjee, S.K., Maulik, S.K., "Effect of garlic on cardiovascular disorders: a review", *Nutrition Journal*, 1(4), 1-14, 2002. Doi: 10.1186/1475-2891-1-4.

[5]   Magryś, A., Olender, A., Tchórzewska, D., "Antibacterial properties of *Allium sativum* L. against the most emerging multidrug-resistant bacteria and its synergy with antibiotics", *Archives of Microbiology*, 203(5), 2257-2268, 2021. Doi: 10.1007/s00203-021-02248-z.

[6]   Ashraf, R., Khan, R.A., Ashraf, I., "Garlic [Allium sativum] supplementation with standard antidiabetic agent provides better diabetic control in type 2 diabetes patients", *Pakistan Journal of Pharmaceutical Sciences*, 24(4), 565-70, 2011. PMID: 21959822.

[7]   Ried, K., Toben, C., Fakler, P., "Effect of garlic on serum lipids: an updated meta-analysis", *Nutrition Reviews*, 71(5), 282-299, 2013. Doi: 10.1111/nure.12012.

[8]   Tsubura, A., Lai, Y.-C., Kuwata, M., Uehara, N., Yoshizawa, K., "Anticancer Effects of Garlic and garlic-derived Compounds for Breast Cancer Control", *Anti-Cancer Agents in Medicinal Chemistry*, 11(3), 249-253, 2011. Doi: 10.2174/187152011795347441.

[9]   Omar, S.H., Al-Wabel, N.A., "Organosulfur compounds and possible mechanism of garlic in cancer", *Saudi Pharmaceutical Journal*, 18(1), 51-58, 2010. Doi: 10.1016/j.jsps.2009.12.007.

[10] Lu, X., Rasco, B.A., Jabal, J.M., Aston, D.E., Lin, M., Konkel, M.E., "Investigating Antibacterial Effects of Garlic [*Allium sativum*] Concentrate and Garlic-Derived Organosulfur Compounds on *Campylobacter jejuni* by Using Fourier Transform Infrared Spectroscopy, Raman Spectroscopy, and Electron Microscopy", *Applied and Environmental Microbiology*, 77(15), 5257-5269, 2011. Doi: 10.1128/AEM.02845-10.

[11] Akilan, S., Prabakar, K., "Spectral studies and antibacterial activity of Garlic *[Allium sativum L.]*", *Journal of Emerging Technologies and Innovative Research (JETIR)*, 5(7), 452-7, 2018. ISSN:2349-5162.

[12] Nagarajan, D., Ramesh Kumar, T., "Fourier transform infrared spectroscopy analysis of garlic [Allium]", *International Journal of Zoology Studies (IJZS)*, 2(6), 11-14, 2017. ISSN: 2455-7269.

[13] Huang, L., Jia, S., Wu, R., Chen, Y., Ding, S., Dai, C., He, R., "The structure, antioxidant and antibacterial properties of thiol-modified soy protein isolate induced by allicin", *Food Chemistry*, 396, 133713, 2022. Doi: 10.1016/j.foodchem.2022.133713.

[14] Tyagi, G., Pradhan, S., Srivastava, T., Mehrotra, R., "Nucleic acid binding properties of allicin: Spectroscopic analysis and estimation of anti-tumor potential", *Biochimica et Biophysica Acta (BBA) - General Subjects*, 1840(1), 350-356, 2014. Doi: 10.1016/j.bbagen.2013.09.007.

[15] Awan, U.A., Ali, S., Shahnawaz, A.M., Shafique, I., Zafar, A., Khan, M.A.R., Ghous, T., Saleem, A., Andleeb, S., "Biological activities of Allium sativum and Zingiber officinale extracts on clinically important bacterial pathogens, their phytochemical and FT-IR spectroscopic analysis", *Pakistan Journal of Pharmaceutical Sciences (PJPS)*, 30[3], 729-745, 2017. PMID: 28653916.

[16] Sangeetha, T., Darlin Quine, S., "Preventive effect of S-allyl cysteine sulfoxide [alliin] on lysosomal hydrolases and membrane-bound ATPases in isoproterenol-induced myocardial infarction in Wistar rats", *Journal of Biochemical and Molecular Toxicology*, 21(3), 118-124, 2007. Doi: 10.1002/jbt.20166.

[17] Mansingh, D.P., Dalpati, N., Sali, V.K., Vasanthi, A.H.R., "Alliin the Precursor of Allicin in Garlic Extract Mitigates Proliferation of Gastric Adenocarcinoma Cells by Modulating Apoptosis", *Pharmacognosy Magazine*, 14(55), 84-91, 2018. Doi: 10.4103/pm.pm_342_17.

[18] Ji, T.-J., "Radioprotection of Alliin in Oogenesis Cells of a White Rat", *Journal of Radiological Science and Technology*, 41(5), 471-478, 2018. Doi: 10.17946/10.17946/JRST.2018.41.5.471.

[19] Tsuchiya, H., Nagayama, M., "Garlic allyl derivatives interact with membrane lipids to modify the membrane fluidity", *Journal of Biomedical Science*, 15(5), 653-660, 2008. Doi: 10.1007/s11373-008-9257-8.

[20] Ezer, N., Sahin I, Kazanci, N., "Alliin interacts with DMPC model membranes to modify the membrane dynamics: FTIR and DSC Studies", *Vibrational Spectroscopy*, 89, 1-8, 2017. Doi: 10.1016/j.vibspec.2016.12.006.

[21] Severcan, F., Sahin, I., Kazanci, N., "Melatonin strongly interacts with zwitterionic model membranes—evidence from Fourier transform infrared spectroscopy and differential scanning calorimetry", *Biochimica et Biophysica Acta [BBA] – Biomembranes*, 1668(2), 215-222, 2005. Doi: 10.1016/j.bbamem.2004.12.009.

[22] Turker, S., Wassall, S., Stillwell, W., Severcan, F., "Convulsant agent pentylenetetrazol does not alter the structural and dynamical properties of dipalmitoylphosphatidylcholine model membranes", *Journal of Pharmaceutical and Biomedical Analysis*, 54(2), 379-386, 2011. Doi: 10.1016/j.jpba.2010.09.002.

[23] Casal, H.L., Mantsch, H.H., "Polymorphic Phase Behaviour of Phospholipid Membranes Studied by Infrared Spectroscopy", *Biochimica et Biophysica Acta (BBA)*, 779, 381-401, 1984. Doi: 10.1016/0304-4157[84]90017-0.

[24] Knobloch, J., Suhendro, D.K., Zieleniecki, J.L., Shapter, J.G., Köper, I., "Membrane-drug interactions studied using model membrane systems", *Saudi Journal of Biological Sciences*, 22(6), 714-718, 2015. Doi: 10.1016/j.sjbs.2015.03.007.

[25] Shinoda, W., "Permeability across lipid membranes", *Biochimica et Biophysica Acta [BBA] – Biomembranes*, 1858(10), 2254-2265, 2016. Doi: 10.1016/j.bbamem.2016.03.032.

[26] Xiang, T-X., Anderson, B.D., "Influence of Chain Ordering on the Selectivity of Dipalmitoylphosphatidylcholine Bilayer Membranes for Permeant Size and Shape", *Biophysical Journal*, 75(6), 2658-2671, 1998. Doi: 10.1016/S0006-3495[98]77711-2.

[27] Mathai, J.C., Tristram-Nagle, S., Nagle, J.F., Zeidel, M.L., "Structural Determinants of Water Permeability through the Lipid Membrane", *Journal of General Physiology (JGP)*, 131(1), 69-76, 2008. Doi: 10.1085/jgp.200709848.

[28] Gruhlke, M.C.H., Hemmis, B., Noll, U., Wagner, R., Lühring, H., Slusarenko, A.J., "The defense substance allicin from garlic permeabilizes membranes of *Beta vulgaris*, *Rhoeo discolor*, *Chara corallina* and artificial lipid bilayers", *Biochimica et Biophysica Acta (BBA) - General Subjects*, 1850(4), 602-611, 2015. Doi: 10.1016/j.bbagen.2014.11.020.

[29] Miron, T., Rabinkov, A., Mirelman, D., Wilchek, M., Weiner, L., "The mode of action of allicin: its ready permeability through phospholipid membranes may contribute to its biological activity", *Biochimica et Biophysica Acta (BBA)*, 1463(1), 20-30, 2000. Doi: 10.1016/s0005-2736[99]00174-1.

[30] Kučerka, N., Nieh, M., Pencer, J., Sachs, J., Katsaras, J., "What determines the thickness of a biological membrane", *General Physiology and Biophysics*, 28(2), 117-125, 2009. Doi: 10.4149/gpb_2009_02_117.

[31] Balakrishnan, M., Kenworthy, A.K., "Lipid peroxidation drives liquid-liquid phase separation and disrupts raft protein partitioning in biological membranes", BioRxiv [Preprint]. 2023.09.12.557355, 2023. Update in: *Journal of the American Chemical Society*, 146(2), 1374-1387, 2024. Doi: 10.1101/2023.09.12.557355.

[32] Zhang, Z., Lei, M., Liu, R., Gao, Y., Xu, M., Zhang, M., "Evaluation of Alliin, Saccharide Contents and Antioxidant Activities of Black Garlic During Thermal Processing", *Journal of Food Biochemistry*, 39(1), 39-47, 2015. Doi: 10.1111/jfbc.12102.

[33] Xiao, H., Parkin, K.L., "Antioxidant Functions of Selected Allium Thiosulfinates and S-Alk[en]yl-L-Cysteine Sulfoxides", *Journal of Agricultural and Food Chemistry*, 50(9), 2488-2493, 2002. Doi: 10.1021/jf011137r.

[34] Bhandari, S.R., Yoon, M.K., Kwak, J.H., "Contents of Phytochemical Constituents and Antioxidant Activity of 19 Garlic [*Allium sativum* L.] Parental Lines and Cultivars", *Horticulture, Environment, and Biotechnology*, 55, 138-147, 2014. Doi: 10.1007/s13580-014-0155-x.

[35] Horn, A., Jaiswal, J.K., "Structural and signaling role of lipids in plasma membrane repair", *Current Topics in Membranes*, 84, 67-98, 2019. Doi: 10.1016/bs.ctm.2019.07.001.

[36] Furdak, P., Bartosz, G., Stefaniuk, I., Cieniek, B., Bieszczad-Bedrejczuk, E., Soszyński, M., Sadowska-Bartosz I., "Effect of Garlic Extract on the Erythrocyte as a Simple Model Cell", *International Journal of Molecular Sciences*, 25(10), 5115, 2024. Doi: 10.3390/ijms25105115.

[37] Tsuchiya, H., Nagayama, M., "Garlic allyl derivatives interact with membrane lipids to modify the membrane fluidity", *Journal of Biomedical Science*, 15(5), 653-660, 2008. Doi: 10.1007/s11373-008-9257-8.

[38] Pinilla, C.M.B., Thys, R.C.S., Brandelli, A., "Antifungal properties of phosphatidylcholine-oleic acid liposomes encapsulating garlic against environmental fungal in wheat bread", *International Journal of Food Microbiology*, 293, 72-78, 2019. Doi: 10.1016/j.ijfoodmicro.2019.01.006.

[39] Lu, Q., Lu, P.-M., Piao, J.-H., Xu, X.-L., Chen, J., Zhu, L., Jiang, J.-G., "Preparation and physicochemical characteristics of an allicin nanoliposome and its release behavior", *LWT - Food Science and Technology*, 57(2), 686-695, 2014. Doi: 10.1016/j.lwt.2014.01.044.

[40] Rønnest, A.K., Peters, G.H., Hansen, F.Y., Taub, H., Miskowiec, A., "Structure and dynamics of water and lipid molecules in charged anionic DMPG lipid bilayer membranes", *The Journal of Chemical Physics*, 144(14), 144904, 2016. Doi: 10.1063/1.4945278.

Middle East Journal of Science

Research Article

OPTICAL, MORPHOLOGICAL, STRUCTURAL, AND PHOTOCATALYTICAL PROPERTIES OF PLASMONIC AU NPS PRODUCED BY PULSED LASER DEPOSITION

İlhan CANDAN* [ID] *[1] Serap YİĞİT GEZGİN* [ID] *[2] Hadice BUDAK GÜMGÜM [3]* [ID]
Hamdi ŞÜKÜR KILIÇ[2,4,5] [ID]

[1] Dicle University, Faculty of Science, Department of Physics, Diyarbakir, Türkiye
[2] Selcuk University, Faculty of Science, Department of Physics, Konya, Türkiye
[3] Dicle University, Faculty of Science, Department of Physics, Diyarbakir, Türkiye
[4] University of Selçuk, High Technology Research and Development Center (ILTEK), Konya, Türkiye
[5] University of Selçuk, Directorate of Laser Induced Proton Therapy App. and Research Center, Konya, Türkiye
* Corresponding author; ilhan.candan@dicle.edu.tr

Abstract: *Plasmonic Au NPs exhibit exceptional optical, morphological, and structural properties, making them promising materials for applications in photocatalysis, sensing, and energy conversion. This study explores the synthesis and characterization of plasmonic gold NPs produced by pulsed laser deposition, a versatile physical vapor deposition technique. Pulsed Laser Deposition enables precise control over NP formation through tunable parameters such as laser fluence, ambient gas environment, and deposition duration. The resulting NPs were systematically analyzed to evaluate their optical properties, including localized surface plasmon resonance, as well as their morphological and structural attributes. The localized surface plasmon resonance behavior of the synthesized Au NPs was found to be highly dependent on particle size, shape, and distribution, as revealed by UV-Vis spectroscopy and electron microscopy. Structural analysis via X-ray diffraction confirmed the crystalline nature of the NPs, with lattice parameters correlating to their stability and catalytic efficiency. Photocatalytic activity tests demonstrated that the gold NPs could effectively degrade organic pollutants under visible light, leveraging their strong LSPR-induced hot electron generation and charge transfer properties. In this study, gold NP thin film was produced on microscopic glass by Pulsed Laser Deposition system. Gold NPs thin film photocatalyst efficiency 95.00% and reaction rate constant 0.39 min^{-1} were calculated. At the end of 210 min, MB dye was degraded and turned into high transparency due to localized surface plasmon resonance property of gold NP. The findings may provide valuable insights into the design and application of plasmonic Au NPs in photocatalysis and other advanced technologies.*

Keywords*: Au NP, thin film, PLD, LSPR; photocatalyst*

1. Introduction

Plasmonic Gold nanoparticles (Au NPs) have garnered significant attention in recent years due to their unique optical, morphological, and structural properties, which make them highly versatile for applications in fields such as photonics, sensing, biomedicine, and environmental remediation [1-5]. One of their most compelling features is the localized surface plasmon resonance (LSPR) phenomenon, wherein the conduction electrons on NP surface oscillate coherently in response to incident light [6-8]. This results in strong light absorption and scattering in the visible and near-infrared regions, which can be finely tuned by manipulating the size, shape, and surrounding medium of the NPs. In addition to their

remarkable optical properties, AuNPs exhibit high stability, biocompatibility, and catalytic activity, making them attractive candidates for photocatalytic applications such as pollutant degradation and solar energy harvesting [9-11].

The synthesis of Au NPs is a critical determinant of their properties and subsequent performance. Among the various methods available, PLD has emerged as a powerful technique for producing plasmonic NPs with tailored characteristics [12-14]. PLD involves ablating a gold target using high-energy laser pulses in a controlled environment, leading to the formation of NPs with unique properties that are challenging to achieve through conventional chemical synthesis. This physical deposition method offers several advantages, including the ability to operate in solvent-free environments, precise control over deposition parameters, and the capacity to produce NPs with uniform size distributions and minimal chemical contamination. Furthermore, using PLD allows for the customization of NP properties by adjusting key parameters such as laser fluence, ambient gas type and pressure, and substrate material [15].

The optical, morphological, and structural characteristics of Au NPs synthesized by PLD have been extensively studied to understand their correlation with functionality. For example, the size and shape of NPs, as well as their surface roughness and spatial distribution, significantly influence their LSPR behavior and photocatalytic activity [16]. Morphological tuning can enhance light absorption efficiency and increase the density of reactive sites, thus improving photocatalytic performance [17, 18]. Structural properties, such as crystallinity and lattice defects, also play a critical role in determining NPs' stability and catalytic activity.

In addition to their intrinsic properties, plasmonic Au NPs are increasingly being explored for photocatalysis, where they act as light absorbers, charge carriers, or electron mediators to drive chemical reactions under light irradiation [19, 20]. The strong LSPR effect enhances local electromagnetic fields and facilitates the generation of hot electrons, which can be transferred to adsorbed molecules to initiate catalytic reactions. Such properties make Au NPs highly effective for environmental applications, including the degradation of organic pollutants and the reduction of toxic compounds. However, optimizing their photocatalytic performance requires a detailed understanding of the interplay between their structural, morphological, and optical attributes.

This study investigates the optical, morphological, structural, and photocatalytic properties of Au NPs synthesized using PLD. By systematically analyzing these attributes, we aim to establish a comprehensive understanding of how the synthesis conditions influence NP performance. The findings provide valuable insights into the design and application of plasmonic Au NPs in photocatalysis and other advanced technologies.

2. Materials and Methods

2.1. Experimental

The synthesis of gold Au NPs was performed using PLD system. The process employed a pulsed Nd:YAG laser operating at a fundamental wavelength of 1064 nm, with pulse durations of 5 ns and a repetition rate of 10 Hz. This laser system is capable of generating second, third, and fourth harmonics at wavelengths of 532 nm, 355 nm, and 266 nm, respectively. For this study, the fundamental wavelength of 1064 nm was selected. A neutral density filter was utilized to control the laser pulse energy before focusing the beam using a lens, as depicted in Fig. 1a.

Glass microscope slides were used as substrates for depositing Au NPs. These substrates were meticulously cleaned using a multi-step procedure involving soap solution, followed by sequential rinsing with isopropyl alcohol and acetone, each for 15 minutes. The cleaning process was further enhanced by ultrasonic treatment, and the substrates were dried using a nitrogen gas stream.

Commercially available high-purity Au sputtering targets (99.99%, Plasmaterials, USA) were used. To ensure uniform ablation and prevent damage to the targets, both the targets and substrates were mounted on independently rotating holders, allowing each laser pulse to strike a fresh area of the target. This setup produced homogeneous NP coatings, as shown in Fig. 1a. The target-to-substrate distance was fixed at 5 cm, and laser deposition was carried out at room temperature.

For the experiments, the laser energy was changed from 15, 20, 25, and 35 mJ per pulse for Au(1), Au(2), Au(3), and Au(4), respectively. The laser beam was focused onto the targets using a lens with a focal length of 50 cm, and the beam was oriented at a 45° angle to the target surface. The energy density for 35 mJ pulse increases significantly to about 2.43 MJ/m² (or 242.81 J/cm²) due to a smaller focused spot size at the focal point. The experiments were conducted in a high vacuum environment, maintaining a pressure of approximately 5×10^{-7} mbar. Different NP sizes were achieved by varying the laser power at fixed pulse number applied to the targets. Au(1), Au(2), Au(3), and Au(4) thin films corresponded to 6,000 laser pulses as the laser power varied as 15, 20, 25, and 35 mJ per pulse, respectively. The optical properties of Au NPs were obtained by UV-Vis-NIR spectroscopy (V-670 Jasco, Japan). The Au(4) sample was further investigated by obtaining the following analysis. The morphological and structural properties of Au(4) NPs were investigated by Atomic Force Microscopy (AFM) (NT-MDT/Ntegra Solaris, Ireland), Scanning Electron Microscopy (SEM) (ZEISS EVO LS10, Germany), and X-Ray Diffraction (XRD) (BRUKER D8 ADVANCE, Germany), respectively.
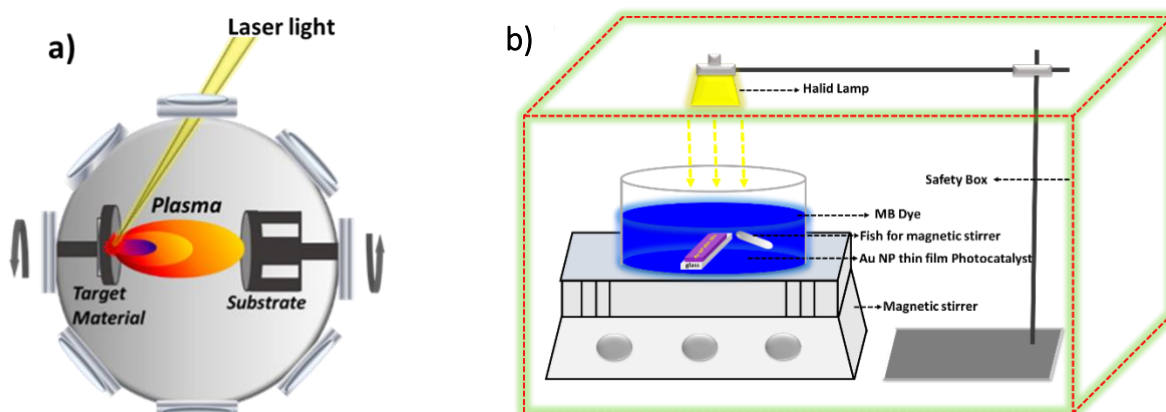
Figure 1. a) The schematic images of PLD and **b)** the photocatalyst systems

100 ml of MB dye was poured into the container in Figure 1b. The fish stirrer and Au NP thin film were placed in the solution and 1000 microliters of base solution (pH=10) were added. The magnetic stirrer was turned on and first kept in the dark for 30 minutes, then liquid was taken under visible light (250 W metal halide lamp (GE ARC250)) every 30 minutes for up to 210 minutes.

3. Results and Discussion

3.1. Structural Properties

Figure 2 shows XRD spectrum of produced plasmonic Au NPs. Peak at ~20°; this peak likely corresponds to the amorphous nature of soda-lime glass, primarily from SiO_2 (silicon dioxide). Peak at ~30°; this peak may arise due to $CaCO_3$ (calcium carbonate) or other crystalline impurities like Na_2SiO_3 present in soda-lime glass. Crystalline calcium-containing compounds can produce reflections in this region, especially under deposition or heat treatment processes. Peak at ~40°; this peak corresponds to the (111) diffraction plane of gold (Au) in a face-centered cubic (FCC) structure. For gold, the (111) peak typically appears at $2\theta \approx 38.2°$ for Cu Kα radiation. Nanoparticle size effects, strain, or substrate interactions can cause slight shifts or broadening of the peak. The expected XRD peaks at 2θ values of 38.18°, 44.38°, 64.57°, and 77.56° correspond to (111), (200), (220), and (311) planes of Au NPs, although the last three peaks are not visible in the XRD spectrum. These diffraction peaks align with the face-centered cubic phase of gold, as referenced in JCPDS file 65-2870 [21, 22]. In the literature, similar research on XRD pattern has been reported for biosynthesized Au NPs, indicating a face-centered cubic structure [23].
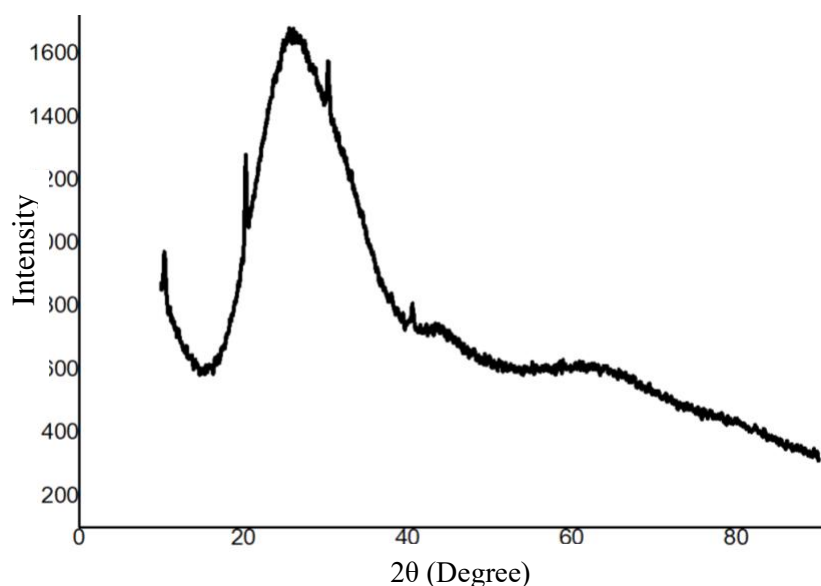
Figure 2. XRD spectrum of plasmonic Au(4) NPs.

3.2. Optical Properties

The optical properties of the produced Au NPs were investigated by UV-Vis-NIR spectroscopy as shown in Figure 3. LSPR peaks of Au NPs were measure to be 925, 685, 655, and 600 nm for Au(1), Au(2), Au(3), and Au(4), respectively. The peaks appeared at the regions of visible as well as infrared spectra. As the laser power increased, LSPR peaks shifted to longer wavelengths (redshift). The reason is at low laser power, small sized Au NPs were produced, and thus, the wavelength of LSPR peak is relatively shorter. Whereas at higher laser power, the larger Au NPs were produced and therefore, the peaks are at longer wavelength.
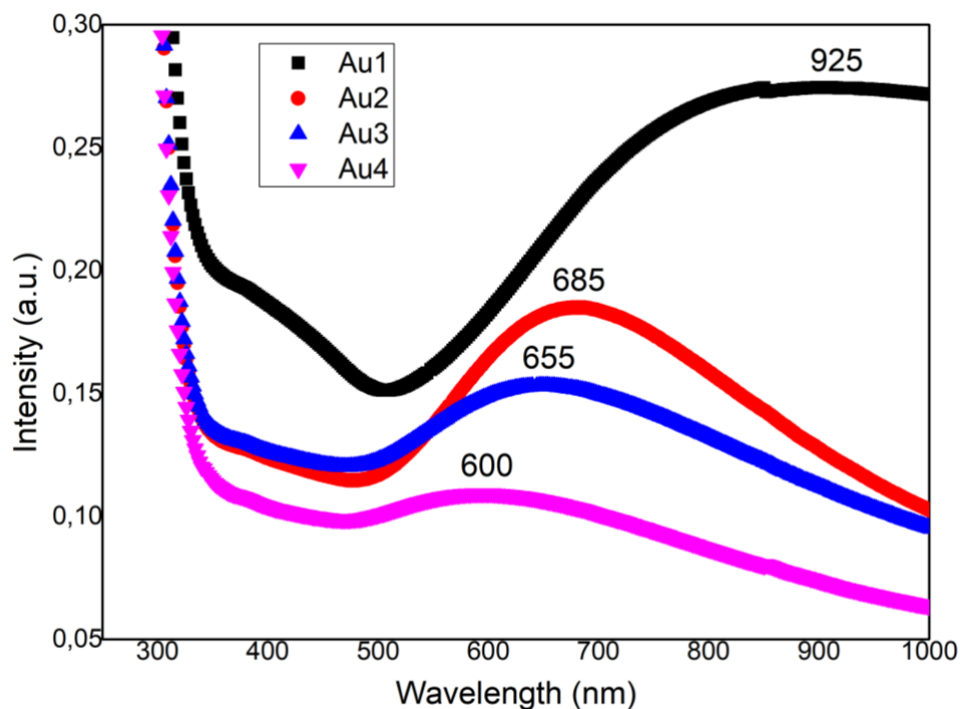
Figure 3. LSPR peak of produced plasmonic Au NPs. The peaks ranges from 600 to 925 nm as the laser power varied.

3.3. Morphological Properties

Figure 4 and 5 illustrates the 2D and 3D AFM images of produced Au NPs. As can be deduced from the pictures, NP sizes are around 100 nm. Roughness values are as follows: S_y= 154.9 nm, S_z = 76.0 nm, Average = 26.5 nm, S_a = 4.9 nm, S_q = 10.1 nm, S_{sk} = 4.7 nm, S_{ka} = 33.9 nm.
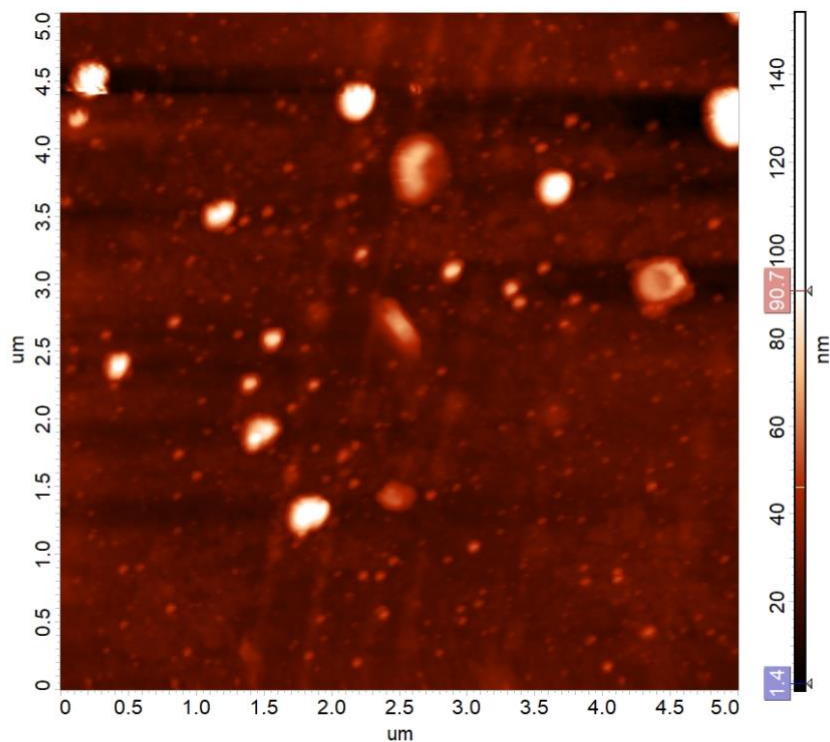
Figure 4. 2D-AFM image of plasmonic Au(4) NPs.
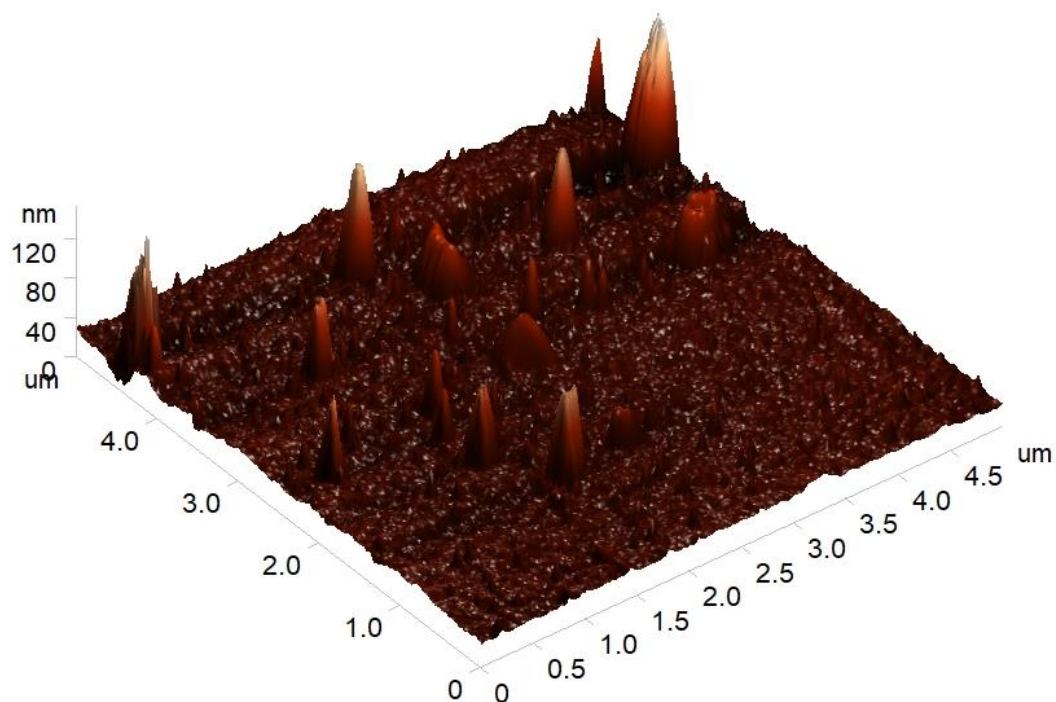
Figure 5. 3D-AFM image of plasmonic Au(4) NPs.

Figure 6 shows SEM image of produced Au NPs and inset of the left demonstrate Au NP thin film that is fabricated on a glass in the lab. The images provide that the produced Au NPs are spherical in shape and the particles are almost uniformly distributed on the glass.
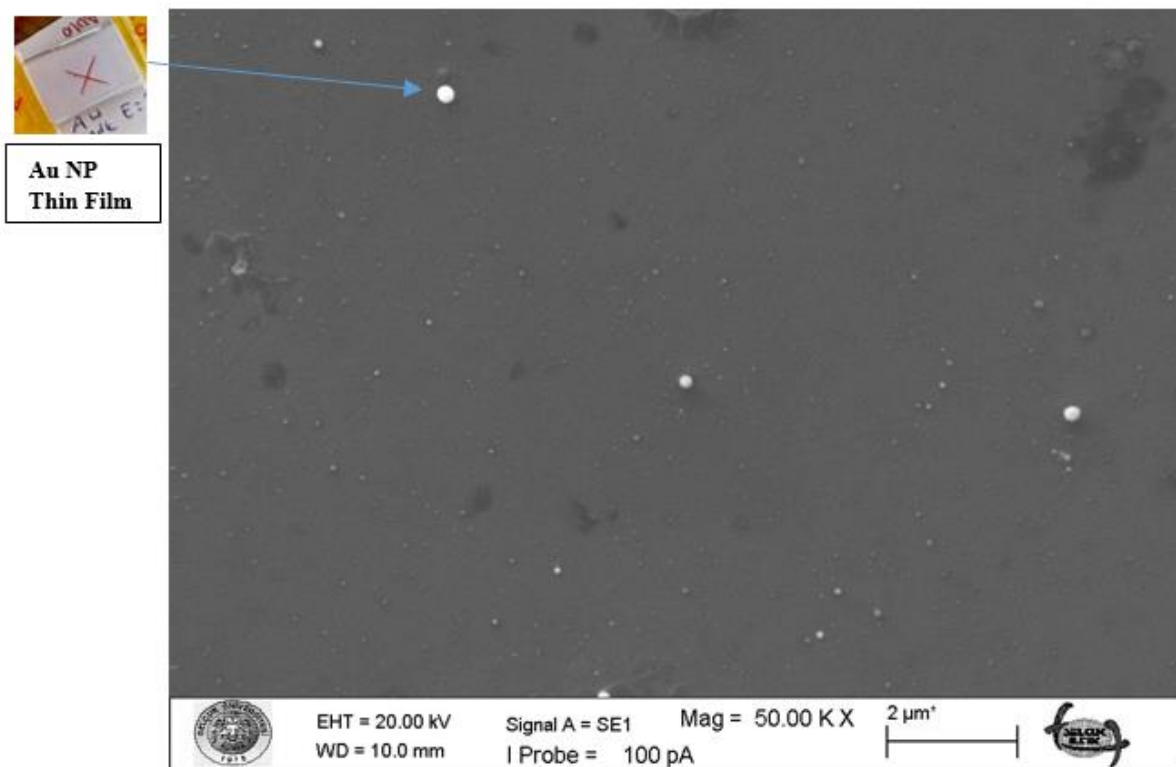
Figure 6. SEM image of plasmonic Au(4) NPs.

The EDS (Energy Dispersive X-ray Spectroscopy) spectrum provided shows the elemental composition of a thin film of Au nanoparticles deposited on a soda-lime glass substrate via Pulsed Laser Deposition shown in the Figure 7. The analysis of the key features can be mentioned as follows. Elements Identified as: Si (Silicon) has a high-intensity peak, likely from the glass substrate. O (Oxygen) stems from the silica (SiO_2) and other oxides in the soda-lime glass. Na (Sodium) has a smaller peak, common in soda-lime glass as Na_2O (sodium oxide). Ca (Calcium) has clearly visible peaks, which is characteristic of CaO (calcium oxide) in soda-lime glass. Mg (Magnesium) has a minor peak, a trace element often present in glass formulations. Au (Gold) has low-intensity peaks corresponding to the deposited gold nanoparticles.
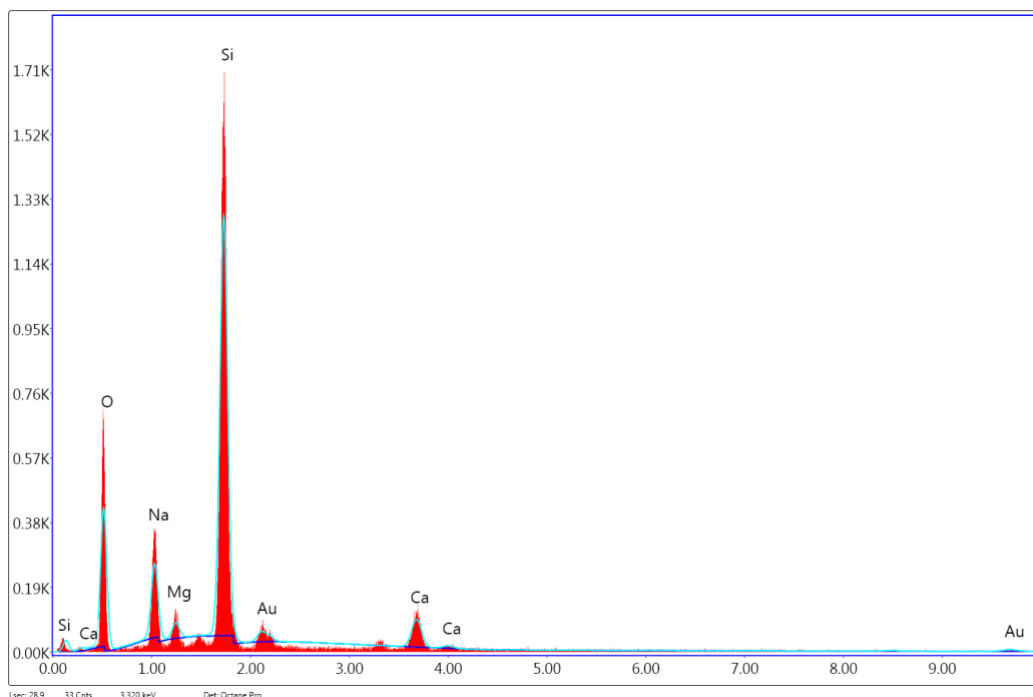
Figure 7. EDS graph of Au(4) NPs produced on soda lime glass by Pulsed laser deposition.

Peak Intensities reveals the following. Si shows the most intense peak, which confirms that the substrate (glass) dominates the composition. O reflects the oxygen bound to silicon (SiO_2) and calcium (CaO). Au peaks for gold (Au) appear at higher energy levels (~2.1 and ~9.7 keV), consistent with characteristic X-rays for Au. However, the intensities are much lower than the substrate peaks, indicating a thin film or low Au concentration. The Au peaks confirm the presence of deposited gold nanoparticles. This result aligns with the expected composition for Au nanoparticles deposited on a soda-lime glass substrate using Pulsed Laser Deposition.

3.4. Photocatalytic Properties of Au NP Thin Film

Industrial dye components, especially those originating from factories, cause environmental pollution and cause significant damage to the environment and human health. The transformation of these organic dye components into clean forms and their reusability in nature is important for the continuity of nature and human life. One of the application areas used to eliminate or reduce environmental pollution caused by wastewater is photocatalysis method. In this study, Metilen Blue (MB) dye, an organic pollutant, was removed by Au NP thin film produced by PLD. First, Au NP thin film was placed into MB organic dye and then a base solution with pH = 10 was added into it. In the dark for 30 min., MB dye was degraded to a negligible scale in the presence of Au NP thin film. However, at the end of 210 min, MB dye was degraded considerably in the presence of Au NP thin film

and a photocatalyst efficiency was determined to be 95.00 % as seen in Fig 8a. Under the condition of no Au NP thin film, the degradation of MB is very low and insignificant.
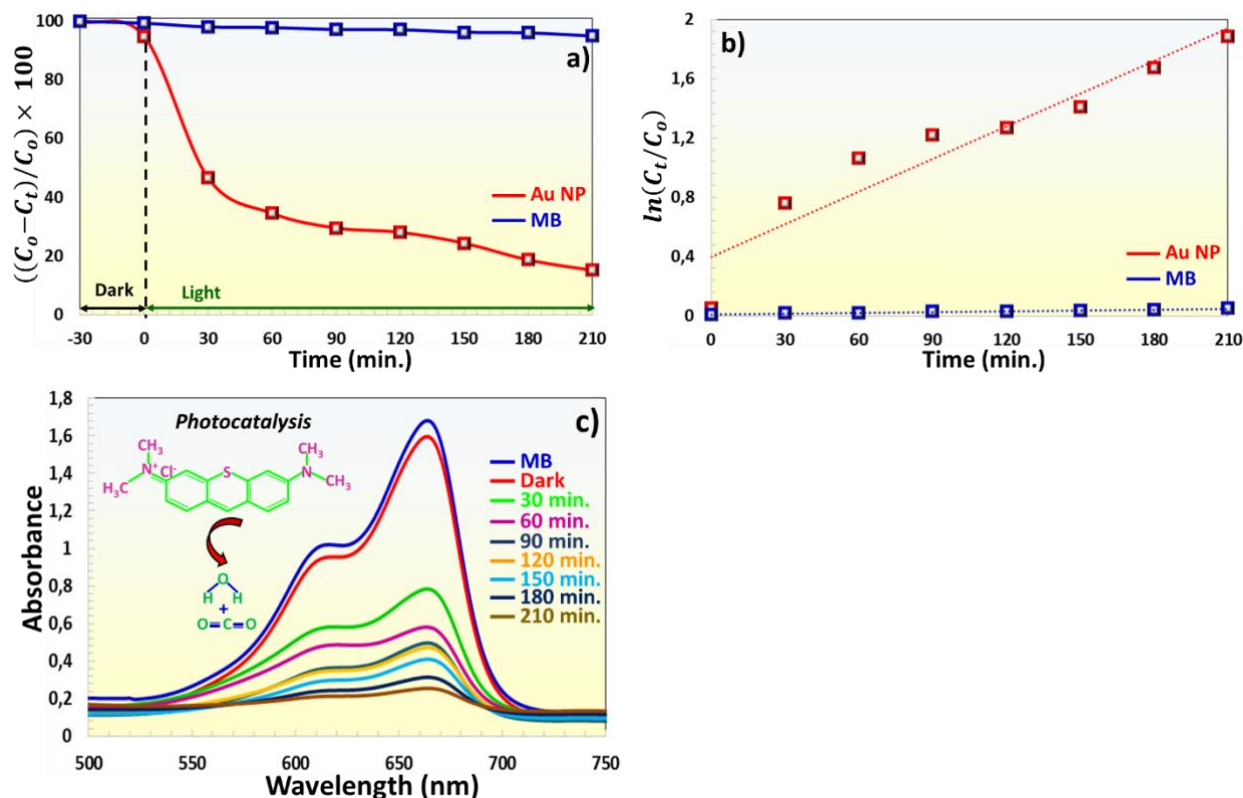
Figure 8. a) The effect on degradation of Au(4) NP thin film grown by the PLD method**, b)** First-order kinetic data of Au NP thin film photocatalyst, and **c)** Real-time absorption spectrum of MB dye in the presence of Au NP thin film (MB degradation mechanism is given as inset in c)

The Langmuir–Hinshelwood first-order kinetic model $\left(ln\left(\frac{c_t}{c_o} \right) = kt \right)$ was used to evaluate the photocatalytic activity of Au NP thin film in Figure 8b [24]. The degradation reaction rate constant of MB dye without using any catalyst was found to be 0.098 min^{-1}. When Au NP thin film photocatalyst was used, the reaction rate constant was determined as 0.39 min^{-1}. The real degradation graph in the Figure. 8c shows the absorption spectrum of Au NP photocatalyst at 210 min. The absorption peak of MB dye is on 666 nm wavelength, when it is exposed to visible light, the intensity of the absorption peak of this dye decreases in the presence of Au NP thin film every 30 min and becomes invisible at the end of 210 min. The reaction mechanism of the photocatalyst is given in the inset image in Figure 8.
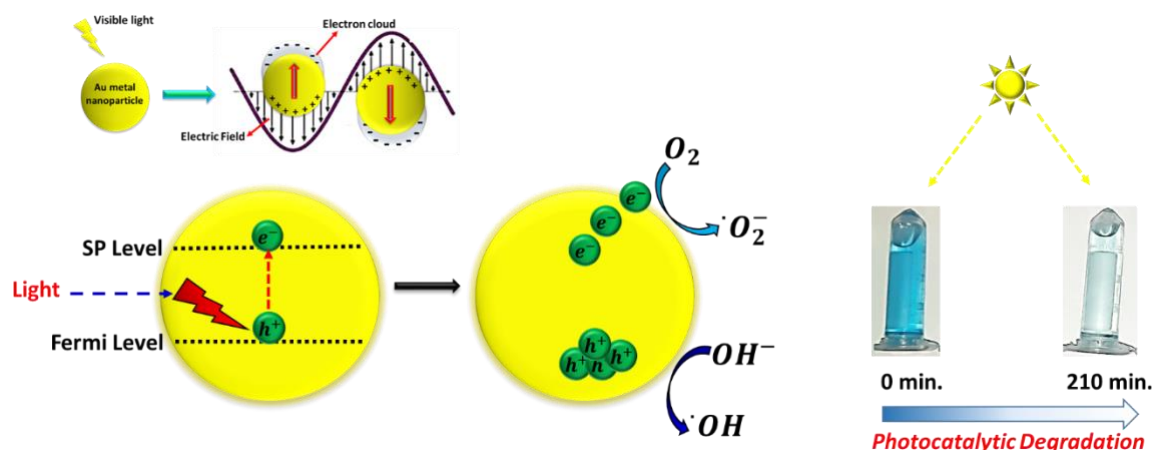
Figure 9. The schematic diagram of MB dye removal by Au NP thin film photocatalysts under visible light

The high-performance photocatalyst event was realized due to LSPR peak property of Au NPs. When visible wavelength light falls on the plasmonic metal Au NP, the electrons in the fermi level of Au are excited and transition to the Surface Plasmon (SP) band [25], causing the formation of $e^- - h^+$ pairs as seen in Figure 9. The released electrons oscillate in resonance as shown in the inset of Figure 9. under the influence of the electromagnetic wave. While the electrons collect on one side of the particle, the holes collect on the other side [26, 27]. The electrons in SP band react with O_2 to form $\cdot O_2^-$ radical [10, 20, 28], while the holes react with water molecules to form hydroxyl ($\cdot OH$) radicals [24]. As a result, the degradation of MB dye occurs and the blue colour of MB dye in Figure 9 became transparent within 210 minutes.

4. Conclusion

This study demonstrates the successful synthesis of Plasmonic AuNPs using PLD and provides a comprehensive analysis of their optical, morphological, structural, and photocatalytic properties. PLD technique proves to be a robust and versatile method for producing high-quality Au NPs, with the ability to precisely control particle size, distribution, and surface characteristics through adjustable deposition parameters. These controllable attributes enable fine-tuning of the NPs' LSPR properties, which are critical for their performance in optical and photocatalytic applications.

Morphological and structural analyses revealed that the synthesized Au NPs possess uniform size distributions, well-defined shapes, and high crystallinity, all of which are essential for stability and functionality. The interplay between particle size and the surrounding medium was shown to significantly influence their LSPR behavior, as characterized by UV-Vis spectroscopy. Structural investigations using X-ray diffraction confirmed that the crystalline nature of the Au NPs, coupled with minimal lattice defects, plays a vital role in enhancing their photocatalytic efficiency.

Photocatalyst performance of Au NP thin film on MB dye degradation was investigated. Au NP thin film photocatalyst efficiency of 95.00% and reaction rate constant 0.39 min^{-1} were calculated. At the end of 210 min, MB dye was degraded and turned into high transparency due to LSPR property of Au NP. The photocatalytic activity of these Au NPs, evaluated through the degradation of organic pollutants under visible light, demonstrated their potential for environmental remediation applications. The strong LSPR effect facilitated efficient light absorption and hot electron generation, which enhanced charge transfer processes and catalytic reaction rates. The results indicate that the photocatalytic performance of Au NPs can be optimized by tailoring their structural and morphological properties during the synthesis process.

In conclusion, PLD emerges as a powerful and clean fabrication method for designing plasmonic Au NPs with highly desirable optical and catalytic properties. The findings of this study provide valuable insights into the relationships between synthesis parameters, NP properties, and their functional performance. These insights contribute to the broader understanding and application of plasmonic materials in fields such as photocatalysis, sensing, and energy conversion. Future work should focus on further optimizing PLD process and exploring hybrid systems where Au NPs can be integrated with other materials to enhance synergistic effects for advanced applications in environmental and energy technologies.

Ethical Statements

The author declares that this document does not require ethics committee approval or special permission. Our study does not cause any harm to the environment.

Acknowledgment

Conflict of interest

The authors declare no conflict of interest.

Authors Contributions

SYG and IC carried out calculations and wrote the first draft of the manuscript. IC and SYG carried out the experiments. HBG and HSK supervised the projects. All authors discussed the results and contributed to the final manuscript.

References

[1] Ghobashy, M. M., et al., "NPAu NPsin microelectronics advancements and biomedical applications". *Materials Science and Engineering: B*, 301, 117191, 2024.

[2] Zare, I., et al., "Gold nanostructures: synthesis, properties, and neurological applications", *Chemical society reviews*, 51(7), 2601-2680, 2022.

[3] Ramacha ndran, T., et al., "Gold on the horizon: unveiling the chemistry, applications and future prospects of 2D monolayers of NPAu NPs(Au-NPs)"*, Nanoscale Advances*, 6(22), 5478-5510, 2024.

[4] Burlec, A.F., et al., "Current overview of metal NPs' synthesis, characterization, and biomedical applications, with a focus on silver and gold NPs"*. Pharmaceuticals,* 16(10), 1410, 2023.

[5] Candan, I., et al., "Sensor properties of plasmonic silver and NPAu NPsproduced by pulsed laser deposition", *Journal of Optoelectronics and Advanced Materials*, 26(5-6), 186-198, 2024.

[6] Agrawal, A., et al., "Localized surface plasmon resonance in semiconductor nanocrystals"*. Chemical reviews,* 118(6), 3121-3207, 2018.

[7] Prabowo, B.A., Purwidyantri, A., Liu, K. C., "Surface plasmon resonance optical sensor: A review on light source technology", *Biosensors,* 8(3), 80 2018.

[8] Candan, İ., et al., "Biosensor Properties Of Plasmonic Silver Nps Produced By Pld", *Middle East Journal of Science,* 7(2), 112-122, 2021.

[9]   Ahmad, I., et al., "A comprehensive review on the advancement of transition metals incorporated on functional magnetic nanocomposites for the catalytic reduction and photocatalytic degradation of organic pollutants". *Coordination Chemistry Reviews*, 514: 215904, 2024.

[10] Dhiman, M., "Plasmonic nanocatalysis for solar energy harvesting and sustainable chemistry", *Journal of Materials Chemistry A*, 8(20), 10074-10095, 2020.

[11] Gellé, A., Moores, A., "Plasmonic NPs: Photocatalysts with a bright future", *Current Opinion in Green and Sustainable Chemistry*, 15, 60-66, 2019.

[12] Kukreja, L.M., et al., "Pulsed laser deposition of plasmonic-metal nanostructures", *Journal of Physics D: Applied Physics,* 47(3), 034015, 2013.

[13] Gezgin, S.Y., Kepceoğlu, A., Kılıç, H.Ş., "An investigation of localised surface plasmon resonance (LSPR) of Ag NPs produced by pulsed laser deposition (PLD) technique", AIP Conference Proceedings, AIP Publishing LLC, 2017.

[14] Gezgin, S.Y., Kepceoğlu, A., Kılıç, H.Ş., "An experimental investigation of localised surface plasmon resonance (LSPR) for Cu NPs depending as a function of laser pulse number in Pulsed Laser Deposition"*, AIP Conference Proceedings, AIP Publishing LLC, 2017.

[15] Yu, J., et al., "Recent Advances on Pulsed Laser Deposition of Large-Scale Thin Films", *Small Methods*, 8(7), 2301282, 2024.

[16] Dal'Toé, A.T., et al., "Lanthanum doped titania decorated with silver plasmonic NPs with enhanced photocatalytic activity under UV-visible light", *Applied Surface Science,* 441, 1057-1071, 2018.

[17] Ou, W., et al., "Plasmonic metal nanostructures: concepts, challenges and opportunities in photo-mediated chemical transformations", *Iscience*, 24(2), 101982, 2021.

[18] Desseigne, M., et al., "Plasmonic Photocatalysts Based on Au NPs and WO3 for Visible Light-Induced Photocatalytic Activity". *Catalysts*, 13(10), 1333, 2023.

[19] Yuan, L., et al., "Sustainable chemistry with plasmonic photocatalysts", *Nanophotonics*, 12(14): 2745-2762, 2023.

[20] Khan, M.E., Cho, M.H., Surface plasmon-based nanomaterials as photocatalyst, Advanced Nanostructured Materials for Environmental Remediation, 25, pp. 173-187, 2019.

[21] Sundararajan, B., Kumari, B.R., "Novel synthesis of NPAu NPsusing Artemisia vulgaris L. leaf extract and their efficacy of larvicidal activity against dengue fever vector Aedes aegypti L", *Journal of Trace Elements in Medicine and Biology*, 43, 187-196, 2017.

[22] Oliveira, A.E.F., et al., "Gold NPs: a didactic step-by-step of the synthesis using the turkevich method, mechanisms, and characterizations"*, Analytica*, 4(2), 250-263, 2023.

[23] Balasubramani, G., et al., "GC–MS analysis of bioactive components and synthesis of gold NP using Chloroxylon swietenia DC leaf extract and its larvicidal activity", *Journal of Photochemistry and Photobiology B: Biology,* 148, 1-8, 2015.

[24] Dursun, S., et al., "Investigation of photocatalytic activity (under visible light) of ultrathin CZTS films produced in different thicknesses by PLD method", *Optical and Quantum Electronics,* 55(2), 166, 2023.

[25] Yiğit Gezgin, S., Kiliç, H. Ş., "The effect of Ag plasmonic NPs on the efficiency of CZTS solar cell: an experimental investigation and numerical modelling", *Indian Journal of Physics*, 97(3), 779-796, 2023.

[26] Gezgin, S.Y., Kepceoğlu, A., Kılıç, H. Ş., "An investigation of localised surface plasmon resonance (LSPR) of Ag NPs produced by pulsed laser deposition (PLD) technique", AIP Conference Proceedings, AIP Publishing, 2017.

[27] Gezgin, S.Y., Kepceoğlu, A., Kılıç, H. Ş., "An experimental investigation of localised surface plasmon resonance (LSPR) for Cu NPs depending as a function of laser pulse number in Pulsed Laser Deposition", AIP Conference Proceedings, AIP Publishing, 2017.

[28] Verma, P., et al., "Plasmonic nanocatalysts for visible-NIR light induced hydrogen generation from storage materials"*, Mater. Adv.* 2, 880–906, 2021.

Middle East Journal of Science

Research Article

OBSERVATIONS ON THE WINTERING OF WHITE-STORK *CICONIA CICONIA* (LINNAEUS, 1758) FROM SOUTH-EASTERN PART OF TÜRKİYE

Recep KARAKAŞ

Department of Biology, Faculty of Science, University of Dicle, 21280 Diyarbakir, Türkiye
Corresponding author; rkarakas@dicle.edu.tr

Abstract: *Between the January 2019 and January 2023 periods, 108 individuals of White-stork Ciconia ciconia (Linnaeus, 1758) have been recorded during winter seasons that covering only December and January months. White-storks determined between Diyarbakır and Batman provinces from 12 different locations and also nearly all of the records obtained within the boundaries of the Bismil Plain IBA's between Diyarbakır and Batman provinces. The wintering of species in this part of Türkiye and Diyarbakır province have been firstly documented. The availability of suitable habitat's together with food possibilities and mild climate conditions may have been supports the population increase in the area during all year round. This study showed that White-storks have found the favourable conditions for wintering in our region and have now started to wintering. Monitoring of the wintering population in the region is recommended for evaluate changes in size of population and range expansion of species in the area by a comprehensive field study in this part of country.*

Keywords: *White-stork, Ciconia ciconia, wintering population, South-east Anatolia, Türkiye.*

1. Introduction

The White-stork *Ciconia ciconia* (Linnaeus, 1758) is a polytypic (*C. ciconia ciconia and C. ciconia asiaticus*) and large migratory bird species belong to Ciconidae family [1,2]. It has a large distribution range in most of Palearctic region [3], including Türkiye. Europe constitutes more than 75% of the global breeding area while the remaining areas are found in north-west Africa, south-west Asia, mainly [1,4,5]. The White-stork populations showed decrease during the almost the entire 20th century due to conventional reasons such as agricultural intensification and habitat loss, resulting in species categorised in ''near threatened'' globally in 1988 and of Species of European Concern (SPEC) Category 2 in Europe [4,6]. However, thanks to conservation efforts and reintroduction programs that conducted mainly in Europe, their population has increased [7]. Related to population increase and large distribution range, it is stated as "Least concern" (LC) species [8] recently, together with increasing trend in overall population's [3]. Recently, the global population size was reported as 700,000-704,000 individuals while European population is reported as 447,000-495,000 individuals [3,7]. Despite of the lack of current data, the size of breeding population in Turkey was given as 15,000-35,000 pairs [5].

The White-stork populations are stated as widespread summer visitor to much of Europe commonly [5], and migrate to their main wintering area in Africa following two main routes; via Gibraltar or Middle East [9,10]. The breeding population of species' in Türkiye and individuals passing through Türkiye to Europe use the migration route via the Middle East to Africa. In general, the species is revealed as a common summer migrant in Türkiye except some parts of Black Sea Coastlands where

species is reported as very local [11,12]. The species arrive to their breeding areas in Türkiye about the end of February / early March, and after the breeding activities between April - June, they start to autumn migration in end of July or early August. Türkiye is not only an important breeding area but also serves an important feeding and stopover site for transiting individuals during migration seasons. Also, there are some irregular wintering records from west, south, central and south eastern part of Türkiye in the past [12].

South-eastern part of Türkiye has a rich biodiversity including birds [13,14], owing to its evolutionary history, strategic geographic location and occurrence of the special habitats together with different climatically conditions. Accordingly, as a result of recent studies, 17 Important Bird Areas (IBA's) and 19 Key Biodiversity Areas (KBA's) have been identified in the region. Among these, the Bismil Plain is one of the important area sheltering many species including birds thanks to some small natural wetlands in plain and riverine habitats mainly concentrated around Tigris River [14]. The big portion of plain thanks to special habitats and biological components including some threatened bird species together with one of the largest known White-stork population, declared as both IBA's [15] and a KBA's [16].

Although irregular wintering records of White-storks have been reported in different locations from Turkey, no regular wintering record has been found for the South-eastern Anatolia Region and Diyarbakır surroundings. In this sense, wintering of White-storks has been reported for the first time in the region. Based on observations, the new wintering site for White-stork have been determined in Diyarbakır province together with some parts of Batman province from South eastern Anatolia region. It was aimed to reporting new wintering site together with contributing knowledge to the ecology of species.

2. Material and Method

The material of this study constituted from White-storks that were wintering in the South-east Anatolia Region, mainly around Diyarbakır province (Figure 1). The data obtained during regular and irregular field excursions performed in the region between 2019 and 2023 years were evaluated. Among the observations, records obtained during December and January months were taken into account as wintering individuals (Figure 2). Field excursions have been carried out by conventional ornithological equipment which is composed from field glasses (8×40), telescope (20-60×80), a camera (with a 400 mm lens), GPS (Magellan eXplorist 100) and ornithological handbook [17].

The Bismil Plain is situated between Diyarbakır and Batman provinces. The plain is mainly shaped around the Tigris River and its large and small branches that carry the waters together with a few natural ponds. In the plain, where the altitude range varies between 500-550 m, there are special habitats such as river beds, natural ponds, swamps, meadows, etc. and the area hosts a significant biodiversity in the region in connection with special habitats [13,14]. The plain is one of the 17 IBA's that was defined by Doğa Derneği and Birdlife International in Türkiye [16,18].
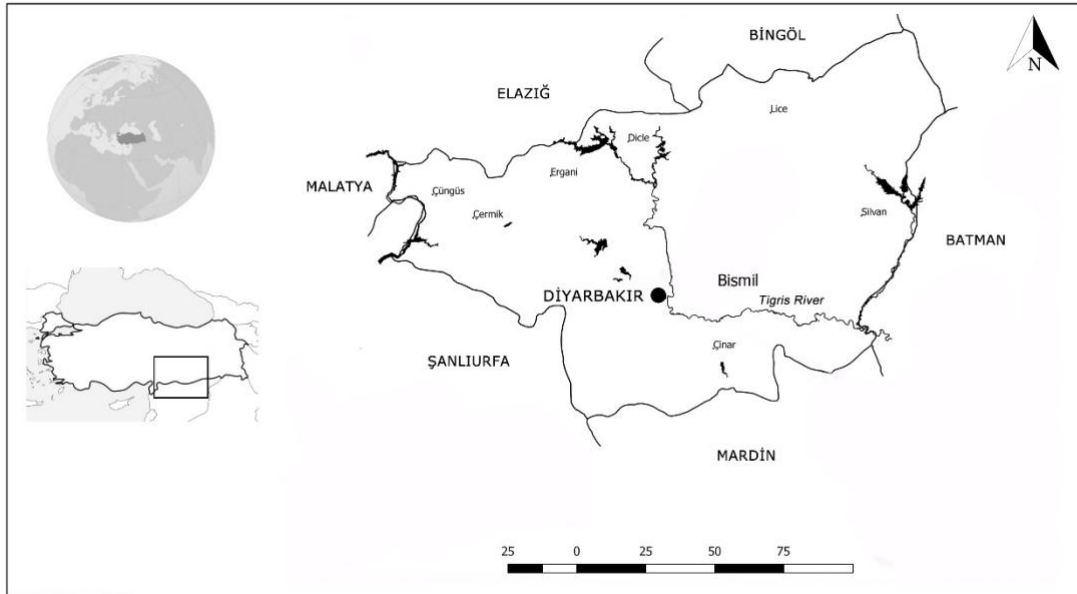
Figure 1. Map of the study area and location of the new wintering site

Figure 2. A group of White–storks together with Grey heron (*Ardea cinerea*) and Great heron (*Egretta alba*) between Diyarbakır-Batman provinces at 4 December 2021.

3. Results

Between the January 2019 and January 2023 periods, totally, 108 individuals of White-storks have been recorded during winter seasons that mean only December (64 individuals) and January (44 individuals) months. White-storks determined between Diyarbakır and Batman provinces from 8 locations (Table 1), mainly. All of the records obtained from some parts of Bismil Plain IBA's between

Diyarbakır and Batman provinces. The regular wintering of species in this part of Türkiye and Diyarbakır province have been firstly documented.

Table 1. The wintering records of White-stork in Diyarbakır and Batman provinces during 2019-2023 years

Location	Dates	Individual Numbers	GPS	Latitude
Batman bridge/Batman	06.01.2019	4	37 S 682754 / 4198312 N	539 m
Fidanlık/Diyarbakır	26.12.2020	11	37 S 614780 / 4186624 N	569 m
Batman River/Batman	02.01.2021	12	37 S 680306 / 4195974 N	532 m
Üçtepe/Bismil	04.12.2021	3	37 S 635966 / 4188229 N	555 m
Batman River/Batman	04.12.2021	42	37 S 679012 / 4194870 N	529 m
Bismil	15.01.2022	6	37 S 648301 / 4188964 N	537 m
Salat River/Bismil	11.12.2022	8	37 S 665148 / 4191786 N	531 m
Çöltepe/Bismil	08.01.2023	22	37 S 658165 / 4190953 N	562 m

Although there have been a few records of irregular wintering such as 1-2 pairs in the past, continuous wintering as in large groups has been determined for the first time in the region. Specially, the increase in the wintering records are remarkable for the last 4-5 years. Maximum 42 individual observed during December 2021 and followed by 22 individuals for January 2023 period. It is estimated that there has been an increase in wintering records in recent years and that this increase will probably continue in the future, when all records are analysed (Figure 3).
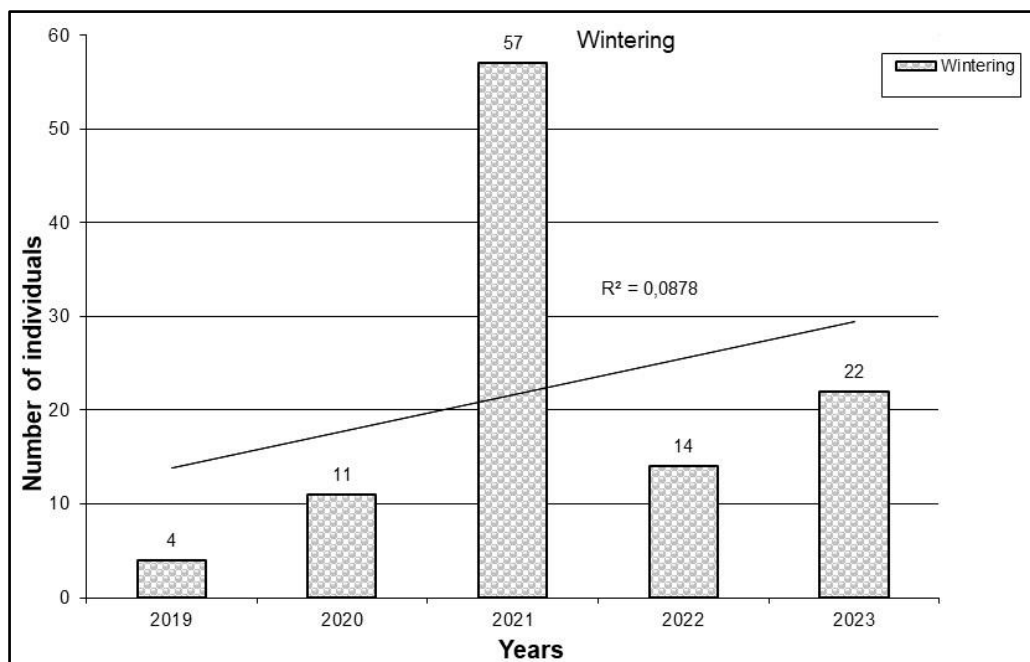
Figure 3. Number of individuals per year between 2019 and 2023 periods

Although ornithological observations were carried out in many different locations in the region for the related period, the species was determined only in this plain means that the area has suitable conditions for the wintering of the species in terms of both climate and feeding opportunities.

Bismil Plain was declared as IBA in 2004 [15] because it regularly supports significant breeding populations of the Great Bustard *Otis tarda* and the White-stork *Ciconia ciconia*, by meeting IBA A1 and B2 criteria, respectively for the mentioned species [18]. Also the area serves as a stop-over site for a large number of migratory waterfowls and raptor bird species [14]. Seasonally-looded meadows and small ponds are very important habitats for many waterfowls including White-storks. Available food resources and suitable climatic conditions are among the main factors affecting the presence of any bird species in an area. Tigris River and together with other components including food resources presumably affected on the wintering of mentioned species in the area. Despite of it's difficulties and risks, bird migration is an activity that is carried out due to it allows them to avoid harsh winter conditions and access abundant food resources. It has been evaluated that the start of wintering of White-storks may be related to many reasons such as food availability, climate change, global warming, etc.

As a result, White-storks have been started to wintering in the Bismil Plain IBA's where is located between Diyarbakır and Batman provinces. Presumably the size of population will increase in the future. The existence of suitable habitats together with food possibilities such as insects, frogs, snakes, small mammals, etc. [1] supports population increase in the area during all year round. These regular wintering records are first for Diyarbakır province and our information on the wintering of species for South-eastern Anatolia is unclear due to there is no any field work covering all of the region for the wintering periods. Monitoring of the wintering population in the region is recommended which may allow us to evaluate changes in size of population and range expansion of species in the region together with a comprehensive field study for determination of wintering population size in this part of Türkiye.

4. Discussion

The White-stork is revealed as a common summer migrant in Türkiye [11,12] with the exception some wintering records during last years [11,12,19,20]. It was considered that the number of wintering individuals, which was limited to a few individuals in the past [14], has increased in recent years. The exact reason of the increase in wintering population size of the species in Türkiye is not known fully. However, there are some studies on how temperature changes due to climate change affect biodiversity, including birds, and in this context, cause changes on distribution ranges, phenologies and structure of communities of many species in some countries [21,22]. And also, there are many studies showing that the transformation of many natural ecosystems by humans has led to habitat loss and degradation, that this situation has worsened with global climate change and that many species are affected by this, recently [23].

In recent years, a small portion of breeding populations of White-storks from western Europe started to wintering in the continent, also elsewhere in locations close to their breeding areas [24]. It was experienced that environmental factors affect the distribution and population dynamics of many waterbirds including White-storks together with available food resources and climatic conditions, in different parts of the world [25].

Despite off without more details, the occurrence of White-storks has been reported from 62 different locations in Türkiye during the winter seasons, by a recent study [19]. Also, by predicting the future situation of the species depending on climate and environmental variables, it has been stated that more suitable habitats will be found for this species in Turkey in the future [19]. Also, during last decades regular wintering areas reported from different part of country such as East Anatolia (Iğdır Plain) [20].

Although the species is still revealed as a widespread summer visitor to much of Europe [5], in generally, including Türkiye, it could be stated that there may be an increase in wintering areas by increase in resident populations. It is predicted that wintering records probably will increase in near future, especially in regions where the climate will be suitable together with available food opportunities during the winter seasons.

The Bismil Plain is one of the important areas for many bird species both as flyway and breeding area in this part of country [14]. Having a wide food diversity, the White-stork eats a wide variety of animal prey, including mainly large insects, fish, amphibians, reptiles and small mammals [1]. Species mainly prefers suitable areas where near the settlements, open farmlands, riverine habitats, marshes and wetlands. Presumably, the availability of suitable habitat's together with food possibilities may have been supports the population increase in the area during all year round. However, many factors such as the constant change of natural processes, global warming, etc. can cause the distribution ranges of species to change over time. Therefore, the continuation of the field works in the region has a great importance. Despite of limited data, it has been reported that the survival rate of White-storks wintering in Europe is higher than in individuals that migrating to Africa for wintering [26]. Therefore, this staying phenomena may cause shorter distance migrations in the future in many Palearctic countries including Türkiye.

Consequently, there are still significant gaps in our knowledge to understanding of how climate change will effects many species including birds. It could be suggested that further research needed for to clarify the impacts of climate change on white-stork distribution behaviour and ranges, particularly on wintering ranges of species. The other hand, this study showed that White-storks have found the favourable conditions for wintering in this part of Türkiye and have now started to wintering. Monitoring of the wintering population in the region will help to understand changes in size of wintering population in this part of country.

Ethical Statement

Due to species only observed ethics committee permission is not required.

Compliance with the Research and Publication Ethics

This study was carried out in accordance with the research rules and publication ethics.

Conflict of Interest

The author declares no conflict of interest.

Author Contribution

R.K. conducted the fieldworks and collected all data and written the manuscript.

References

[1] Cramp, S., ' *'The Complete Birds of the Western Palearctic''*, on CD-ROM.- Oxford University Press, Oxford, 1998.

[2] Gill, F., Donsker, D., Rasmussen, P., (Eds). *IOC World Bird List* (v 13.1), 2023. Doi 10.14344/IOC.ML.13.1.

[3] BirdLife, Species factsheet: White Stork *Ciconia ciconia*. Downloaded from https://datazone.birdlife.org/species/factsheet/white-stork-ciconia-ciconia on 11/07/2024, 2024a.

[4] Tucker, G.M., Heath, M.F., *Birds in Europe: their conservation status.* BirdLife International (BirdLife Conservation Series no: 3), Cambridge, UK, 1994.

[5]   BirdLife, *Birds in the European Union: a status assessment:* BirdLife International, Wageningen, The Netherlands, 2004.

[6]   Parr, S.P., Collin, P., Silk, S., Wilbraham, J., Williams, N.P., Yarar, M., ''A baseline survey of white Storks *Ciconia ciconia* in central Turkey'', *Sandgrouse,* 18(2), 46-51, 1996.

[7]   BirdLife, *Ciconia ciconia.* The IUCN Red List of Threatened Species 2016: e.T22697691A86248677. http://dx.doi.org/10.2305/IUCN.UK.2016-3.RLTS.T22697691A86248677.en, 2016.

[8]   IUCN, Red List of Threatened Species. <www.iucnredlist.org>. Downloaded on 20 Sep2024., 2024.

[9]   Itonaga, N., Köppen, U., Plath, M., Wallschläger, D., ''Breeding dispersal directions in the white stork (*Ciconia ciconia*) are affected by spring migration routes'', *Journal of ethology*, *28*, 393-397, 2010. Doi: 10.1007/s10164-010-0204-6

[10] Kaatz, M., Kaatz, M., Meinzenbach, A., Springer, S., Zieger, M., ''From "arrow storks" to search engine data: Google Trends reveals seasonality in search interest for migratory white storks (*Ciconia ciconia*) in Germany'', *Zoologischer Anzeiger*, *307*, 83-88, 2023. Doi: 10.1016/j.jcz.2023.09.005

[11] Kasparek, M., Bilgin, C.C. *Kuşlar (Aves).* In: *Türkiye Omurgalılar Tür Listesi [List of Turkish Vertebrates] (*Ed*.* Kence, A. and Bilgin, C.C.), TÜBİTAK, Ankara, p. 27-87, 1996.

[12] Kirwan, G.M., Boyla, K., Castell, P., Demirci, B., Özen, M., Welch, H., Marlow, T., *The Birds of Turkey,* Christopher Helm, London, 2008.

[13] Welch, H.J., *GAP Biodiversity Research Project 2001-2003 / Final Report.* DHKD (Doğal Hayatı Koruma Derneği - Turkish Society for the Conservation of Nature). İstanbul, Türkiye, 2004.

[14] Karakaş, R. ''Bird diversity in Bismil Plain IBA's with new records for South-eastern Anatolia, Turkey'', *European Journal of Wildlife Research,* 56, 471–480, 2010. Doi: 10.1007/s10344-009-0336-6.

[15] Kılıç, D.T., Eken, G., *Türkiye'nin Önemli Kuş Alanları – 2004 Güncellemesi [Turkey's Important Bird Areas – 2004 Update].* Doğa Derneği, Ankara, 2004.

[16] Eken, G., Bozdoğan, M., İsfendiyaroğlu, S., Kılıç, D.T., Lise, Y., (Eds) *Türkiye'nin Önemli Doğa Alanları* [*Turkey's Key Biodiversity Areas*]. Doğa Derneği, Ankara, 2006.

[17] Mullarney, K., Svensson, L., Grant, P.J., Zetterström, D., *Collins Bird Guide.* HarperCollins, London, UK, 1999.

[18] BirdLife, *Important Bird Area factsheet: Bismil Plain.* Downloaded from https://datazone.birdlife.org/site/factsheet/bismil-plain-iba-türkiye on 11/07/2024. 2024b.

[19] Süel, H., ''Predicting distribution of white stork (*Ciconia ciconia* Linnaeus, 1758) under climate change in Turkey. *Turkish Journal of Forestry*, 20(3), 243-249, 2019. Doi: 10.18182/tjf.565284

[20] Özkoç, Ö.Ü. ''Breeding and Migratory Bird Diversity in Iğdır Province (Eastern Anatolia). *Commagene Journal of Biology*, *6*(2), 207-217, 2022, Doi: 10.31594/commagene.1190796

[21] Kappelle, M., Van Vuuren, M.M.I., Baas, P., ''Effects of climate change on biodiversity: a review and identification of key research issues''. *Biodiversity Conservation,* 8(10), 1383–1397, 1999. Doi: 10.1023/A:1008934324223.

[22] Verniest, F., Le Viol, I., Julliard, R., Dami, L., Guelmami, A., Suet, M., Abdou, W., Azafzaf, H., Bendjedda, N., Bino, T., Borg, J.J., Bozic, L., Dakki, M., El Hamoumi, R., Encarnaçao, V., Erciyas-Yavuz, K., Etayeb, K., Georgiev, V., Hamada, A., Hatzofe, O., Galewski, T., ''Anticipating the effects of climate warming and natural habitat conversion on waterbird communities to address protection gaps''. *Biological Conservation*, *279*, 109939, 2023. Doi: 10.1016/j.biocon.2023.109939

[23] Pavon-Jordan, D., Abdou, W., Azafzaf, H., Balaž, M., Bino, T., Borg, J. J., Božic, L., Butchart, S.H.M., Clausen, P., Sniauksta, L., Dakki, M., Devos, K., Domsa, C., Encarnaçao, V., Etayeb, K., Faragó, S., Fox, A.D., Frost, T., Gaudard, C., Georgiev, V., Goratze, I., Hornman, M., Keller, V., Kostiushyn, V., Langendoen, T., Lawicki, L., Ieronymidou, C., Lewis, L.J., Lorentsen, S.H., Luigujoe, L., Meissner, W., Mikuska, T., Molina, B., Musil, P., Musilova, Z., Nagy, S., Natykanets, V., Nilsson, L., Paquet, J.Y., Portolou, D., Ridzon, J., Santangeli, A., Sayoud, S., Šćiban, M., Stipniece, A., Teufelbauer, N., Topić, G., Uzunova, D., Vizi, A., Wahl, J., Yavuz, K.E., Zenatello, M., Lehikoinen, A., ''Positive impacts of important bird and biodiversity areas on wintering waterbirds under changing temperatures throughout Europe and North Africa''. *Biological Conservation*, *246*, 108549, 2020. Doi: 10.1016/j.biocon.2020.

[24] Archaux, F., Henry, P.Y., Balança, G. ''High turnover and moderate fidelity of White Storks *Ciconia ciconia* at a European wintering site''. *Ibis*, *150*(2), 421-424, 2008, Doi: 10.1111/j.1474-919X.2007.00798.x

[25] Mammeria, A.B., Triplet, P., Bitam, I., ''The white stork *Ciconia ciconia* in the northeast of Algeria, and its relation with climatic change between 1996 and 2014. *Estuarine, Coastal and Shelf Science*, *216*, 165-170, 2019. Doi: 10.1016/j.ecss.2018.01.001

[26] Rotics, S., Turjeman, S., Kaatz, M., Resheff, Y. S., Zurell, D., Sapir, N., Eggers, U., Fiedler, W., Flack, A., Jeltsch, F., Wikelski, M., Nathan, R., ''Wintering in Europe instead of Africa enhances juvenile survival in a long-distance migrant''. *Animal Behaviour*, *126*, 79-88, 2017. Doi: 10.1016/j.anbehav.2017.01.016.

Middle East Journal of Science

Research Article

NORTHERN BALD IBIS POPULATION DYNAMICS-BİRECİK-TÜRKİYE (2012-2022)

Ahmet KILIÇ[1]   *& Ersin UYSAL[2]*

[1]M.S.Ö. Air & Space Museum, Yeşilköy Sivrihisar, TR-26600 Eskişehir, Türkiye
[2]Department of Computer Technologies, Vocational School of Technical Sciences, Dicle University, TR-21280 Diyarbakır, Türkiye
Corresponding author: ahmetkilic20011961@gmail.com

Abstract *This research was carried out to determine the reproduction, death, and loss numbers of Northern Bald Ibises living in Birecik (Şanlıurfa). The research was continued for 11 years. Northern Bald Ibises are an endangered species. Northern Bald Ibises breed freely in nature in Birecik. They are placed in cages at the end of June. They live in a cage for eight months. The reproductive ability of the population is high (2012-2022: 782 offspring). But the total number of the population is increasing very slowly. The number of offspring deaths is high (2012-2022: 267 dead offspring). Mortality occurs in the first two weeks of the offspring. Adult deaths and losses occur for different reasons (2012-2022: 246 adult individuals). Measures to be taken can prevent offspring deaths. There is a need for regulation in feeding and cage conditions. A second Northern Bald Ibis breeding station should be established. In order to keep the population alive, the aim should be to increase the number of Northern Bald Ibises. Allowing Northern Bald Ibises to migrate causes individuals to perish. Scientific methods need to be applied to accustom people to migration. Expert personnel (biologists or veterinarian) should be assigned to the station throughout the year.*

Keywords: *Northern Bald Ibis, Geronticus eremita, number of offspring, offspring deaths, adult losses*

1. Introduction

Northern Bald Ibises are an endangered species. There is one large populations in Morocco and a semi-wild population in Türkiye. A captive population is maintained in Germany, Austria and Italy. There are 1995 Northern Bald Ibises in 92 zoos in the United States, Japan and Europe [1]. Northern Bald Ibises in zoos are of Moroccan origin [2].

Northern Bald Ibis colonies were detected in Türkiye, Syria and Iraq 200 years ago [3]. The first written source reporting Northern Bald Ibises in Birecik (Şanlıurfa) belongs to Ainsworth (1842) [3]. The drug DDT used in agriculture caused the mass death of Northern Bald Ibises [4, 5, 6]. Habitat change can lead to a decrease in the feeding and breeding areas of particularly sensitive species, which may result in a decline or even extinction of their populations [7]. The last Northern Bald Ibis living in nature in Birecik was seen in 1989 [8]. In 1990, the Northern Bald Ibis became extinct in nature in Birecik [9]. At the Birecik Northern Bald Ibis Breeding Station, 156 chicks were added to the population between 2000 and 2009 [10]. In Türkiye, 18 Northern Bald Ibises were placed in three zoos in 2016 [2]. Based on satellite transmitter records one of the tracked Northern Bald Ibis traveled 3300 km from Birecik to Ethiopia [11]. It has been determined that Northern Bald Ibises in Morocco have problems such as human disturbance and distance to food areas [12].

After many years, a wild population (seven individuals) was detected in Palmyra (Syria) in the Middle East [13]. Between 2002 and 2007, Northern Bald Ibises raised 24 chicks in Syria [14].

A correct correlation was determined between the number of offspring and the number of breeding pairs in the breeding area of Tamri in Morocco. In the other breeding area, Souss-Massa National Park, no correlation was observed between the number of offspring and the number of breeding pairs [15]. Between 1 and 22 individuals were identified migrating between Morocco and Spain between 2010 and 2017 [16]. There are 708 Northern Bald Ibises living in Morocco [1].

The increase in the number of breeding pairs in Morocco from 59 to 147, the reappearance of Northern Bald Ibises in Syria, the survival of the semi-wild population in Turkey, and the efforts to settle Northern Bald Ibises in Southern Europe are considered successful [17]. Due to these studies, the IUCN red list status of Northern Bald Ibises has been reduced from "critically endangered" to "endangered" [18,19].

Birecik-Şanlıurfa, on the banks of the Euphrates River, is located in the continental climate zone - winters are mild and summers are hot.

This research aims to contribute to preventing the extinction of the Northern Bald Ibis and increasing its number.

2. Material and Methods

This research was carried out on free-breeding Northern Bbald Ibises in Birecik (Şanlıurfa). Observations lasted 11 (2012-2022) years. Research started in mid-February every year and continued until the end of the breeding season (June). Observations were made 1-2 days each week. Observations lasted 2 - 10 hours during the day. Observations were made outside the breeding station, 50-150 m away from the nests. Thus, Northern Bald Ibises were prevented from being affected by the research. Binoculars, telescopes, cameras, and video cameras were used to see the eggs and hatchlings in the nest.

A chi-square statistical test was used in this study. Statistical evaluations were considered significant for $p < 0,05$.

3. Results and Discussion

Northern Bald Ibises are released from the cage in mid-February. At the end of the breeding season (June), they are put back into cages. They breed in wooden nests placed on the rocks next to the cage. In 2018, 12 more wooden nests were added to the Birecik breeding station, in addition to the existing nests in previous years. The number of artificial (wooden) nests was 48. In 2020, 20 more artificial nests were added. In 2022, the number of wooden nests was 68. Besides these, there are five more nests carved into the rock (by the officials). Northern Bald Ibises also nest in suitable places on rocks every year (natural nest). The number of these natural nests varied between 10-15 each year. In addition, the roofs of wooden nests were also used as nesting places. Some of the different nest types remained empty and were not preferred as incubation sites (Table 1).

Table 1. Population Dynamics of Northern Bald Ibis (n)

	Years										
	2012	**2013**	**2014**	**2015**	**2016**	**2017**	**2018**	**2019**	**2020**	**2021**	**2022**
A-Released from the Cage (February)	126	152	163	185	205	209	241	261	241	278	301
B-Number of Offspring (April)	45	60	66	74	59	58	71	116	75	95	63
C-Loss of offspring in the Nest	3	21	20	17	21	3	0	71	0	1	7
D-Number of Offspring (May)	42	39	46	57	38	55	71	45	75	94	56
E-Number of Young in the Cage	33	34	42	52	38	47	65	25	68	72	39
F-Number of Adults Taken into the Cage (June)	126	131	147	157	179	198	208	218	217	253	282
G-Total Number in the Cage (June) (E+F)	159 (33+126)	165 (34+131)	189 (42+147)	209 (52+157)	217 (38+179)	245 (47+198)	273 (65+208)	243 (25+218)	285 (68+217)	325 (72+253)	321 (39+282)
H-Annual Number Increase (G- A)	33 (159-126) (5 that cannot be taken into the cage)	13 (165-152) (Released with 6 NBI satellite + radio receivers)	26 (189-163)	24 (209-185)	12 (217-205)	36 (245-209)	32 (273-241)	-18 (243-261)	44 (285 - 241)	47 (325-278) (Left to Migration 15 NBI)	20 (321-301) (Left to Migration 30 NBI)
I-Dying, Lost Young (B-E)	12 (45-33)	26 (60-34)	24 (66-42)	22 (74-52)	21 (59-38)	11 (58-47)	6 (71-65)	91 (116-25)	7 (75 - 68)	23 (95-72)	24 (63-39)
J-Dead, Disappeared Adult (A-F)	0 (126-126)	21 (152-131)	16 (163-147)	28 (185-157)	26 (205-179)	11 (209-198)	33 (241-208)	43 (261-218)	24 (241 - 217)	25 (278-253)	19 (301-282)
K-Deaths Disappeared Total (I + J)	12 (12+0)	47 (26+21)	40 (24+16)	50 (22+28)	47 (21+26)	22 (11+11)	39 (6+33)	134 (91+43)	31 (7+24)	48 (23+25)	43 (24+19)
L-Number of Incubations	23	34	35	46	41	49	64	73	67	85	70
M-Per Incubation Number of Offspring (B÷L)	1,95 (45÷23)	1,76 (60÷34)	1,88 (66÷35)	1,60 (74 ÷ 46)	1,43 (59 ÷ 41)	1,18 (58 ÷ 49)	1,10 (71 ÷ 64)	1,58 (116÷73)	1,11 (75 ÷ 67)	1,11 (95 ÷ 85)	0,90 (63 ÷ 70)
N-Per Incubation Number of Flying Chicken (E÷L)	1.43 (33÷23)	1.00 (34÷34)	1.20 (42÷35)	1.13 (52÷46)	0.92 (38÷41)	0.95 (47÷49)	1.01 (65÷64)	0.34 (25÷73)	1.01 (68÷67)	0.84 (72÷85)	0.55 (39÷70)

The number of offspring varies in April, May and June (Table 2). The reason for this change is offspring mortality. There is a difference in the comparison of the number of offspring in April, May and June in 2013, 2014, 2016, 2017, 2019 (Table 2). It was statistically determined that there was no difference between the number of offspring in April, May and June in 2012, 2015, 2018, 2020, 2021 and 2022 (Table 2).

Table 2. Calculations for the Number of Offspring (Quarterly changes over the years)

Years	Months	n	Chi-square	p
2012	April	45		
	May	42	1,950	0,377
	June	33		
2013	April	60		
	May	39	8,586	**0,014**
	June	34		
2014	April	66		
	May	46	6,442	**0,040**
	June	42		
2015	April	74		
	May	57	4,361	0,113
	June	52		
2016	April	59		
	May	38	6,533	**0,038**
	June	38		
2017	April	58		
	May	55	1,213	**0,545**
	June	47		
2018	April	71		
	May	71	0,348	0,840
	June	65		
2019	April	116		
	May	45	73,774	**0,000**
	June	25		
2020	April	75		
	May	75	0,450	0,799
	June	68		
2021	April	95		
	May	94	3,885	0,143
	June	72		
2022	April	63		
	May	56	5,785	0,055
	June	39		

The change in the number of offspring by month between 2012 and 2022 is shown in Figure 1. The number of offspring increased to a maximum in 2019. However, the highest loss of offspring occurred in 2019. Deaths occur due to competition between offsprings. That's why the number of offsprings in June decreases. (Figure 1).
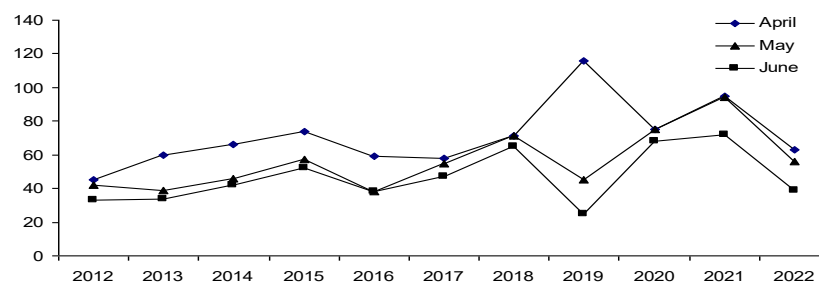
Figure 1. Distribution of the Number of Offspring by Years.

The number of offspring varies in April, May, and June (Figure 1). This difference continued in a similar way every year. The number of offspring is highest in April. Competition is very intense between the 2-3 siblings in the nest. Food is mostly taken by the eldest sibling. In all nests, the youngest chick who hatches the latest has a low chance of survival. The youngest chick that receives little food becomes weak and shows developmental delays. Also, the older sibling/s constantly pecks the younger sibling. The youngest offspring is kept under pressure before food intake. Offspring deaths occur in the nest. The parent does not prevent fights between offspring.

There is a slight increase in the total number of offspring between 2012 and 2022 (Figure 1). When the total number of offspring of the eleven-year (2012-2022) months of April, May and June is examined, it is seen that there is a statistically significant difference (Table 3).

Table 3. Calculations for the Number of Offspring (11-year changes by months).

Months	Years	n	Chi-square	p
April	2012	45		
	2013	60		
	2014	66		
	2015	74		
	2016	59		
	2017	58	53,803	**0,000**
	2018	71		
	2019	116		
	2020	75		
	2021	95		
	2022	63		
	∑	782		
May	2012	42		
	2013	39		
	2014	46		
	2015	57		
	2016	38		
	2017	55	54,495	**0,000**
	2018	71		
	2019	45		
	2020	75		
	2021	94		
	2022	56		
	∑	618		
June	2012	33		
	2013	34		
	2014	42		
	2015	52		
	2016	38		
	2017	47	51,981	**0,000**
	2018	65		
	2019	25		
	2020	68		
	2021	72		
	2022	39		
	∑	515		

Figure 2 shows the comparative histogram of April, May and June. Since offspring deaths are less in April, the number of offsprings is high. Due to chick mortality, the number of offsprings is low in June (Figure 2).
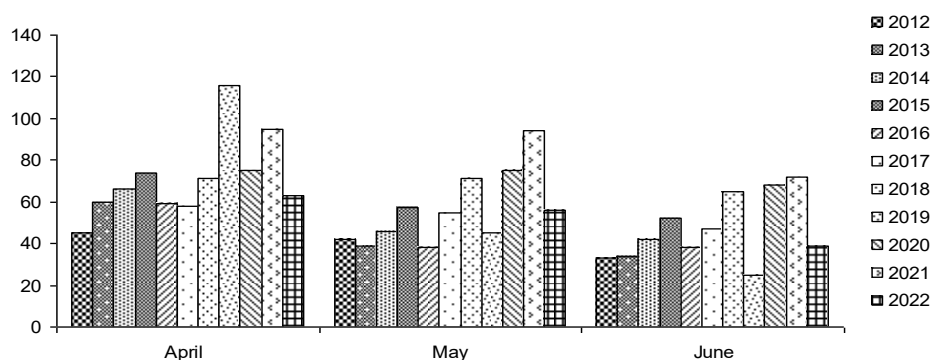
Figure 2. Distribution of the number of offspring by years.

A decrease was detected when the number of adults released from cages at the beginning of the breeding season (February) was compared with the number of adults taken into the cage at the end of the breeding season. However, no statistical difference was observed (Table 4). In 2019, the total number of individuals decreased due to juvenile deaths and adult losses and a difference was detected (Table 4).

Table 4. Comparison of the Number Released from the Cage (February) and the Number of Adults Caged (June) by Years.

Years	Parameters	n	Chi-square	p
2012	Released from the Cage	126	0,00	1,000
	Number of Adults Taken into the Cage	126		
2013	Released from the Cage	152	1,558	0,212
	Number of Adults Taken into the Cage	131		
2014	Released from the Cage	163	0,826	0,363
	Number of Adults Taken into the Cage	147		
2015	Released from the Cage	185	2,292	0,130
	Number of Adults Taken into the Cage	157		
2016	Released from the Cage	205	1,760	0,185
	Number of Adults Taken into the Cage	179		
2017	Released from the Cage	209	0,297	0,586
	Number of Adults Taken into the Cage	198		
2018	Released from the Cage	241	2,425	0,119
	Number of Adults Taken into the Cage	208		
2019	Released from the Cage	261	3,860	**0,049**
	Number of Adults Taken into the Cage	218		
2020	Released from the Cage	241	1,258	0,262
	Number of Adults Taken into the Cage	217		
2021	Released from the Cage	278	1,177	0,278
	Number of Adults Taken into the Cage	253		
2022	Released from the Cage	301	0,619	0,431
	Number of Adults Taken into the Cage	282		

The number of adult Northern Bald Ibises removed from cages (in February) is higher than the number of adults taken into cages (in June) (Figure 3, Tables 4, 5). The low number of adults taken into cages was not statistically significant (Table 5). Every year, on average (246 (n) ÷ 11 (year) =) 22.36 adult Northern Bald Ibises die and/or disappear.

Table 5. Comparison of the Number of Adults Released from the Cage and Taken into the Cage.

	Years										
	2012	**2013**	**2014**	**2015**	**2016**	**2017**	**2018**	**2019**	**2020**	**2021**	**2022**
Released from the Cage (February)	126	152	163	185	205	209	241	261	241	278	301
Number of Adults Taken into the Cage	126	131	147	157	179	198	208	218	217	253	282
Chi-Square=2,156; p=0,976											
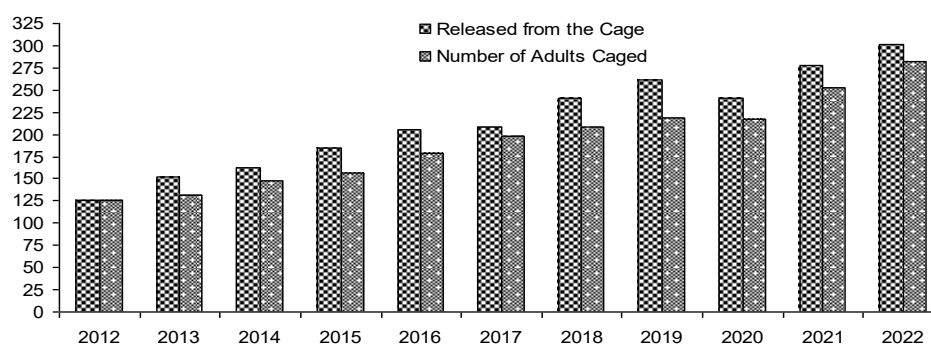
Figure 3. Comparison of the Number of Adults Released from the Cage and Caged Adults.

Adults do not die only in nature. Deaths were also detected in cages (Table 1). As can be seen in the data in Table 1, the number of Northern Bald Ibises spending the winter in cages is decreasing. Between 2012 and 2022, a total of 55 Northern Bald Ibises decreased in cages.

The number of adult Northern Bald Ibises released into the wild at the beginning of the breeding season and the total number of adults and young birds taken into cages at the end of the breeding season are compared statistically in Table 6. According to Table 6, it is revealed that there is no difference in the total number of Northern Bald Ibises before and after breeding.

Table 6. Comparison of the Number Released from Cages (February) and the Number Caged (June) by Years

| Years	Parameters	n	Chi-square	p
2012	Released from the Cage Number of Adults Taken into the Cage	126 159	3,821	0,051
2013	Released from the Cage Number of Adults Taken into the Cage	152 165	0,533	0,465
2014	Released from the Cage Number of Adults Taken into the Cage	163 189	1,920	0,166
2015	Released from the Cage Number of Adults Taken into the Cage	185 209	1,462	0,227
2016	Released from the Cage Number of Adults Taken into the Cage	205 217	0,341	0,559
2017	Released from the Cage Number of Adults Taken into the Cage	209 245	2,855	0,091
2018	Released from the Cage Number of Adults Taken into the Cage	241 273	1,992	0,158
2019	Released from the Cage Number of Adults Taken into the Cage	261 243	0,643	0,423
2020	Released from the Cage Number of Adults Taken into the Cage	241 285	3,681	0,055
2021	Released from the Cage Number of Adults Taken into the Cage	278 325	3,663	0,056
2022	Released from the Cage Number of Adults Taken into the Cage	301 321	0,643	0,423

The total number of Northern Bald Ibises released from the cage and taken into the cage at the end of the breeding period between 2012 and 2022 was evaluated statistically (Chi-square = 7.083; p = 0.718) (Table 7). No statistical increase can be expressed for 11 years.

Table 7. Comparison of the Number Released from the Cage and the Number Caged by Years (n)

	2012	2013	2014	2015	2016	2017	2018	2019	2020	2021	2022
Released from the Cage (February)	126	152	163	185	205	209	241	261	241	278	301
Number of Adults Taken into the Cage (June)	159	165	189	209	217	245	273	243	285	325	321
Chi-Square = 7,083 ; p = 0,718											

Every year, hatchlings join the population. Out of the three eggs in the nest, all three hatchlings can hatch. In some nests, two or one offspring can be seen. Offspring deaths occur in the first weeks. At the end of the breeding season, young birds and adults are returned to the cage. There was a statistical difference in the number of hatchlings hatched in April from the number of hatchlings that died or disappeared that year (Table 8).

Table 8. Comparison of Number of Offsprings (April) and Number of Dead-Missing Offsprings by Years

Years	Parameters	n	Chi-square	p
2012	Number of Offspring (April)	45	19,105	**0,000**
	Dying, Lost Young	12		
2013	Number of Offspring (April)	60	13,442	**0,000**
	Dying, Lost Young	26		
2014	Number of Offspring (April)	66	19,600	**0,000**
	Dying, Lost Young	24		
2015	Number of Offspring (April)	74	28,167	**0,000**
	Dying, Lost Young	22		
2016	Number of Offspring (April)	59	18,050	**0,000**
	Dying, Lost Young	21		
2017	Number of Offspring (April)	58	32,014	**0,000**
	Dying, Lost Young	11		
2018	Number of Offspring (April)	71	54,870	**0,000**
	Dying, Lost Young	6		
2019	Number of Offspring (April)	116	3,019	**0,082**
	Dying, Lost Young	91		
2020	Number of Offspring (April)	75	56,390	**0,000**
	Dying, Lost Young	7		
2021	Number of Offspring (April)	95	43,932	**0,000**
	Dying, Lost Young	23		
2022	Number of Offspring (April)	63	17,483	**0,000**
	Dying, Lost Young	24		

In Table 9, the number of dead-lost offspring of all observation years (2012-2022) and the total number of offspring in April are compared statistically, and it is seen that the difference has changed significantly. The number of offsprings in April was different from the number of offsprings that died (Table 9 and Figure 4).

Table 9. Comparison of Total Number of Offsprings (April) and Number of Dead-Missing Offsprings by Years.

	2012	2013	2014	2015	2016	2017	2018	2019	2020	2021	2022
Number of Offsprings (April)	45	60	66	74	59	58	71	116	75	95	63
Dying, Lost Offsprings	12	26	24	22	21	11	6	91	7	23	24
Chi-Square=70,143 ; p=0,000											
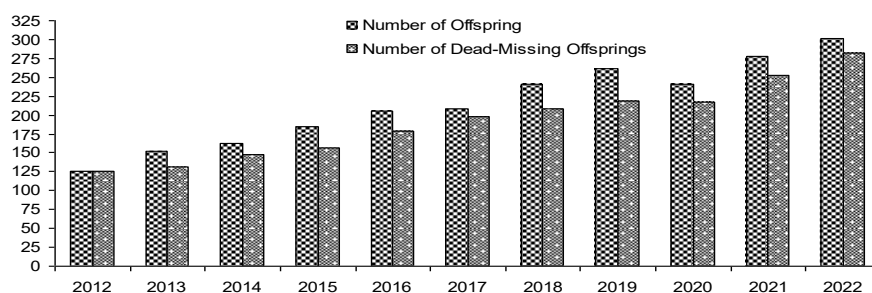
Figure 4. Comparison of Number of Offsprings (April) and Number of Dead-Missing Offsprings

The number of adult individuals released from the cage into the wild and the total annual number of offspring + adults that died or disappeared until the end of the breeding season were compared statistically (Table 10). It is calculated separately for each year in Table 10. It was revealed that the number of adults released from the cage in all years of observation was different from the number of dead or missing (adults + young birds) (Table 10).

Table 10. Number of Adults Released from the Cage by Years Comparisons of Total Number of Death- Lost Hatchlings + Adults

Years	Parameters	n	Chi-square	p
2012	Released from the Cage (February)	126	94,174	**0,000**
	Deaths Disappeared Total	12		
2013	Released from the Cage (February)	152	55,402	**0,000**
	Deaths Disappeared Total	47		
2014	Released from the Cage (February)	163	74,527	**0,000**
	Deaths Disappeared Total	40		
2015	Released from the Cage (February)	185	77,553	**0,000**
	Deaths Disappeared Total	50		
2016	Released from the Cage (February)	205	99,063	**0,000**
	Deaths Disappeared Total	47		
2017	Released from the Cage (February)	209	151,381	**0,000**
	Deaths Disappeared Total	22		
2018	Released from the Cage (February)	241	145,729	**0,000**
	Deaths Disappeared Total	39		
2019	Released from the Cage (February)	261	40,833	**0,000**
	Deaths Disappeared Total	134		
2020	Released from the Cage (February)	241	162,132	**0,000**
	Deaths Disappeared Total	31		
2021	Released from the Cage (February)	278	162,270	**0,000**
	Deaths Disappeared Total	48		
2022	Released from the Cage (February)	301	193,500	**0,000**
	Deaths Disappeared Total	43		

According to the eleven-year evaluation, the number of individuals released from the cage was found to be statistically different from the total number of dead and missing individuals (Table 11).

Table 11. Comparison of the Number of Adults Released from the Cage and the Total Number of Dead-Missing Hatchlings + Adults by Years.

	2012	2013	2014	2015	2016	2017	2018	2019	2020	2021	2022
Released from the Cage (February)	126	152	163	185	205	209	241	261	241	278	301
Deaths-Missings Total (June)	12	47	40	50	47	22	39	134	31	48	43
Chi-Square=114,970 ; **p=0,000**											

A comparative histogram of the annual number of deaths and losses and the number of Northern Bald Ibises released from the cage between 2012 and 2022 is shown in Figure 5. According to Figure 5, the total number of individuals released from the cage appears to have increased regularly. According to Figure 5, the annual number of dead or missing individuals continues without any major change.
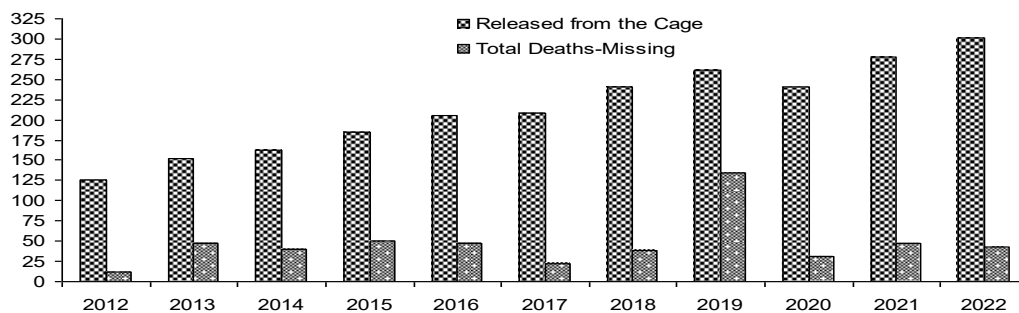
Figure 5. Histogram comparing the number of individuals released from the cage and the total number of dead-missing individuals

A different number of broods (n = 23–85) (Table 1) occurred each year. The number of incubated chicks (April) has decreased over the years (Figure 6).
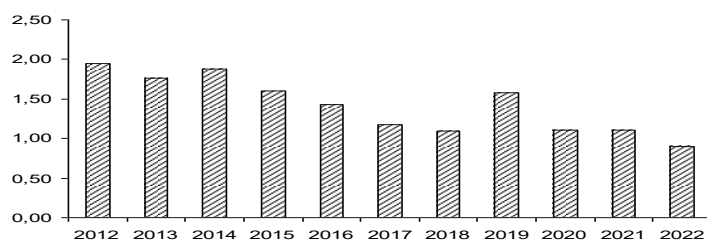
Figure 6. Number of Offspring per Brood (in April)

The number of hatchlings per brood (between 2012-2022) is shown in Figure 7. As seen in Figure 7, the number of flying chicks is decreasing on average.
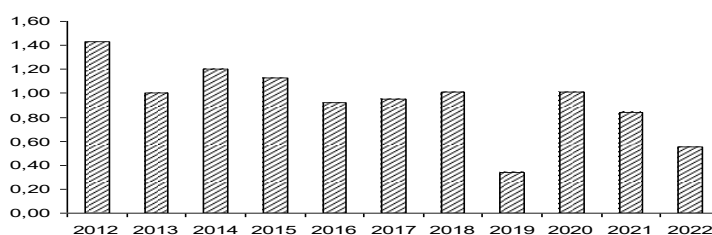
Figure 7. Number of Hatchlings flying per Brood (in May)

Although the breeding potential is high, deaths and losses are high in juvenile and adult Northern Bald Ibises. Offspring deaths are more common in the first weeks. During this period, offspring loss varies between 8-78%. Adult deaths and losses were determined as 0-16% of the population. Total losses and deaths in the population have varied between 7-35% over the years (2012-2022).

The wooden nests mounted on the rocks at the Northern Bald Ibis breeding station are covered with roof insulation material. This situation prevents the ventilation of the nests. During the extremely hot breeding season, the temperature in wooden nests increases even more. The slope of the wooden nest roofs has been steepened. It has become difficult to stand on roofs due to the extreme slope. Northern Bald Ibises, which nested on wooden nest roofs in previous years, have lost this opportunity. In wooden nests, Northern Bald Ibises cannot see each other. However, Northern Bald Ibises incubate close to each other in nature. Successful incubation and baby care are achieved by influencing each

other. Their nesting places in separate boxes do not allow them to see each other. Therefore, they are prevented from influencing each other positively.

In the joint project of Germany-Austria-Italy, 84 Northern Bald Iibises lost their lives due to different reasons (hunting, electric cable shock, etc.) between 2014 and 2016. In 2017, electric shocks accounted for 23% of the causes of Northern Bald Ibis deaths, and disappearances accounted for 51% [17]. The number of Northern Bald Ibises reached 102 in Rosegg, Kuchl (Austria) and Burghausen, Überlingen (Germany) in 2018 [17]. In 2018, the number of offspring deaths was determined as 46 individuals. Predation and electrocution are the causes of losses. There are also losses of Northern Bald Ibises due to hunters [17].

In 1996, 38 individuals (of different ages) died in Morocco. The cause of death could not be determined [20].

Quevedo Muñoz et al [21] reported that 24 Northern Bald Ibises died and 8 disappeared due to hunters, power lines and other reasons in 2004-2005 in the Proyecto Eremita-Almeria (Spain) project, it was determined that six individuals died due to electric shock in 2006, 39.4% of 190 individuals (75 young birds and adults) died between 2004 and 2009. It was determined that those who died were mostly offsprings [22]. It is known that deaths by electric shock also occur from Northern Bald Ibises in Birecik [23].

The disappearance of Northern Bald Ibises in Birecik was also reported by different researchers in previous years. It was determined that 67 individuals disappeared in Birecik between 1981 and 1988 [8]. It was recorded that many individuals were lost before the Northern Bald Ibises were taken into cages [24, 25]. Özbağdatlı [26] found that 32 northern bald ibises disappeared and 21 of them died between 2000 and 2006. Between 2000 and 2009, 25 chicks died and 53 individuals were found to have disappeared at the Birecik Northern Bald Ibis Breeding Station [10]. Pesticides and high voltage lines used in agricultural areas in Birecik have been identified as problems faced by Northern Bald Ibises [27].

These losses and deaths can be prevented [28, 29, 30]. During our observations (2012-2022), it was determined that deaths and losses occurred due to indifference [31, 32]. In 2019, the highest number of juvenile and adult losses occurred in Birecik. In 2019, 91 offsprings died or disappeared. Dead offsprings have been detected in the nests. In the same year, 43 adults were lost. Northern Bald Ibis Breeding Station officials declared that the pesticides used in the surrounding fields may be effective. In our research, the total loss of offspring in Birecik between 2012 and 2022 is 267. The average number of offspring deaths and losses each year was 24 (6-91). In addition, a total of 246 adult Northern Bald Ibises were lost annually between 2012 and 2022. An average of 22 (0-43) adult Northern Bald Ibises were lost each year.

It is stated that the Northern Bald Ibis colony in Syria may consist of Birecik Northern Bald Ibises [33]. The annual loss of adults in our research in Birecik supports this view. Detailed studies are needed on losses of adult Northern Bald Ibises. It is thought that some of the northern bald ibises may have settled in one of the Middle Eastern countries (Syria, Saudi Arabia, Israel or Jordan).

Özbağdatlı [26] reports that 1.4-1.9 offsprings per nest were raised in Birecik between 2000 and 2006. Yeniyurt et al [34] reported that the average productivity of northern bald ibises in Birecik from 2009 to 2015 was 1.12 offspring per nesting pair (0.96-1.19). When two studies [26, 34] are evaluated together, Northern Bald Ibises raise fewer offspring. The values we obtained as a result of our research are as follows: The number of offspring per incubation (in April) was calculated as 1.41 (1.95-0.90), and the number of offspring flying per incubation was calculated as 0.94 (1.43-0.34). These findings differ from Özbağdatlı [26] and Yeniyurt et al [34].

Serra and Peske [35] reported that free-living bald ibises in Palmyra (Syria) raised 20 chicks between 2002 and 2006. 1-3 offsprings per nest were raised here.

A total of 59-77 pairs bred in two different regions in Morocco between 1994 and 2002 [36]. In Parc National de Souss-Massa (PNSM) (Morocco), between 1995 and 1999, 289 hatchlings emerged from 354 eggs in 123 nests. The hatching percentage is 81.6. In Tamri, between 1995 and 1999, 179 hatchlings emerged from 216 eggs in 79 nests. The hatching percentage is 82.9 [37]. El Bekkay et al [38] reported the number of offspring (reproduction) in the nest in Morocco between 1994 and 2004 as 0.61-2.27 in Massa and 0.54-1.47 in Tamri. Between 1980 and 2007, 48-105 eggs were produced each year in Morocco. It has been determined that 0.39-1.80 offspring are raised per nest pair here [39]. Oubrou & El Bekkay [40] reported that 122 pairs of Northern Bald Ibises raised 152 offspring in two localities in Morocco (Souss-Massa National Park and Tamri), with 1.2 offspring per nest. An increase in the number of couples was observed in two separate colonies in Morocco between 2006 and 2018. The number of Northern Bald Ibises reached 147 pairs [15]. Two new breeding colonies have been identified on the Atlantic Ocean coast in Morocco. 11-15 individuals were detected in these two new colonies [41]. The results regarding the number of offspring reported from Morocco are higher than the values in Birecik.

Nests with and without access to water were compared in the Agadir (Morocco) region between 1998 and 2002. The number of offspring per nest has been reported as 1.16-2.41 (with water) and 1.00-2.27 (without water). It is reported that access to water resources positively affects reproduction [42]. Breeding values in Birecik are calculated to be lower than in the Agadir (Morocco) region. It was calculated that an average of 0.8-3.0 chicks were raised per nest in Northern Bald Ibises in Germany and Austria between 2011 and 2016 [43]. These values are higher than the breeding values in Morocco and Birecik.

Murray & Shaw-2006 [44] found that in White Bald Ibises, the success rate was 47.9% in incubation, 60.3% in raising offspring, and 28.9% in flight size.

The values given by Yeniyurt et al [34] in their study (Table 1) are clearly different from the values given in our study (Table 1). Böhm et al [1] The breeding values of Northern Bald Ibises in Birecik in 2012-2018 (Table 3) differ from our research.

The genetic structure of Northern Bald Ibises in European Zoos is different from the Eastern population [45]. That's why the Northern Bald Ibises in Birecik need to be protected.

Böhm [2] states that the Northern Bald Ibises detected in Saudi Arabia are not of Turkish origin. However, the wild Northern Bald Ibis colony in Palmyra (Syria) is located a few hundred kilometers south of Birecik [2]. Adult Northern Bald Ibises from Birecik (Türkiye) disappear every year (Table 1).

There is a possibility of new colonies appearing in Syria. Because there is a loss of Northern Bald Ibises in Birecik every year (Table 1). In the pictures in Serra [46] and [47], Northern Bald Ibises can be seen wearing colorful leg rings. These Northern Bald Ibises are thought to be the ones leaving Birecik (Türkiye).

Many Northern Bald Ibises are disappearing. It has not been determined whether these losses were due to death or migration. Different reasons can be considered for losses. Some Northern Bald Ibises may have headed south (towards Syria). It is highly likely that the natural colony identified in Syria [13, 14] originates from Turkey. No Northern Bald Ibis hunting has been detected in Birecik. Because Northern Bald Ibises are considered sacred in Birecik.

According to Tables 4 and 6, it is revealed that there is no statistically significant increase in numbers between the beginning and the end of the breeding season. Adult losses and offspring deaths are thought to be the determinants of this situation. When the data in Table 6 is examined, it is seen that there is no statistical increase in annual reproduction. According to Table 7, it is shown that there is no change in the total number before breeding and at the end of the breeding season (Chi-Square = 7.083; p = 0.718).

Between 2012 and 2022, there was a decrease of 55 individuals in cages. There is an average of (55÷11=5) 5 Northern Bald Ibis birds decreasing every year. Northern Bald Ibis breeding station officials will inform the scientific world about this issue.

The number of incubations increased steadily from 2012 to 2022 (Table 1). However, the number of offspring per brood tends to decrease regularly. The decrease in the number of hatchlings hatched during incubation may be due to different reasons. One of these is lack of food. Parental ability may be an important factor affecting offspring rearing. In addition, stress in the population due to inbreeding, hunting, biocides, and congeneric environment may be effective.

Dead chicks have been seen in Northern Bald Ibis nests. In our observations, it was determined that in some nests, the dead chick was tried to be swallowed by the parent.

4. Conclusion

Northern Bald Ibis rescue activity has been continuing for 45 years (1977-2022). The protected status of endangered Northern Bald Ibises is sensitive. It is essential to increase their numbers. Expert support is needed to keep the offspring alive during the breeding period. It has been determined that some adults died from electricity poles. Not enough information could be obtained about the deaths and losses of adults. There is also a need to re-evaluate nutrition and shelter conditions. Instead of chicken feed, a diet based on grasshoppers, insects and caterpillars should be preferred. A sandy and grassy ground should be prepared in the cage. The environment in which earthworms will survive should be arranged on the ground.

It is recommended to establish a second station for the survival and protection of Northern Bald Ibises [48, 49]. Since in-breeding involves risks, a second breeding station is deemed necessary due to the possibility of epidemics and different threats. It is recommended that the younger ones in the nest be left in nests that do not have chicks. The one that hatches late and is younger than its siblings can be kept alive.

It is reported by the Birecik Northern Bald Ibis Breeding Station officials that 75 Northern Bald Ibis chicks were sent to migration between 2021 and 2023 [50, 51]. Young individuals do not know migration routes. These young Northern Bald Ibises do not know where to eat or stay. Releasing young Northern Bald Ibises into the wild in this way will cause them to perish. There are no adult Northern Bald Ibises that know the migration route. Migration should be regulated like in Europe [43]. It is wrong to leave Northern Bald Ibis chicks outside without teaching them the migration route.

Ethical statement

The author declare that this document does not require ethics committee approval or any special permission.

Conflicts of Interest

The authors confirm that this article's content has no conflict of interest.

Author Contributions

A.K: Writing - Original draft preparation

E.U: Statistical analysis

References

[1] Böhm, C., Bowden, C.G.R., Seddon, P.J., Hatipoğlu, T., Oubrou, W., El Bekkay, M., Quevedo, M.A., Fritz, J., Yeniyurt, C., Lopez, J.M., Orueta, J.F., Frigerio, D. and Unsöld, M., "The northern bald ibis *Geronticus eremita*: History, current status and future perspectives", *Oryx*, 55(6), 934-946, 2021. https://doi.org/10.1017/S0030605320000198

[2] Böhm, C.,"Der Waldrapp -eine (un)endliche Geschichte?- Aktueller Status im Freiland und in Zoos, Schutzprojekte – eine Übersicht". *Zeitschrift des Kölner Zoos* 62(2):107-123, 2019.

[3] Schenker, A. and Serra, G. " Review of historical breeding sites of the Northern Bald Ibis *Geronticus eremita* in Syria and south-eastern Turkey". *Bird Conserv. Interna.* 32, 137-146, 2022.   https://doi.org/10.1017/S0959270921000010

[4] Hirsch, U., "Studies of West Palearctic birds. 183 Bald Ibis". *Brit, Birds* 72: 313-325, 1979.

[5] Şahin, R., "Kelaynak Kuşlarının (Geronticus eremita) Davranış ve Biyolojileri" *Habilitation. Dicle University*, Diyarbakır, Türkiye 1980.

[6] Pegoraro, K., "Der Waldrapp: vom Ibis, den man für einen Raben hielt". *AULA*. Wiesbaden, Germany, 1996.

[7] Parmaksız, A., Yığın, A., & Bozkaya, F. Determination of genetic structure of Bald ibis population living in Birecik (Türkiye) using mtDNA COI sequences. *Biological Diversity and Conservation*, *16*(1), 31-37, 2023.

[8] Akçakaya, H.R., "Bald Ibis *Geronticus eremita* population in Turkey: An evaluation of the captive breeding Project for reintroduction". *Biol. Conserv*. 51:225-237,1990.

[9] Akçakaya, H.R., Akçakaya, R., Barış, Y.S.,"Birecik'teki Kelaynak (*Geronticus eremita*) populasyonunun yok olma nedenleri ve koruma çalışmalarının değerlendirilmesi". *Doğa-Turkish Journal of Zoology*, 16, 1–12,1992.

[10] Hatipoğlu,T., "Northern BaldIbis Project at Birecik Breeding Centre: yesterday, today and tomorrow". (in: Boehm C. & Bowden, C. G. R.-eds. Northern Bald Ibis Conservation and Reintroduction workshop.) *Proceedings of 3rd Meeting of International Advisory Group for Northern Bald Ibis (IAGNBI)*, Palmyra, Syria. November 2009 pp.91, 2010.

[11] Serra, G., Lindsell, J. A., Peske, L., Fritz, J., Bowden, C. G. R., Bruschini, C. & Wondafrash, M., "Accounting for the low survival of the Critically Endangered northern bald ibis *Geronticus eremita* on a major migratory flyway". *Oryx*, 49(2), 312–320, 2015.

[12] Schenker, A., Cahenzli, F., Gutbrod, K.G., Thevenot, M. and Erhardt, A., "The Northern Bald Ibis *Geronticus eremita* in Morocco since 1900: Analysis of ecological requirements". *Bird Cons. Intn*. 1-22, 2019.   https://doi.org/10.1017/S0959270919000170

[13] Serra, G., Abdallah, M., Assaed, A., Abdallah, A., Al Qaim, G., Fayad, T. and Williamson, D. "Discovery of a relict breeding colony of northern bald ibis *Geronticus eremita* in Syria. *Oryx*, 38 (1), 1–7, 2004.

[14] Serra, G., Peske, L., Abdallah, M.S., al Qaim, G. and Kanani, A., "Breeding ecology and Behaviour of the last wild oriental Northern Bald Ibises (*Geronticus eremita*) in Syria". *J.Ornithology* 150: 769-782, 2009. https://doi.org/10.1007/s10336-009-0398-y

[15] Schenker, A., Cahenzli, F., Gutbrod, K.G., Thevenot, M. and Erhardt, A., "The Northern Bald Ibis *Geronticus eremita* in Morocco since 1900: Analysis of ecological requirements". *Bird Cons. Intn*. 1-22, 2019.   https://doi.org/10.1017/S0959270919000170

[16] Bowden, C.G.R., Orueta, J.F., Vazquez, J.M.L., Onrubia, A., Quevedo, M.A.,"Sightings of reintroduced northern bald ibis *Geronticus eremita* crossing between Spain and Morocco are probably hand-reared rather than wild-born". *Oryx*, 52(3), 411–412, 2018 https://doi.org/10.1017/S0030605318000479

[17] Fritz, J., "Life Northern Bald Ibis Wiederansiedlung des Waldrapp in Europa Jahresbericht 2017. Reintroduction of the Northern Bald Ibis". *LIFE+12-BIO_AT_000143, LIFE Northern Bald Ibis | Waldrappteam,* 2018.

[18] Bird Life, "Red List update for birds: iconic species saved from extinction by conservation action. Conservation successes. Northern Bald Ibis population has reached a modern record and expanded to new breeding sites (Morocco)". *International Press Release. Embargoed until 00:01 AM GMT on 22 November* 2018.

[19] IUCN, "Northern Bald Ibis *Geronticus eremita*". *The IUCN Red List of Threatened Species 2018:* Downloaded on 18 March 2021. https://dx.doi.org/10.2305/IUCN.UK.2018-2.RLTS.T22697488A130895601.en

[20] Touti, J.,Oumellouk, F., Bowden, C.G.R., Kirkwood, J.K. and Smith, K.W., "Mortality incident in northern bald ibis *Geronticus eremita* in Morocco in May 1996". *Oryx*, 33(2) 160-167, 1999. https://doi.org/10.1046/j.1365-3008.1999.00050.x

[21] Quevedo Muñoz, M. A., López Vazques, J. M., Aguilera Prieto, E., "Update of Proyecto eremita".(Edit: Böhm, C., Bowden, C.G.R., Jordan, M.J.R. and King, C.), *Northern Bald Ibis Conservation and Reintroduction workshop*. 2 nd IAGNBI Meeting, September, Vejer, Spain. 2006.

[22] Quevedo, M. A., "Update report of Proyecto Eremita, March 2010". (in: Boehm, C. & Bowden, C. G. R. (eds). *Northern Bald Ibis Conservation and Reintroduction workshop.) Proceedings of 3rd Meeting of International Advisory Group for Northern Bald Ibis (IAGNBI)* (ISBN 978-1-905601-27-1), Palmyra, Syria. November, pp.91, 2009.

[23] Kılıç, A., "Reproduction Success of Northern Bald Ibises (*Geronticus eremita*) -2016". *XIII.Cogress of Ecology and Environment with İnternational Participation.* Oral Presentation. 12-15 September Edirne Trakya University, 2016.

[24] Arihan, O., "Recent Information on the occurrence of the Northern Bald Ibis *Geronticus eremita* inTurkey". *Turna* 1:10-15, 1998.

[25] Özbağdatlı, N., Hatipoğlu, T., Kurt, B., Arıhan, O., Tavares, J. and Bowden, C., "Outline of a proposed collaborative Project to monitor and develop the Bireçik semi-wild Northern Bald Ibis population". (in edit C.Bowden, An update on current projects involving wild and captive Northern Bald Ibis *Geronticus eremita*) *I.A.G.N.B.I. Newsletter 1*. September 2001.

[26] Özbağdatlı, N., "Northern Bald Ibis Project at the Birecik Breeding Centre". (Edit: Böhm, C., Bowden, C.G.R., Jordan, M.J.R. and King, C., *Northern Bald Ibis Conservation and Reintroduction workshop. 2 nd IAGNBI Meeting*, September, Vejer-Spain, 2007.

[27] Bowden, C., Böhm, C., Lopez, J.M., Hatipoglu, T., "Draft update to Release guidelines and methodology for Northern Bald Ibis *Geronticus eremita*". (in eds. Böhm, C. & Bowden, C.G.R.

Northern Bald Ibis Conservation and Translocation Workshop), 2016.
https://doi.org/10.13140/RG.2.2.16913.63845

[28] Kılıç, A., "Numerical Changes in Northern Bald Ibis (*Geronticus eremita*)". 24th National Biology Congress. *Proceedings Book*, (ISBN 978-975-8628-71-1)10-14 September, Manisa-Türkiye, 2018.

[29] Kılıç, A., "Near-Extinct Northern Bald Ibis (*Geronticus eremita*)". Agriculture and Bird Diversity Workshop in Diyarbakır. *Oral Presentation*. *Proceedings Book*. 10 October, Dicle Univ. Diyarbakır, 2019.

[30] Kılıç, A., "Losses and Deaths in the Northern Bald Ibıs Population (2012-2020)". International Engineering and Natural Sciences Conference (IENSC 2020) (ISBN 978-605-81971-9-0). Oral Presentation. *Proceedings Book* 5-6 November , Dicle University, Diyarbakır, Türkiye, 2020.

[31] Kılıç, A., "Challenges Facing Northern Bald Ibis (*Geronticus eremita*)-2021". 4th National Applied Biological Sciences Congress. *Oral Presentation. Online*. *Proceedings Book*, S 33 (E-ISBN: 978-605-71081-3-5). 06-07 December, 2021.

[32] Kılıç, A.,"2018-2022 Losses of Northern Bald Ibis Population". 5th National Zoology Congress, Oral Presentation. Online, *Proceedings Book* (E-ISBN:978-605-72835-4-2) 2-3 December, 2022.

[33] Safriel, U.N., "Notes on the Extinct Population of the Bald Ibis *Gerontıcus eremita* in the Syrian Desert". *Ibis* 122: 82-88, 1980.

[34] Yeniyurt, C., Oppel, S., İsfendiyaroğlu, S., Özkınacı, G., Erkol, I.L., & Bowden, C.G.R., "Influence of feed ingecology on breeding success of a semi-wildpopulation of the critically endangered Northern Bald Ibis *Geronticus eremita* in southern Turkey". *Bird Conservation International*, 27: 537–549, 2017.   https://doi.org/10.1017/S0959270916000253

[35] Serra, G. & Peske, L., "Northern Bald Ibis conservations efforts in Syria 2002-2006: results and lessons learned". (Edit: Böhm, C.,Bowden, C.G.R., Jordan, M.J.R. and King, C., Northern Bald Ibis Conservation and Reintroduction workshop. *2 nd IAGNBI Meeting* September, Vejer, Spain, 2007.

[36] El Bekkay, M.,Oubrou,W., Smith, K.W., Bowden, C.G.R. and Armesto, M.J.J., "Northern Bald Ibis conservation Project In Souss Massa region" (in Edits Böhm, C., Bowden, C.G.R., and Jordan, M., Northern Bald Ibis Conservation and Reintroduction Workshop.) *Proceeding of the IAGNBI Meeting* Innsbruck-Tirol. July., pp.25-30, 2003.

[37] Bowden, C.G.R., Agnaj, A., Smith, K.W. and Ribi, M., "The status and recent breeding performance of the critically endangered Northern Bald Ibis *Geronticus eremita* population on the Atlantic coast of Morocco". *Ibis* 145: 419-431, 2003.

[38] El Bekkay, M., Oubrou,W., Ribi, M., Smith, K., and Bowden, C.G.R., "Un programme de conservation pour l'ibis chauve (*Geronticus eremita*) au Maroc". *Ostrich*, 78(2): 155–157, 2007.

[39] Bowden C.G.R., Smith K.W., El Bekkay. M, Oubrou, W., Aghnaj, A. and Jimenez-Armesto, M., "Contribution of research to conservation action for the Northern Bald Ibis *Geronticus eremita* in Morocco". *Bird Conservation International,* 18: 74–90, 2008.

[40] Oubrou, W. & El Bekkay, M., "*Rapport* sur la reproduction de l'Ibis Chauve *Geronticus eremita* dans la région de Souss-Massa Saison 2017". 2017.

[41] Aourir, M., Bousadik, H., El Bekkay, M., Oubrou, W., Znari, M. & Qninba, A., "New Breeding sites of the critically endangered northern bald ibis *Geronticus eremita* on the moroccan atlantic coast". *Int J Avian & Wildlife Biol.* 2(3):77–80, 2017. https://doi.org/10.15406/ijawb.2017.02.00021

[42] Smith, K.N., Aghnaj, A., El Bekkay, M., Oubrou, W., Ribi, M., Armesto, M.J. & Bowden, C.G.R., "The provision of supplementary fresh water improves the breeding success of the globally threatened Northern Bald Ibis *Geronticus eremita*". *Ibis* 150 (4), 728–734, 2008. https://doi.org/10.1111/j.1474-919X.2008.00844.x

[43] Fritz, J., Kramer, R., Hoffmann, W., Trobe, D. & Unsöld, M., "Back into the wild: establishing a migratory Northern bald ibis *Geronticus eremita* population in Europe". *Int. Zoo Yb*.51: 107–123, 2017. https://doi.org/10.1111/izy.12163

[44] Murray, N.J. & Shaw, P.P., "Breeding Biology of the Australian White Ibıs *Threskiornis molucca* at an Urban Breeding Colony south-east Queensland". *Corella*, 30(2): 41-45, 2006.

[45] Wirtz, S., Böhm. C.,Fritz, J.,Kotrschal, K., Veith M., Hochkirc, A., "Optimizing the genetic management of reintroduction projects: genetic population structure of the captive Northern Bald Ibis population". *Conservation Genetics* 19(4) 853-864, 2018. https://doi.org/10.1007/s10592-018-1059-6

[46] Serra G.,"The Last Flight of the Ancient Guide of *Hajj*". *Self published. Apia,* Samoa.74 pp., 2017.

[47] Serra, G. & Wondafrash, M., "Eco-ethologıcal and Conservatıon Survey of N. Bald Ibıses Wintering in the Northern Shawa (Ethiopia) During 2008-09". *Fınal Report IUCN West Asia / DGCS Trust Fund Pilot Project*. Ethiopian Wildlife and Natural History Society / IUCN. April, 22pp, 2009.

[48] Böhm, C., "Problems and demands of the selection of release sites for the Northern Bald Ibis". (in eds. Böhm, C. & Bowden, C.G.R. *Northern Bald Ibis Conservation and Translocation Workshop*), 2016. https://doi.org/10.13140/RG.2.2.16913.63845

[49] Erdoğan, İ., " https://www.aa.com.tr/tr/yasam/kelaynaklara-yeni-yuva-arayisi/900920" , 2017.

[50] Çiçek, A., "https://www.aa.com.tr/tr/yasam/sanliurfada-dogaya-salinan-30-kelaynak-kusundan-4une-goc-yolunu-takip-icin-gprs-takildi/2939307" , 2023.

[51] Yeniyurt, C., "Trevor Poyser Species Conservation Fund supports Northern Bald Ibis conservation in Türkiye". *OSME, NEWS* 13/06/ 2023.   https://osme.org/2023/06/trevor-poyser-species-conservation-fund-supports-northern-bald-ibis-conservation-in-turkiye/

Middle East Journal of Science

https://dergipark.org.tr/mejs

MEJS

Research Article

NEW GENERALIZED DIFFERENCE SEQUENCE SPACES AND THEIR KÖTHE-TOEPLITZ DUALS

Gülcan ATICI TURAN*¹ (iD)

¹ Munzur University, Vocational School of Tunceli, Türkiye
* Corresponding author; gatici23@hotmail.com

Abstract: *We will define the sequence spaces* $c_0(u,\Delta_v^m)_p$, $c(u,\Delta_v^m)_p$ *and* $\ell_\infty(u,\Delta_v^m)_p$ *in this article. Furthermore, we give some topological properties and compute their Köthe-Toeplitz duals.*

Keywords: *Difference sequence spaces, α-, β- and γ- dual.*

1. Introduction

We show w display the set of all sequences $x = (x_k)$, and c_0, ℓ_∞ and c, the linear spaces of null, bounded and convergent sequences with real terms, respectively, normed by $\|x\|_\infty = \sup_k |x_k|$. In all this study we use X instead of c_0, ℓ_∞ and c. The difference in sequence spaces

$$X(\Delta) = \{x = (x_k): \Delta x \in X\}$$

first defined by Kızmaz [1]. Et and Çolak [2] generalized this.

Later, Et and Esi [3] widened the difference sequence spaces to the sequence spaces
$$X(\Delta_v^m) = \{x = (x_k): (\Delta_v^m x_n) \in X\}$$
where $v = (v_n)$ be any fixed sequence of non-zero complex numbers and such that

$$(\Delta_v^m x_n) = (\Delta_v^{m-1} x_n - \Delta_v^{m-1} x_{n+1}), \quad \Delta_v^m x_n = \sum_{i=0}^m (-1)^i \binom{m}{i} v_{n+i} x_{n+i}.$$

Bektaş, Et and Çolak [4] defined the sequence spaces $\Delta_v^m(X)$ for $X = \ell_\infty$, c and c_0, and worked out β - and γ - duals of the these.

Definition 1.1. Let X be a sequence space.

$$X^\alpha = \left\{ a \in w: \sum_{n=1}^\infty |a_n x_n| < \infty, \text{for all } x \in X \right\}$$

$$X^\beta = \left\{ a \in w: \sum_{n=1}^\infty a_n x_n \text{ converges}, \text{for all } x \in X \right\}$$

$$X^\gamma = \left\{ a \in w: \sup_k \left| \sum_{n=1}^k a_n x_n \right| < \infty, \text{for all } x \in X \right\},$$

are called α-, β-, γ- dual spaces of X, respectively. $\emptyset \subset X^\alpha \subset X^\beta \subset X^\gamma$ is shown. Since $X \subset Y$, $Y^\eta \subset X^\eta$ for $\eta = \alpha, \beta, \gamma$. We have $X^{\alpha\alpha} = (X^\alpha)^\alpha$.

Et and Başarır [5] defined the sequence spaces
$$\Delta^m(X) = \{x = (x_n): \Delta^m x \in X(p)\}$$

for $m \in \mathbb{N}$, where $X = \ell_\infty$, c or c_0.

Let U be the set of all sequences $u = (u_n)$ such that $u_n \neq 0$ and complex for all $n = 1,2, \dots$. Throughout the paper we write $w_n = 1/|u_n|$.

Malkowsky [6] defined the sequence spaces

$$X(u, \Delta) = \left\{ x \in w : \left(u_n(x_n - x_{n+1}) \right)_{n=1}^\infty \in X \right\}$$

where $u \in U$ and $X = \ell_\infty$, c or c_0.

After Asma and Çolak [7] defined the sequence spaces

$$X(u, \Delta, p) = \{ x \in w : (u_n \Delta x_n)_{n=1}^\infty \in X(p) \}$$

where $u \in U$ and $X = \ell_\infty$, c or c_0.

Recently Bektaş, A. [8] defined the sequence spaces

$$X(u, \Delta^2, p) = \{ x \in w : (u_n \Delta^2 x_n)_{n=1}^\infty \in X(p) \}$$

where $\Delta^2 x = (\Delta^2 x_n)_{n=1}^\infty = (\Delta x_n - \Delta x_{n+1})_{n=1}^\infty$.

Many studies have been carried out on dual and Köthe-Toeplitz dual etc. ([9], [10]).

2. Main Results

Let us consider $p = (p_n)$ as a sequence of strictly positive real numbers thought this study.

We define the sequence spaces as follows:

$$\ell_\infty(u, \Delta_v^m)_p = \{ x \in w : (u_n \Delta_v^m x_n) \in \ell_\infty(p) \},$$

$$c(u, \Delta_v^m)_p = \{ x \in w : (u_n \Delta_v^m x_n) \in c(p) \},$$

$$c_0(u, \Delta_v^m)_p = \{ x \in w : (u_n \Delta_v^m x_n) \in c_0(p) \}$$

for $p = (p_n)$, $m \in \mathbb{N}$ and $u \in U$.

Theorem 2.1. $c_0(u, \Delta_v^m)_p$, $c(u, \Delta_v^m)_p$ and $\ell_\infty(u, \Delta_v^m)_p$ are linear spaces.

Theorem 2.2. Let $p = (p_n)$ be bounded and $M = max(1, H = sup_n p_n)$. Then $\ell_\infty(u, \Delta_v^m)_p$ and $c_0(u, \Delta_v^m)_p$ are linear topological spaces by g, defined by

$$g(x) = \sup_n |u_n \Delta_v^m x_n|^{p_n/M}.$$

Furthermore $c(u, \Delta_v^m)_p$ is paranormed by g if $inf_n p_n > 0$.

Theorem 2.3. For every $p = (p_n)$,

(i) $\left[\ell_\infty(u, \Delta_v^m)_p \right]^\alpha = D_\alpha(u, p) = \bigcap_{S=2}^\infty \left\{ a \in w : \sum_{n=1}^\infty |a_n| |v_n|^{-1} \sum_{i=1}^{n-m} \binom{n-i-1}{m-1} S^{1/p_i} w_i < \infty \right\}$,

(ii) $\left[\ell_\infty(u, \Delta_v^m)_p \right]^{\alpha\alpha} = D_{\alpha\alpha}(u, p) = \bigcup_{S=2}^\infty \left\{ a \in w : \sup_{n \geq m+1} |a_n| |v_n| \left[\sum_{i=1}^{n-m} \binom{n-i-1}{m-1} S^{1/p_i} w_i \right]^{-1} < \infty \right\}$.

Proof. (i) Let $x \in \ell_\infty(u, \Delta_v^m)_p$ and $a \in D_\alpha(u, p)$. We choose $S > max\{1, sup_k |u_k \Delta_v^m x_k|^{p_k}\}$. Since

$$\sum_{i=1}^{n-m} \binom{n-i-1}{m-1} S^{1/p_i} w_i > \sum_{i=1}^{m} \binom{n-i-1}{m-1} S^{1/p_i} w_i$$

for arbitrary $S > 1$ ($n = 2m, 2m + 1, \dots$) and $|u_i \Delta_v^{m-i} x_i| \leq M$ ($1 \leq i \leq m$) for some constant M, $a \in D_\alpha(u, p)$ implies

$$\sum_{n=1}^\infty |a_n| |v_n|^{-1} \sum_{i=1}^{m} \binom{n-i-1}{m-1} |\Delta_v^{m-i} x_i| < \infty.$$

Since,

$$x_n = |v_n|^{-1}\left(\left|\sum_{i=1}^{n-m}(-1)^m\binom{n-i-1}{m-1}\Delta_v^m x_i + \sum_{i=1}^{m}(-1)^{m-i}\binom{n-i-1}{m-1}\Delta_v^{m-i}x_i\right|\right),$$

we can write

$$\sum_{n=1}^{\infty}|a_n x_n| = \sum_{n=1}^{\infty}|a_n||v_n|^{-1}\left(\left|\sum_{i=1}^{n-m}(-1)^m\binom{n-i-1}{m-1}\Delta_v^m x_i + \sum_{i=1}^{m}(-1)^{m-i}\binom{n-i-1}{m-1}\Delta_v^{m-i}x_i\right|\right)$$

$$\leq \sum_{n=1}^{\infty}|a_n||v_n|^{-1}\sum_{i=1}^{n-m}\binom{n-i-1}{m-1}|\Delta_v^m x_i| + \sum_{n=1}^{\infty}|a_n||v_n|^{-1}\sum_{i=1}^{m}\binom{n-i-1}{m-1}|\Delta_v^{m-i}x_i|$$

$$\leq \sum_{n=1}^{\infty}|a_n||v_n|^{-1}\sum_{i=1}^{n-m}\binom{n-i-1}{m-1}S^{1/p_i}w_i + \sum_{n=1}^{\infty}|a_n||v_n|^{-1}\sum_{i=1}^{m}\binom{n-i-1}{m-1}|\Delta_v^{m-i}x_i|$$

$$< \infty.$$

Therefore $a \in \left[\ell_\infty(u,\Delta_v^m)_p\right]^\alpha$.

Conversely, let $a \notin D_\alpha(u,p)$. Then for some integer $S > 1$, we have

$$\sum_{n=1}^{\infty}|a_n||v_n|^{-1}\sum_{i=1}^{n-m}\binom{n-i-1}{m-1}S^{1/p_i}w_i = \infty.$$

If we define the sequence $x = (x_n)$ by

$$x_n = v_n^{-1}\sum_{i=1}^{n-m}\binom{n-i-1}{m-1}S^{1/p_i}w_i \qquad (n = m+1, m+2,\dots),$$

then we obtain that $x \in \ell_\infty(u,\Delta_v^m)_p$ and $\sum_n|a_n x_n| = \infty$. So $a \notin \left[\ell_\infty(u,\Delta_v^m)_p\right]^\alpha$.

(ii) Let $a \in D_{\alpha\alpha}(u,p)$ and $x \in \left[\ell_\infty(u,\Delta_v^m)_p\right]^\alpha = D_\alpha(u,p)$, by part (i). Then for some $S > 1$, we can write

$$\sum_{n=1}^{\infty}|a_n x_n| = \sum_{n=m+1}^{\infty}|a_n||v_n|\left[\sum_{i=1}^{n-m}\binom{n-i-1}{m-1}S^{1/p_i}w_i\right]^{-1}|x_n||v_n|^{-1}\sum_{i=1}^{n-m}\binom{n-i-1}{m-1}S^{1/p_i}w_i$$

$$\leq \sup_{n\geq m+1}\left\{|a_n||v_n|\left[\sum_{i=1}^{n-m}\binom{n-i-1}{m-1}S^{1/p_i}w_i\right]^{-1}\right\}\cdot\sum_{n=m+1}^{\infty}|x_n||v_n|^{-1}\sum_{i=1}^{n-m}\binom{n-i-1}{m-1}S^{1/p_i}w_i.$$

Hence $\sum_{n=1}^{\infty}|a_n x_n| < \infty$, i.e., $a \in \left[\ell_\infty(u,\Delta_v^m)_p\right]^{\alpha\alpha}$.

Conversely, let $a \in \left[\ell_\infty(u,\Delta_v^m)_p\right]^{\alpha\alpha}$, but $a \notin D_{\alpha\alpha}(u,p)$. Hence for all integers $S > 1$, we can write

$$\sup_{n\geq m+1}|a_n||v_n|\left[\sum_{i=1}^{n-m}\binom{n-i-1}{m-1}S^{1/p_i}w_i\right]^{-1} = \infty.$$

We recall that $\sum_{i=1}^{n-m}\binom{n-i-1}{m-1}y_i = 0$ $(n < m+1)$ for optionally y_i. Therefore, there is a strictly increasing sequence $(n(s))$ of integers $n(s) \geq m+1$ such that

$$|a_{n(s)}||v_{n(s)}|\left[\sum_{i=1}^{n(s)-m}\binom{n(s)-i-1}{m-1}S^{1/p_i}w_i\right]^{-1} > s^{m+1} \quad (s = m+1, m+2,\dots).$$

We define the sequence $x = (x_n)$ with

$$x_n = \begin{cases} |a_{n(s)}|^{-1}, & n = n(s) \\ 0 & , n \neq n(s) \end{cases} \quad (n = m+1, m+1, \dots).$$

Then for all integers $S > m + 1$, we can write

$$\sum_{n=1}^{\infty} |a_n||v_n|^{-1} \sum_{i=1}^{n-m} \binom{n-i-1}{m-1} S^{1/p_i} w_i \leq \sum_{s=m+1}^{\infty} |a_{n(s)}|^{-1}|v_{n(s)}|^{-1} \sum_{i=1}^{n(s)-m} \binom{n(s)-i-1}{m-1} S^{1/p_i} w_i$$

$$\leq \sum_{s=m+1}^{S-1} |a_{n(s)}|^{-1}|v_{n(s)}|^{-1} \sum_{i=1}^{n(s)-m} \binom{n(s)-i-1}{m-1} S^{1/p_i} w_i$$

$$+ \sum_{s=S}^{\infty} |a_{n(s)}|^{-1}|v_{n(s)}|^{-1} \sum_{i=1}^{n(s)-m} \binom{n(s)-i-1}{m-1} S^{1/p_i} w_i.$$

Hence $x \in \left[\ell_\infty(u, \Delta_v^m)_p\right]^\alpha$ and $\sum_{n=1}^{\infty}|a_n x_n| = \sum_{S=1}^{\infty} 1 = \infty$. Thus $a \notin \left[\ell_\infty(u, \Delta_v^m)_p\right]^{\alpha\alpha}$.

Theorem 2.4. For every $p = (p_n)$ and $u \in U$,

(i) $\left[c_0(u, \Delta_v^m)_p\right]^\alpha = M_\alpha(u, p) = \bigcup_{S=2}^{\infty} \left\{ a \in w: \sum_{n=1}^{\infty} |a_n| v_n^{-1} \sum_{i=1}^{n-m} \binom{n-i-1}{m-1} S^{-1/p_i} w_i < \infty \right\},$

(ii) $\left[c_0(u, \Delta_v^m)_p\right]^{\alpha\alpha} = M_{\alpha\alpha}(u, p) = \bigcap_{S=2}^{\infty} \left\{ a \in w: \sup_{n \geq m+1} |a_n| \left[\sum_{i=1}^{n-m} \binom{n-i-1}{m-1} S^{-1/p_i} w_i \right]^{-1} < \infty \right\}.$

Proof. (i) Let $x \in c_0(u, \Delta_v^m)_p$ and $a \in M_\alpha(u, p)$. Then there is an integer $S > 1$ such that $|u_n \Delta_v^m x_n|^{p_n} \leq S^{-1}$. Since

$$\sum_{i=1}^{n-m} \binom{n-i-1}{m-1} S^{-1/p_i} w_i > \sum_{i=1}^{m} \binom{n-i-1}{m-1} S^{-1/p_i} w_i$$

$a \in M_\alpha(u, p)$ implies

$$\sum_{n=1}^{\infty} |a_n||v_n|^{-1} \sum_{i=1}^{m} \binom{n-i-1}{m-1} |\Delta_v^{m-i} x_i| < \infty.$$

Then

$$\sum_{n=1}^{\infty} |a_n x_n| = \sum_{n=1}^{\infty} |a_n||v_n|^{-1} \left(\left| \sum_{i=1}^{n-m} (-1)^m \binom{n-i-1}{m-1} \Delta_v^m x_i + \sum_{i=1}^{m} (-1)^{m-i} \binom{n-i-1}{m-1} \Delta_v^{m-i} x_i \right| \right)$$

$$\leq \sum_{n=1}^{\infty} |a_n||v_n|^{-1} \sum_{i=1}^{n-m} \binom{n-i-1}{m-1} S^{-1/p_i} w_i + \sum_{n=1}^{\infty} |a_n||v_n|^{-1} \sum_{i=1}^{m} \binom{n-i-1}{m-1} |\Delta_v^{m-i} x_i|$$

$$< \infty.$$

Hence $a \in \left[c_0(u, \Delta_v^m)_p\right]^\alpha$.

Conversely, let $a \notin M_\alpha(u, p)$. Hence we can define a strictly increasing sequence $(n(s))$ of integers such that

$$M_\alpha(u, p) = \sum_{n=n(s)}^{n(s+1)-1} |a_n||v_n|^{-1} \sum_{i=1}^{n-m} \binom{n-i-1}{m-1} (s+1)^{-1/p_i} w_i > 1 \quad (s = 1, 2, \dots)$$

where $n(1) = 1$.

We define sequence $x = (x_n)$ such that

$$x_n = v_n^{-1} \sum_{i=1}^{n-m} \binom{n-i-1}{m-1} (s+1)^{-1/p_i} w_i.$$

Then $|u_n \Delta_v^m x_n|^{p_n} = \frac{1}{s+1} (n(s) \leq n \leq n(s+1) - 1; s = 1, 2, \dots)$. Hence

$$\sum_{n=1}^{\infty} |a_n x_n| = \sum_{n=1}^{\infty} |a_n| |v_n|^{-1} \sum_{i=1}^{n-m} \binom{n-i-1}{m-1} (s+1)^{-1/p_i} w_i > 1$$

and $x \in c_0(u, \Delta_v^m)_p$. Hence $a \notin \left[c_0(u, \Delta_v^m)_p\right]^{\alpha}$. This is a contradiction. Therefore $a \in M_\alpha(u, p)$.

(ii) Proof is smilar to [11].

Theorem 2.5. For every $p = (p_n)$,

$$\left[c(u, \Delta_v^m)_p\right]^{\alpha} = \mathbf{D}_v^m(p)$$

where

$$\mathbf{D}_v^m(p) = M_\alpha(u, p) \cap \left\{ a \in w: \sum_{n=1}^{\infty} |a_n| |v_n^{-1}| \sum_{i=1}^{n-m} \binom{n-i-1}{m-1} w_i < \infty \right\}.$$

Proof. Let $a \in \mathbf{D}_v^m(p)$ and $x \in c(u, \Delta_v^m)_p$. Then there is a complex number λ such that $|u_n \Delta_v^m x_n - \lambda|^{p_n} \to 0$ $(n \to \infty)$. We define $y = (y_n)$ with

$$y_n = x_n + \lambda v_n^{-1} \sum_{i=1}^{n-m} \binom{n-i-1}{m-1} u_i^{-1}.$$

Then $y \in c_0(u, \Delta_v^m)_p$ and

$$\sum_{n=1}^{\infty} |a_n x_n| = \sum_{n=1}^{\infty} |a_n| \left| y_n - \lambda v_n^{-1} \sum_{i=1}^{n-m} \binom{n-i-1}{m-1} u_i^{-1} \right|$$

$$\leq \sum_{n=1}^{\infty} |a_n| |y_n| + |\lambda| \sum_{n=1}^{\infty} |a_n| |v_n^{-1}| \sum_{i=1}^{n-m} \binom{n-i-1}{m-1} w_i$$

$$< \infty.$$

Hence $a \in \mathbf{D}_v^m(p)$.

Now let $a \in \left[c(u, \Delta_v^m)_p\right]^{\alpha}$. Since $\left[c(u, \Delta_v^m)_p\right]^{\alpha} \subset \left[c_0(u, \Delta_v^m)_p\right]^{\alpha}$ and $\left[c_0(u, \Delta_v^m)_p\right]^{\alpha} = M_\alpha(u, p)$ by Theorem 2.1 (i), then $a \in M_\alpha(u, p)$. If we put

$$x_n = v_n^{-1} \sum_{i=1}^{n-m} \binom{n-i-1}{m-1} w_i,$$

then $x \in c(u, \Delta_v^m)_p$ and therefore

$$\sum_{n=1}^{\infty} |a_n| |v_n^{-1}| \sum_{i=1}^{n-m} \binom{n-i-1}{m-1} w_i < \infty.$$

Thus $a \in \mathbf{D}_v^m(p)$.

Theorem 2.6. For every $p = (p_n)$,

(i) $\left[\ell_\infty(u, \Delta_v^m)_p\right]^{\beta} = \mathbf{D}_v^{\beta}(p)$,

(ii) $\left[\ell_\infty(u, \Delta_v^m)_p\right]^{\gamma} = \mathbf{D}_v^{\gamma}(p)$,

where

$$D_v^\beta(p) = \bigcap_{S=2}^{\infty} \left\{ a \in w : \sum_{n=1}^{\infty} a_n v_n^{-1} \sum_{i=1}^{n-m} \binom{n-i-1}{m-1} S^{1/p_i} w_i \text{ converges and} \right.$$

$$\left. \sum_{n=1}^{\infty} |R_n| \sum_{i=1}^{n-m+1} \binom{n-i-1}{m-2} S^{1/p_i} w_i < \infty \right\},$$

$$D_v^\gamma(p) = \bigcap_{S=2}^{\infty} \left\{ a \in w : \sup_n \left| \sum_{n=1}^{\infty} a_n v_n^{-1} \sum_{i=1}^{n-m} \binom{n-i-1}{m-1} S^{1/p_i} w_i \right| < \infty, \right.$$

$$\left. \sum_{n=1}^{\infty} |R_n| \sum_{i=1}^{n-m+1} \binom{n-i-1}{m-2} S^{1/p_i} w_i < \infty \right\},$$

and $R_n = \sum_{i=n+1}^{\infty} v_i^{-1} a_i$ $(n = 1, 2, \dots)$.

Proof. Proof is smilar to [11]. So we omitted it.

3. Conclusion

Numerous branches of mathematics use the theory of sequence space, such as the structural theory of topological vector spaces, summability theory, and function space theory. However, the convergence issues that arise from the subject place it under analysis rather than algebra.

Given that sequence convergence is a crucial concept in the foundational theory of mathematics, numerous convergence notions arise in areas such as summability theory, classical measure theory, approximation theory, and probability theory, with discussions focusing on the relationships between them.

Researchers in this field may explore the topological and geometric characteristics of these sequence spaces.

Ethical statement

The author declares that this document does not require ethics committee approval or any special permission. Our study does not cause any harm to the environment.

Conflict of interest

The author declares no potential conflicts of interest related to this article's research, authorship, and publication.

References

[1]   Kızmaz, H., "On Certain Sequence Spaces", *Canad. Math. Bull.,* 24, 169-176, 1981.

[2]   Et, M., Çolak, R., "On Some Generalized Difference Sequence Spaces", *Soochow J. Math.,* 21, 377-386, 1995.

[3]   Et, M., Esi, A., "On Köthe-Toeplitz Duals of Generalized Difference Sequence Spaces", *Bull Malaysian Math. Sc. Soc.,* 23(2), 1-8, 2000.

[4]   Bektaş, Ç. A., Et, M., Çolak, R., "Generalized Difference Sequence Spaces and Their Dual Spaces", *J. Math. Anal. Appl.,* 292, 423-432, 2004.

[5]   Et, M., Başarır, M., "On Some New Generalized Difference Sequence Spaces", *Periodica Math. Hungarica*, 35(3), 169-175, 1997.

[6]   Malkowsky, E., "A Note on the Köthe-Toeplitz Duals of Generalized Sets of Bounded and Convergent Difference Sequences", *J. Anal.,* 4, 81-91, 1996.

[7]   Asma, Ç., Çolak, R., "On the Köthe-Toeplitz Duals of Some Generalized Sets of Difference Sequences", *Dermonstratio Math.,* 4 , 797-803, 2000.

[8]   Bektaş, Ç. A., "On Some New Generalized Sequence Spaces", *J. Math. Anal. Appl.,* 277, 681-688, 2003.

[9]   Barlak D., Bektaş Ç.A., "Duals of generalized Orlicz Hilbert sequence spaces and matrix transformations", *Filomat*, 31(27), 9089-9102, 2023.

[10] Bektaş, Ç. A., "On Some Generalized Difference Sequence Spaces and Köthe Toeplitz Duals", *IeJEMTA*, 7, 61-72, 2009.

[11] Bektaş, Ç. A., "Absolute and Ordinary Köthe-Toeplitz Duals of Some Generalized Sets of Difference Sequences", *Hokkaido Mathematical Journal*, 33(1), 207-214, 2004.

Middle East Journal of Science

Research Article

ARCHIMEDES OPTIMIZATION ALGORITHM-BASED PITCH ANGLE CONTROL IN WIND ENERGY SYSTEMS

Hasan Bektas PERCIN [iD] **1, Abuzer CALISKAN* [iD] *2*

[1] Firat University, Elazig, Türkiye Orcid[1]: https://orcid.org/0000-0001-8968-969X
[2] Department of Electrical and Electronics Engineering, Firat University, Elazig, Türkiye
Orcid[2]: https://orcid.org/0000-0001-8262-7912
* Corresponding author; hbpercin@firat.edu.tr

Abstract: Variable-speed wind energy systems equipped with permanent magnet synchronous generators (PMSGs) have become a common configuration in wind energy industry. Appropriate pitch angle control is designed to limit the output power of the system by adjusting the pitch angle of the wind turbine blades at higher wind speeds. This approach reduces mechanical stress on the turbine, extends its operating speed range, and increases the overall lifespan. Intelligent control methods, such as optimization algorithms, are notable for their fast and reliable control performance; however, their use in pitch angle control applications remains relatively limited. In this study, a pitch angle control based on the Archimedes Optimization Algorithm (AOA) was developed and analyzed using MATLAB/Simulink. The proposed control system demonstrated fast and stable performance at higher wind speeds. Additionally, the control mechanism was set to deactivated at lower wind speeds to optimize energy efficiency for varying conditions. When compared to other conventional control methods, alternative approaches generally achieve an average accuracy of %75 to %80. However, the proposed control method performed a significantly faster convergence speed and achieved an accuracy rate exceeding %90.

Keywords: Wind energy; Archimedes optimization; Pitch angle; MATLAB/Simulink

1. Introduction

In recent years, pollution problems, increasing production costs, and the fast depletion of fossil energy sources have reached an indisputable level. Above all, industrial development and an increasing population across the world will increase limited fossil energy usage and lead to more emissions of greenhouse gases, which have consequences for global climate change [1, 2]. These problems lead to a remarkable transition and increasing investments in renewable energy sources. One of these, wind energy, has become a significant source due to its safe, pollutant-free, and inexhaustible nature. According to the 2023 Global Wind Energy Council (GWEC) report, 78 GW of new wind power capacity was added globally, making it the third-highest year for capacity expansion. The total installed capacity worldwide has reached 906 GW, representing a significant year-on-year growth rate of 9%. It is anticipated to be the first year to surpass 100 GW of newly added capacity globally, with a projected year-on-year growth of 15%, as forecasted by GWEC Market Intelligence. The future outlook is optimistic, with GWEC Market Intelligence predicting a substantial increase in new capacity over the next five years (2023–2027). The forecast suggests the addition of 680 GW of new capacity during this

period, averaging 136 GW per year until 2027. This signifies a significant upward trajectory in global capacity expansion in the coming years [3].

In principle, a wind energy conversion system (WECS) has three main components. The first component is the wind turbine. As the wind goes through the turbine blades, it makes the turbine shaft move, and this movement creates mechanical power. The second component is a drivetrain that transfers mechanical power to the generator. The last component is the electric generator, which converts mechanical power to electric power. Other control structures and interfaces are integrated into these main components [4, 5]. WECSs can be categorized into fixed-speed and variable-speed configurations. Variable-speed WECSs are more commonly used than fixed-speed types. The main advantages of variable-speed types are their ability to extract more energy, reduce mechanical stresses, and provide a longer working life [6]. For electrical generators, there are several types used with WECSs. Recently, the permanent magnet synchronous generator (PMSG) has gained great popularity due to its advantages, such as gearless operation, better reliability, and higher power density [7]. For WECSs, the rapid wind variations and system conditions require different control structures. Generally, there are two main controls used for WECSs. The first control is utilized for maximum power production efficiency below the rated wind speed, which provides the most efficient output power for a WECS. The second control aims to limit the instant power at higher wind speeds. This control is defined as pitch angle control [8, 9].

For pitch angle control of WECSs, various control methods have been studied in the literature. Controllers utilizing PID controllers are more convenient for small WECSs. They utilize various parameters such as wind speed, generator power, and rotor speed to derive appropriate pitch angle values through the controller [10–13]. However, PID-based controllers may not perform well due to the nonlinear characteristics of WECSs. Furthermore, the choice of controller gains can be a challenging task in response to instant wind variations. Some control methods are modified with different control structures to overcome these problems [14–16]. Due to the nonlinear system dynamics and wind speed variations, intelligent controllers have been developed. These controllers ensure flexible, fast, and autonomous control. These features have made their use widespread in all kinds of control applications. Such controllers include fuzzy logic, artificial neural networks, and various optimization algorithms. They are highly suitable techniques for stable pitch angle control of WECSs [17]. The fuzzy logic control (FLC)-based pitch control of WECSs provides many advantages, such as independence from system parameters, adaptability, and simplicity. However, fuzzy logic control (FLC) requires expert knowledge of the system to design the fuzzy interface and necessitates memory allocation [18–21]. Artificial neural networks (ANNs) are another method that emulates information processing by the neural structure of the brain. ANNs consist of neural layers, specified learning, and training algorithms. ANN-based WECS controls are commonly used for power optimization at higher wind speeds [22–25]. Recently, optimization algorithms have gained popularity in controlling nonlinear systems. They can be developed the social hierarchy of animals in the natural world or from various physical phenomena. [26]. They can be used for different control objectives and have advantages such as better adaptability, fast response, and independence from system parameters. Furthermore, they can be combined with other methods, defined as hybrid control structures. The genetic algorithm-based control method is one of the commonly used optimization algorithms [27, 28]. The particle swarm optimization (PSO) method is another metaheuristic technique that derives its operating principle from the searchability of flocks [29, 30]. Similarly, other metaheuristic algorithms (Firefly, Ant Colony, Artificial Bee, Differential Evolution algorithms, etc.) can be exemplified for different energy applications and control techniques. At present, there is a growing focus on investigating novel and creative optimization techniques, which have been demonstrated to yield more robust, efficient, and precise control performance [31–38].

In our study, Archimedes optimization algorithm (AOA) based pitch angle control is proposed. This algorithm can be controlled by requiring fewer controlling parameters and it enables different convergence phases to optimize the pitch angle controller adaptively.

The main contributions from this paper are listed in the following points:

●The usage of newly introduced algorithms is uncommon for pitch angle control. Studying these algorithms can contribute to studies related to pitch angle control. A comprehensive analysis of the performance of innovative methods for the aforementioned control will inevitably result in the implementation of more reliable and more efficient methods for the regulation of pitch angle.

●Using an activation structure enables pitch angle control at higher wind speeds. Below the rated wind speed, the control system is deactivated to enable maximum efficiency. In this way, different control structures can be used for a WECS at changing wind speeds.

The rest of this study is organized as follows. Section 2 explains basic modeling principles, operating regions of a WECS, and pitch angle control. Section 3 describes the principle of the proposed AOA and its usage for pitch angle control. Simulation results of the proposed method based on variable wind speeds are given in Section 4. The conclusions are given in the last section.

2. Materials and Methods

The main configuration for a WECS includes a wind turbine, a generator, and different types of drivetrains. In addition to these, appropriate control units are integrated into the overall system. The produced energy can be used for both standalone and grid-connected applications. The basic conversion scheme for a WECS is shown in Figure 1.
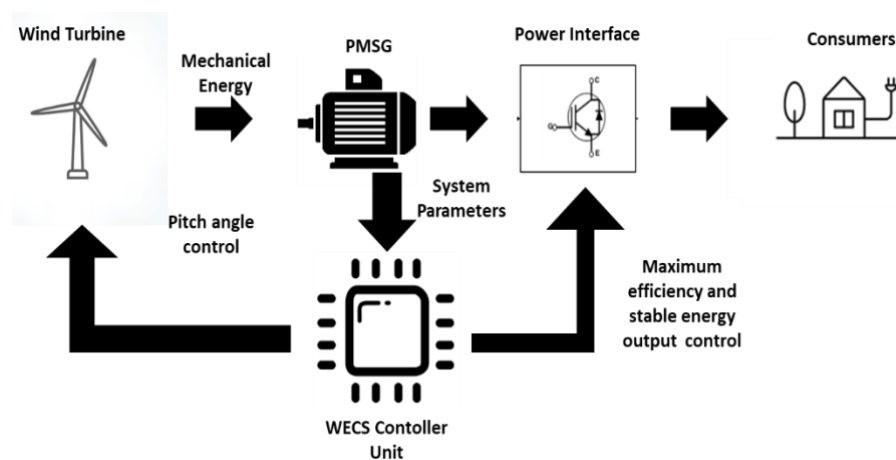
Figure 1. The conversion scheme of a WECS.

In Figure 1, the WECS converts the kinetic energy of the wind into mechanical energy via the wind turbine, and then into electrical energy through the electric generator. The power interface is responsible for the efficiency and stability controls of energy production. All these controls are implemented through this interface using different controller designs. Pitch angle control is applied to the turbine blades through hydraulic or electromechanical actuators. To understand pitch angle control, mathematical models are essential for grasping the fundamental principles of energy conversion in wind energy systems. The power captured by a wind turbine from flowing wind is expressed as shown in Equation (1).

$$P = \frac{1}{2} \times C_P \times p \times A \times V_W{}^3 \tag{1}$$

In Equation (1), P is the extracted mechanical power from the wind (W or J/s), ρ is the air density, which can be defined as a constant equal to 1.225 kg/m³, V_W is the wind speed and A is the swept area by turbine blades (m²), C_P (power coefficient) is defined as the energy conversion efficiency and it is a function of tip speed ratio (TSR) (λ) and pitch angle (β) defined in Equation (2).

$$C_P(\lambda, \beta) = C_1 \left(\frac{C_2}{\lambda_i} - C_3 \times \beta - C_4 \right) e^{-(C_5/\lambda_i)} + C_6 \times \lambda \tag{2}$$

Where $C_{(1-6)}$ are characteristic design values for wind turbines TSR (λ) and λi values can be expressed as in Equation (3).

$$\lambda = \frac{w \times R}{V_W}, \quad \frac{1}{\lambda_i} = \frac{1}{\lambda + 0.08\beta} - \frac{0.035}{\beta^3 + 1} \tag{3}$$

In equation (3), R is the radius of the swept area by the wind turbine and ω represents the mechanical speed of the turbine in rad/s [39]. Figure 2 shows the relationship between the C_P and the TSR for different β values.
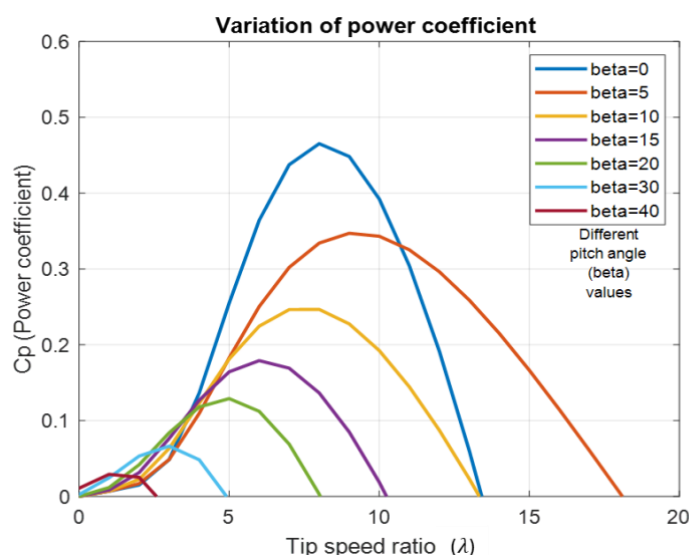
Figure 2. The variation curve of Cp with TSR and pitch angle.

In Figure 2, the relationship demonstrates that the maximum values of C_P are achieved at optimal values of TSR. These optimal values can be obtained using a speed controller for WECS, as described by Equations (2–3). In practice, C_P can reach a maximum value within the range of 0.4–0.5. This indicates that the produced mechanical power is less than 50% of the instant wind power [40]. Another feature shown in Figure 2 is that the power coefficient can be adjusted by increasing the value of the pitch angle to limit the instant power at higher wind speeds.

2.1. Pitch angle control

The pitch angle control is implemented by adjusting blade angles around their longitude axes [41]. The pitch angle controller system is a crucial and effective component for improving the efficiency of wind energy conversion systems and enhancing the stability of output power. Its variable mode of

operation also helps reduce the impact of fluctuating natural conditions, which can otherwise place excessive stress on mechanical components [42]. The implementation of pitch angle variation is shown in Figure 3.

Figure 3. The implementation of pitch angle [41].

Pitch control is categorized into two types. The first is individual pitch control (IPC), which allows for independent adjustment of each blade's pitch angle. IPC utilizes an electromechanical actuator to manage the blade pitch. These systems consist of an electric motor, a gearbox, a power supply unit, and an energy storage system. The second is collective pitch control (CPC), where all blades are set to the same pitch angle and hydraulic actuators are used to control all the blades simultaneously. CPCs offer key advantages, including low complexity and safer operation. On the other hand, IPCs are more efficient and exhibit faster response times compared to hydraulic controllers. However, their power-to-mass ratio is lower. Despite this, IPCs are often preferred due to their lower maintenance and operational costs [28]. With the increasing size of wind turbines, the impact of wind shear, air density variations, and extreme wind turbulence has become more pronounced. This phenomenon intensifies the cyclic loads on turbine blades, which can lead to fatigue, reduced efficiency, and shortened system lifetime. As a result, IPC has gained significant attention, as it can mitigate cyclic loads by independently adjusting the pitch angle of each blade [43]. The IPC principle is applicable for variable-speed wind turbines. Aerodynamic stall controls, which turn the blades into the wind to induce stall, are typically applied to fixed-speed wind turbines [40, 41]. Pitch angle control principle can be explained in the operating regions of a WECS shown in Figure 4.
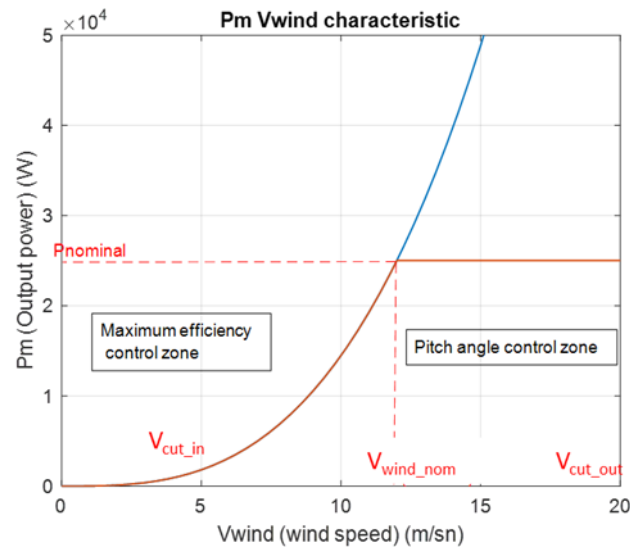
Figure 4. The operating regions of a WECS.

The captured mechanical power is proportional to the cube of the wind speed. This variation is illustrated by the blue curve in Figure 4. Three wind speed values define the boundaries of these operating regions: the cut-in wind speed (V_{cut_in}), the nominal wind speed (V_{wind_nom}), and the cut-out wind speed (V_{cut_out}). When the wind speed is lower than V_{cut_in}, the WECS is in a standstill state. Between V_{cut_in} and V_{wind_nom}, the system operates in the maximum efficiency zone, where the primary objective of the WECS control is to maximize energy efficiency for the prevailing wind speeds [44]. Above the nominal wind speed, the principal control objective shifts to limiting the output power to the rated value to ensure safe operation, improve stability, and maintain optimal power production. If the wind speed surpasses V_{cut_out}, the WECS is stopped to prevent damage [45, 46].

2.2. Archimedes optimization algorithm (AOA)

The proposed algorithm works based on the phenomenon explained by Archimedes' law of physics. This principle is concerned with an object that is either fully or partially submerged in a fluid. The fluid applies an upward force on the object which equals the magnitude of the fluid weight displaced by the object. [47, 48]. The immersed objects represent the optimization population. The AOA search process starts with the initial population. At first, each object is randomly located and has randomly assigned volumes, densities, and accelerations in fluid [47]. Like other metaheuristic algorithms, AOA updates the accelerations and positions of each object. until the termination criteria are satisfied.

AOA consists of both exploration and exploitation processes. The initialization process of all objects is defined in Equation (4).

$$O_i = l_i + rnd \times (u_i \times l_i), i = 1 \dots n \tag{4}$$

Where l_i and u_i are the boundaries of the ith object, and n represents the object number. The volume (*vol*) and density of each object (*den*) can be expressed as shown in Equation (5).

$$den_i = rnd, \ vol_i = rnd \tag{5}$$

Where rnd represents a D-dimension vector within range [0, 1]. Each object acceleration (*acc*) can be expressed as in Equation (6).

$$acc_i = lb_i + rnd \times (ub_i \times lb_i) \tag{6}$$

lb_i and ub_i represent lower and upper boundaries of the search space, respectively. The object with the best position (x^{best},), the best volume (vol^{best}), the best density (den^{best}), and the best acceleration (acc^{best}) are determined based on a fitness function. Their values are recorded as best values for each iteration. Each object's density and volume can be updated as in Equation (7).

$$den_i^{t+1} = den_i^t + rnd2 \times (den^{best} \times den_i^t) \tag{7}$$
$$vol_i^{t+1} = vol_i^t + rnd2 \times (vol^{best} \times vol_i^t)$$

The current and next iterations are expressed as t and $t+1$ respectively. $rnd2$ is a randomly assigned value. In the beginning, there is a collision between the objects until the equilibrium state. This state determines the transition from the exploration stage to the exploitation stage for tracking global optimum faster. The transition operator is defined in Equation (8).

$$TF = exp\left(\frac{t-t_{max}}{t_{max}}\right) \tag{8}$$

Where TF is the transfer operator, t_{max} is the selected maximum iteration number. The operator value is increased gradually at each iteration until a specified unit value. The density factor (d) is another term that is utilized for improving the search process, it can be formulated as in Equation (9).

$$d^{t+1} = exp\left(\frac{t-t_{max}}{t_{max}}\right) - \left(\frac{t}{t_{max}}\right) \tag{9}$$

The d value contributes to the exploration/exploitation balance. The collision between the objects occurs in the exploration phase, the TF value could be taken as a number between 0 and 1 for the threshold value of the two stages. The acceleration of the ith object at the next iteration is updated by using a random object (ro) defined as in Equation (10).

$$acc_i^{t+1} = \left(\frac{den_{ro}+vol_{ro}\times acc_{ro}}{den_i^{t+1}\times vol_i^{t+1}}\right) \tag{10}$$

Where den_{ro}, vol_{ro}, and acc_{ro} represent density, volume, and acceleration values for the random object. When the TF value exceeds the selected number, the exploitation phase represents the equilibrium state between the objects. The acceleration of the ith object in this stage is defined as in Equation (11).

$$acc_i^{t+1} = \left(\frac{den_{best}+vol_{best}\times acc_{best}}{den_i^{t+1}\times vol_i^{t+1}}\right) \tag{11}$$

For both stages and each iteration, the acceleration process is adjusted adaptively. If the object is not close to the best solution, the acceleration change will be larger or vice versa. Furthermore, a normalization parameter prevents the local solution stagnation [47, 48]. This parameter is defined in Equation (12).

$$acc_{i-nom}^{t+1} = u \times \left(\frac{acc_i^{t+1}+min(acc)}{(acc)-(acc)}\right) + l \tag{12}$$

157

In Equation (12), l and u are the normalization edge values, they are selected within the range [0,1]. i-nom represents normalized value for the *ith* object at the t+1 iteration. For the exploration stage, the position of the *ith* object (x) is updated through the iterations as in Equation (13).

$$x_i^{t+1} = x_i^t + C1 \times rnd \times acc_{i-nom}^{t+1} \times d \times (x_{rnd} - x_i^t)$$ (13)

The position updating of objects in the exploitation stage is expressed in Equation (14).

$$x_i^{t+1} = x_i^t + F \times C2 \times rnd \times acc_{i-nom}^{t+1} \times d \times (T \times x_{best} \times x_i^t)$$ (14)

In Equations (13)-(14), $C1$ and $C2$ values are determined in the range [0,10]. T is a parameter value $(T = C3 \times TF)$ based on T increasing within the range $[C3 \times 0.3, 1]$ and, it takes a certain percentage from the best position through the iterations. As the search process continues, the percentage of adjustment applied to the current position gradually increases. This mechanism effectively reduces the disparity between the best-known position and the current position. A constant defined as flag value $(F=2)$, defined by user, is utilized to change the movement direction of the objects. The application flowchart of the Archimedes optimization algorithm is given in Fig. 5.
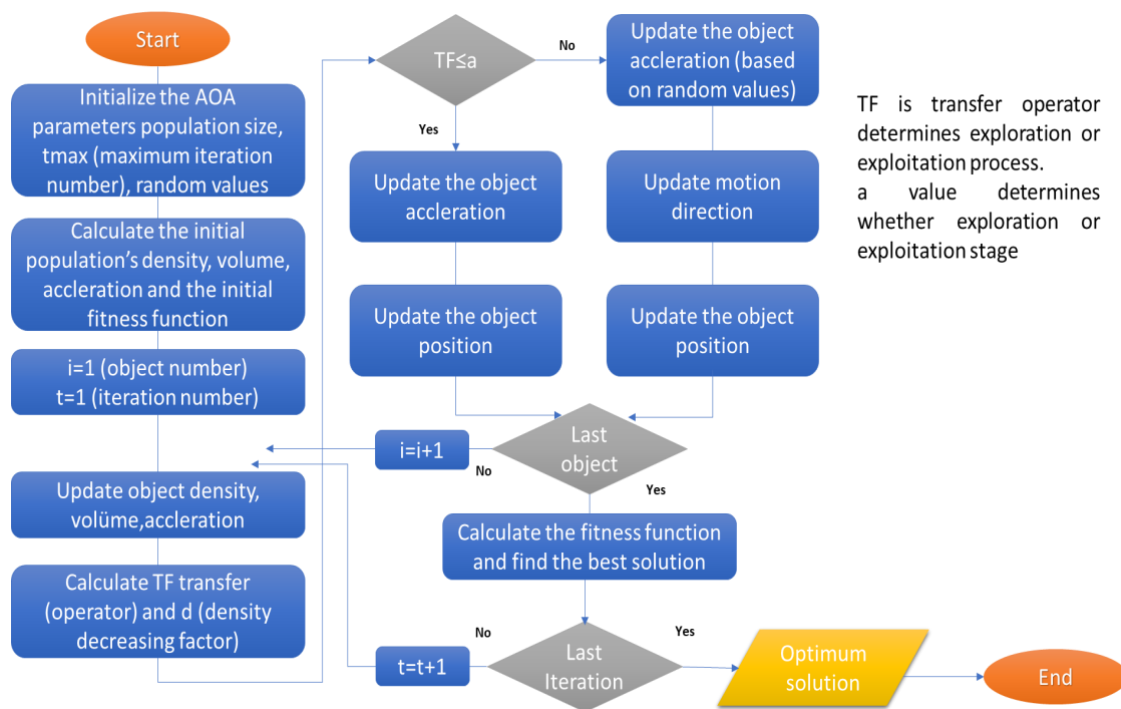
Figure 5. The flowchart of AOA.

3. Results and Discussion

Designing an AOA-based pitch angle control for a WECS is formulated as an optimization problem. The primary criterion used for evaluating the performance of the optimization method is the fitness function. The fitness function for this study aims to minimize the power error between the instant and nominal mechanical output powers. The control adjusts angle values within the range of [0°, 45°]

to limit the instant output power. These values are implemented as objects for the optimization algorithm. The control structure is activated at higher speeds than the rated wind speed. Conversely, at lower speeds, the angle values are adjusted to a minimum to maximize efficiency. The application flowchart of the AOA-based pitch angle controller is illustrated in Figure 6.
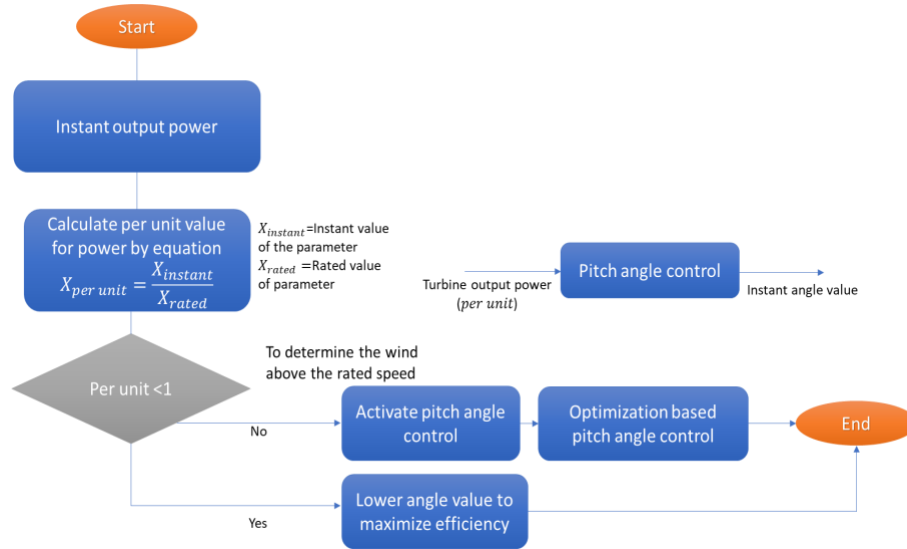
Figure 6. Application steps of pitch angle controller.

In Figure 6, the instant output power is used as an input variable in the control application. This value is calculated as a per-unit value (p.u). The calculation for $p.u$ values is calculated as in Equation (15).

$$X_{p.u.} = \left(\frac{X_{instant}}{X_{rated.}}\right) \tag{15}$$

In Equation (15), where X represents a control parameter of a WECS. This value can be electrical or mechanical parameters. In this study turbine output power was utilized. Reference power value was defined as 1 $p.u$ the utilization of per unit values simplifies the controller and controller-related calculations. The instant angle value can be applied to the wind turbine through actuators. The wind turbine simulation model through MATLAB/Simulink is shown in Figure 7.
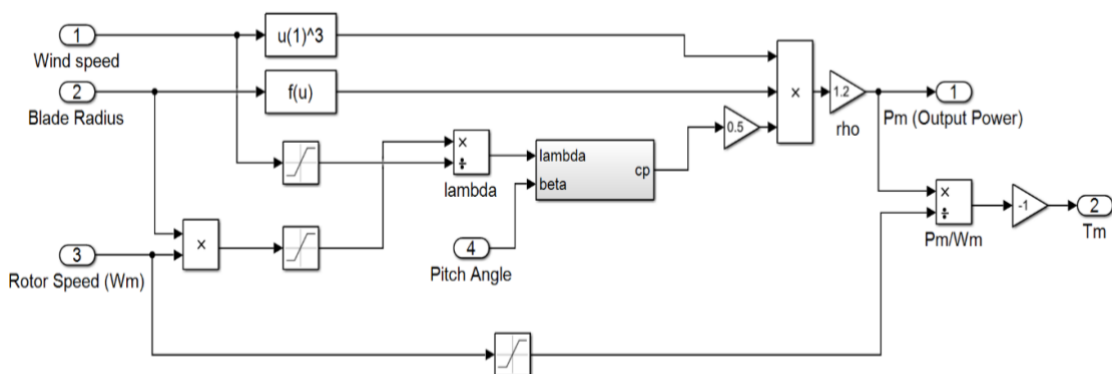
Figure 7. The Simulink model of the wind turbine.

In Figure 7, the wind turbine model was designed based on the mathematical functions of the output power, C_P, and TSR. The angle value was adjusted between 0°-45° values.

For evaluating the AOA-based controller performance, the algorithm has been designed by using a maximum number of iterations that reaches 500 iterations and the population size has been set to 50. To test the AOA-based control, simulations were carried out by using the WECS and optimization parameters, listed in Table I.

Table 1. WECS and optimization parameters

Parameters	Values
Rated Power ($P_{nominal}$)	25 kW
Rated Wind Speed ($V_{wind\ nominal}$)	12 m/s
The area radius by wind turbine (R)	4 m
Air density (p)	1.2 kg/m3
Population (Objects) size	20
t_{max} (Maximum iteration number)	500
a (preselected value for the algorithm)	0.5
(Constant values for optimization)	C1:2 C2:5 C3:4

The rated (nominal) wind speed was defined as 12 m/s in the simulation process. The wind speed patterns for rated and instant wind speed are given in Figure 8.
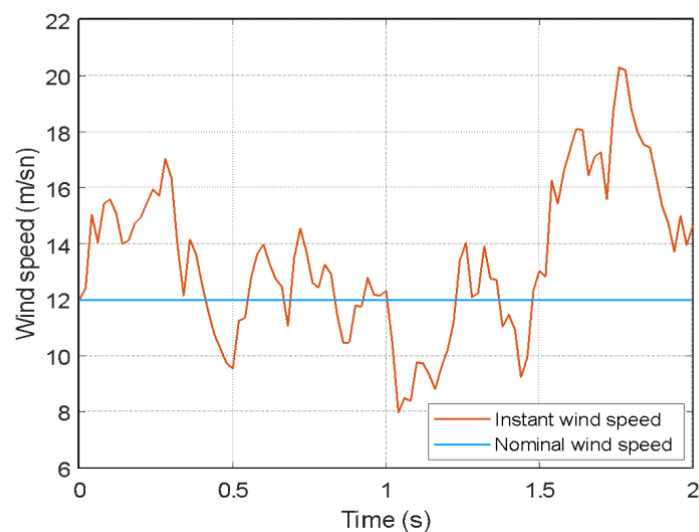
Figure 8. Wind speed patterns for simulation.

The instant wind speed (the orange curve) varies between 8 and 20 m/s in Figure 8. These wind patterns play a crucial role in simulating pitch angle control within wind energy conversion systems, ensuring adaptation to rapidly changing wind conditions. Based on the instant wind speed, the instant angle variation is shown in Figure 9.
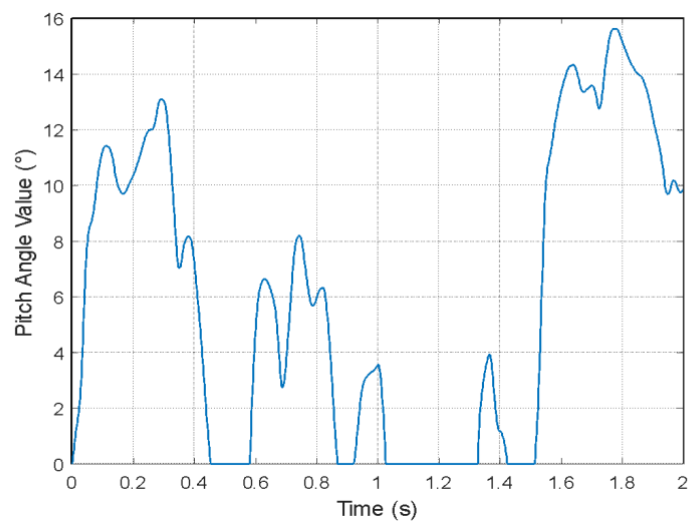
Figure 9. Pitch angle variation of the WECS.

In Figure 9, below the rated speed, the angle value is adjusted at a minimum value (0°) to keep the efficiency value (C_P) at the optimum value for maximum efficiency. When the wind speed exceeds the rated speed (12 m/s), the controller will activate the control and increase the angle value to keep the output power within the rated power limits. The angle value was adjusted by the control in the range [0°-16°]. Minimum oscillated angle variations in all wind speeds proved the remarkable performance of the AOA method. Furthermore, Fast response and compatible variation of angle values showed the high performance of the proposed controller.

The influence of pitch angle control is not illustrated only through the angle variation. The control performance can also be analyzed by assessing the other parameters of the WECS. The power coefficient (C_P) value variation is shown in Figure 10.
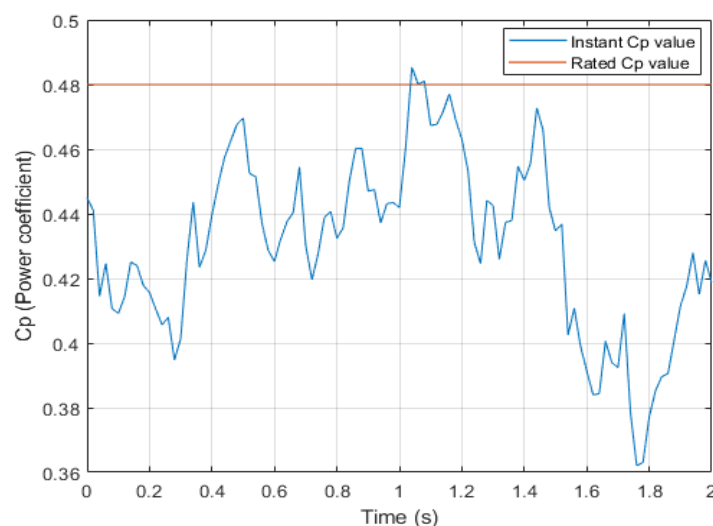
Figure 10. C_P variation of the WECS.

In Figure 10., As mentioned earlier, the obtained pitch angle value by AOA decreased the Cp value to balance the instant output power of the WECS at higher wind speed levels. The angle value was

decreased to increase the power coefficient and WECS efficiency at lower wind speeds. The instant power variation of the WECS is shown in Figure 11.
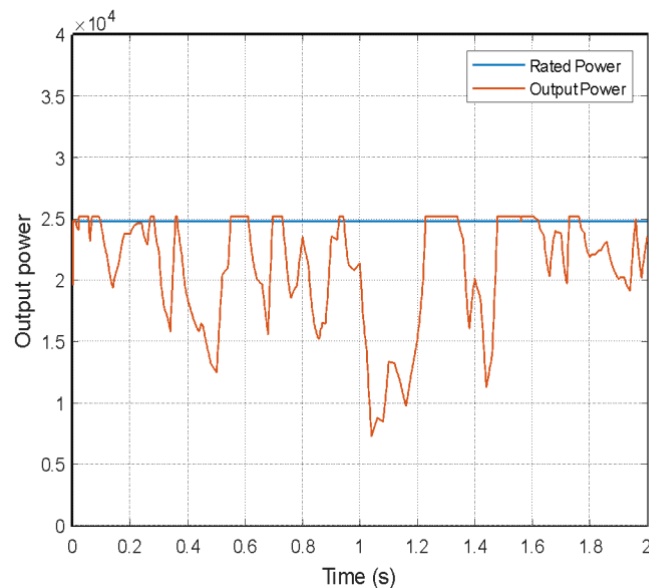
Figure 11. Output power variation of the WECS.

In Figure 11, the extracted mechanical power with AOA based algorithm tracks the rated power curve at higher wind speeds. For lower values, the output power changes in line with variations in wind speed and achieves a highly efficient performance. The proposed controller increased the capacity factor of the wind turbine by enabling it to work at rated limits for higher wind speeds Therefore it can lower the cost per kWh of electricity production.

Except for the comparison with rated values, the proposed algorithm can be compared with other conventional methods used for pitch angle control. For different studies mentioned in the literature. The comparison table for the different pitch angle controls is given in Table 2.

Table 2. The comparison table for the different methods.

Methods	Comparison Criteria			
	Controller efficiency	**Convergence speed**	**Complexity**	**Accuracy**
The proposed AOA method	High	High	Medium	>%90
FLC [21]	High	Medium	High	%70-%90
PID controller [15]	Low	Low	Low	<%50
P&O, INC etc. [8]	Medium	Medium	Low	%60-%80

According to Table 2, the proposed method outperformed the other methods. The metaheuristic principle provided high efficiency and fast-tracking features for the proposed method. The accuracy value reflects the stability and performance level of the controller. A higher accuracy value signifies greater stability and superior performance. The proposed method achieved higher accuracy compared to other methods Another key benefit of the proposed method is that it does not necessitate expertise in the field of expert systems., as required for the FLC method, which reduces its complexity. Conventional PID-based controllers operate based on the adjustment of controller gains. However, the proper

162

adjustment of gains and the reliance on additional tools lower the performance and response speed of the controller, particularly during fast wind speed variations. The perturb and observe (P&O) or incremental conductance (INC) methods operate by iteratively adjusting the controller. At each iteration, the controller output is modified through constant or adaptive steps based on the variations. Although these methods are less complex, their convergence for fast variations and the magnitude and speed of controller adjustments reduce overall efficiency.

4. Conclusion

In this study, an AOA-based pitch angle control for a WECS has been proposed to limit the output power to a desirable level. The working principle of this algorithm is based on Archimedes' law. The control structure was evaluated through simulations in the MATLAB/Simulink environment. The results demonstrate that the proposed controller effectively limits the instant output power to the rated limit for wind speeds above the rated value. Faster and stable control of the pitch angle protects the WECS from higher wind speeds, ultimately increasing the system's lifespan and overall energy output. Furthermore, the control reduces the operation and maintenance expenses of WECSs. AOA-based pitch angle controllers perform well for nonlinear systems and can operate independently of system dynamics and external conditions. For the studied WECS, the proposed control provided a faster response to rapidly changing wind speeds and reduced oscillations around the rated values at higher wind speeds. For future studies, different metaheuristic algorithms can be explored to design alternative control structures for WECSs. These can then be evaluated and compared with the proposed algorithm.

Ethical statement

The author declares that this document does not require ethics committee approval or any special Permission

Conflict of interest

The author declares no conflict of interest.

Authors' Contributions

H. B. Percin: Conceptualization, Methodology, Writing-original draft, Writing - review & editing
A. Caliskan: Supervision, Methodology, Writing - review & editing

References

[1] Yakob Kiros Teklehaimanot, F. K. Akingbade, B. C. Ubochi, and T. O. Ale, "A review and comparative analysis of maximum power point tracking control algorithms for wind energy conversion systems," *International Journal of Dynamics and Control*, vol. 12, no. 9, pp. 3494–3516, May 2024.

[2] Gümüş Bilal, "Integration of Renewable Energy Sources to Power Networks and Smart Grids," Lecture notes in energy, pp. 81–103, Jan. 2022.

[3] Alex, (2024 Nov. 11). "Global Wind Report 2023 - Global Wind Energy Council," Global Wind Energy Council, Feb. 14, 2023. https://gwec.net/globalwindreport2023/.

[4]   Kharchouf I., A. Essadki, M. Fdaili, and T. Nasser, "Comparative Study of MPPT and Pitch Angle using PI and Fuzzy Logic Controllers," 2021 9th International Renewable and Sustainable Energy Conference (IRSEC), 2018.

[5]   Nguyen H. M. and Naidu D. S., "Advanced control strategies for wind energy systems: An overview,", 2011.

[6]   Gajewski P. and Pieńkowski K., "Advanced control of direct-driven PMSG generator in wind turbine system," *Archives of Electrical Engineering*, vol. 65, no. 4, pp. 643–656, 2016.

[7]   Singh N. and Scholar M. T., "Design and Modeling of Wind Energy Conversion System Based on PMSG Using MPPT Technique," vol. 5, no. 2, pp. 96–100, 2016.

[8]   Apata O. and Oyedokun D.T.O., "An overview of control techniques for wind turbine systems," *Scientific African*, vol. 10, pp. e00566–e00566, 2020.

[9]   Elbeji O., Mouna B. hamed, and Lassaad S., "Modeling and control of a variable speed wind turbine," 2014 5th International Renewable Energy Congress (IREC), pp. 1–5, 2014.

[10] Kumar H., Gupta A., Rupendra Kumar Pachauri, and. Chauhan Y. K, "PI/FL based blade pitch angle control for wind turbine used in wind energy conversion system,", 2015.

[11] Wang J., Tse N., and Gao Z., "Synthesis on PI-based pitch controller of large wind turbines generator," *Energy Conversion and Management*, vol. 52, no. 2, pp. 1288–1294, 2011.

[12] Hwas A. and Katebi R., "Wind Turbine Control Using PI Pitch Angle Controller," IFAC Proceedings Volumes, vol. 45, no. 3, pp. 241–246, 2012.

[13] Perçin H.B. and Çalişkan A., "Modeling And Analysis Of Pitch Angle Control On Variable Speed Wind Turbines," *European Journal of Technic*, vol. 11, no. 1, pp. 101–106, 2021.

[14] Muhando, E. B., Senjyu, T., Yona, A., Kinjo, H., & Funabashi, T., Disturbance rejection by dual pitch control and self-tuning regulator for wind turbine generator parametric uncertainty compensation. IET Control Theory and Applications, 1(5), 2007.

[15] Kim J.-S., Jeon J., and Heo H., "Design of adaptive PID for pitch control of large wind turbine generator" , 2011.

[16] Muzakkir Quamar Md, Khan K. A., Liu B., and M. Khalid, "Optimal PID and FOPID Based Pitch Angle Control of Wind Generation System," pp. 1–6, 2023.

[17] Al-Toma, A. S., Taylor, G. A., & Abbod, M., "Intelligent pitch angle control scheme for variable speed wind generator systems", 2017.

[18] Pachauri, R. K., Kumar, H., Gupta, A., & Chauhan, Y. K, "Pitch Angle Controlling of Wind Turbine System Using Proportional-Integral/Fuzzy Logic Controller," *Smart innovation, systems and technologies*, pp. 55–63, 2015.

[19] Chowdhury, M. A., Hosseinzadeh, N., & Shen, W. X., "Smoothing wind power fluctuations by fuzzy logic pitch angle controller," Renewable Energy, vol. 38, no. 1, pp. 224–233, 2011.

[20] Kamel, R. M., Chaouachi, A., & Nagasaka, K., "Enhancement of micro-grid performance during islanding mode using storage batteries and new fuzzy logic pitch angle controller", Energy Conversion and Management, vol. 52, no. 5, pp. 2204–2216, 2011.

[21] Mousa, N. M., El-Shaer, Y. I., & El-Sebah, M. I. A. "A Proposed Controller for Pitch Angle of Wind Turbine", Wseas Transactions On Systems And Control, 18, 527-539, 2023.

[22] Kumar, D., & Chatterjee, K., "A review of conventional and advanced MPPT algorithms for wind energy systems", *Renewable and Sustainable Energy Reviews*, vol. 55, pp. 957–970, 2015.

[23] Tiwari, R., & N, R. B, "Comparative Analysis of Pitch Angle Controller Strategies for PMSG Based Wind Energy Conversion System", *International Journal of Intelligent Systems and Applications*, vol. 9, no. 5, pp. 62–73, 2017.

[24] Yilmaz A. S. and Özer Z., "Pitch angle control in wind turbines above the rated wind speed by multi-layer perceptron and radial basis function neural networks", *Expert Systems with Applications*, vol. 36, no. 6, pp. 9767–9775, 2009.

[25] Asghar A. B., Ehsan R., Naveed K., Al-Ammar E. A., Ejsmont Krzysztof, and Nejman M., "Recurrent neural network for pitch control of variable-speed wind turbine", *Science Progress*, vol. 107, no. 2, 2024.

[26] Hannachi, M., Elbeji, O., Benhamed, M., & Sbita, L., "Comparison between ABC and ACO: Tunning of On-Off MPPT for wind systems", *Wind Engineering*, vol. 45, no. 6, pp. 1601–1612, 2021.

[27] Burakov M., Shishlakov V., "Genetic algorithm optimization for pitch angle control of variable speed wind turbines", MATEC Web of Conferences, vol. 113, pp. 01009–01009, 2017

[28] Tiwari, R., & Babu, N. R., "Recent developments of control strategies for wind energy conversion system", *Renewable and Sustainable Energy Reviews*, vol. 66, pp. 268–285, 2016.

[29] Sudhakar Babu, T., Rajasekar, N., & Sangeetha, K., "Modified Particle Swarm Optimization technique based Maximum Power Point Tracking for uniform and under partial shading condition" , *Applied Soft Computing*, vol. 34, pp. 613–624, 2015.

[30] Seyedmahmoudian, M., Mekhilef, S., Rahmani, R., Yusof, R., & Asghar Shojaei, A., "Maximum power point tracking of partial shaded photovoltaic array using an evolutionary algorithm: A particle swarm optimization technique", *Journal of Renewable and Sustainable Energy*, vol. 6, no. 2, 2014.

[31] V. da, L. P. Sampaio, and S. Augusto, "Comparative Analysis of ABC, Bat, GWO and PSO Algorithms for MPPT in PV Systems," pp. 347–352, 2019.

[32] Mokhtari, Y., & Rekioua, D., "High performance of Maximum Power Point Tracking Using Ant Colony algorithm in wind turbine," *Renewable Energy*, vol. 126, pp. 1055–1063, 2018.

[33] Hetmaniok, E., Słota, D., Zielonka, A., & Wituła, R., "Comparison of ABC and ACO Algorithms Applied for Solving the Inverse Heat Conduction Problem" *Lecture notes in computer science*, pp. 249–257, 2012.

[34] Rahim, A. H. M. A., & Raza, S. A., "A differential evolution based adaptive neural network pitch controller for a doubly fed wind turbine generator system", *Research Journal of Applied Sciences, Engineering and Technology*, *6*(22). 2013.

[35] Karami-Mollaee, A., & Barambones, O., "Pitch Control of Wind Turbine Blades Using Fractional Particle Swarm Optimization," *Axioms*, vol. 12, no. 1, p. 25, 2022.

[36] Ghefiri, K., Bouallegue, S., Haggege, J., Garrido, I., & Garrido, A. J., "Firefly algorithm based-pitch angle control of a tidal stream generator for power limitation mode", *2018 International Conference on Advanced Systems and Electric Technologies (IC_ASET)*, pp. 387–392, 2018.

[37] Lastomo, D., Setiadi, H., & Djalal, M. R., "Optimization pitch angle controller of rocket system using improved differential evolution algorithm", *International Journal of Advances in Intelligent Informatics*, *3*(1), 2017.

[38] Bianchi, F. D., De Battista, H., & Mantz, R. J., *Wind turbine control systems: principles, modelling and gain scheduling design*. Springer Science & Business Media, 2006.

[39] Rolan, A., Luna, A., Vazquez, G., Aguilar, D., & Azevedo, G., "Modeling of a variable speed wind turbine with a Permanent Magnet Synchronous Generator," 2009 IEEE International Symposium on Industrial Electronics, Seoul, Korea (South), , pp. 734-739, 2009.

[40] Zhou, F., & Liu, J., "Pitch Controller Design of Wind Turbine Based on Nonlinear PI/PD Control," *Shock and Vibration*, vol. 2018, no. 1, 2018.

[41] E. José, A. M. Araújo, and S. Bouchonneau, "A review on wind turbine control and its associated methods," *Journal of Cleaner Production*, vol. 174, pp. 945–953, 2017.

[42] Bouregba, H., Hachemi, M., Bey, M., & Hamidat, A., Stability analysis of the pitch angle control of large wind turbines using different controller strategies. *Advances in Mechanical Engineering*,*14*(11), 2022.

[43] Yamada, M., & Murakami, T., "Individual Pitch Control of Wind Turbine System by Estimating Wind Speed Using Pitching Moment". *IEEJ Journal of Industry Applications*, *12*(5), 1008–1014, 2023.

[44] Chen, Z., & Li, H., "Overview of different wind generator systems and their comparisons," *IET Renewable Power Generation*, vol. 2, no. 2, pp. 123–138, 2008.

[45] Ben Smida, M., & Sakly, A., "Pitch angle control for grid-connected variable-speed wind turbine system using fuzzy logic: A comparative study," *Wind Engineering*, vol. 40, no. 6, pp. 528–539, 2016.

[46] Shehata, E. G., "A comparative study of current control schemes for a direct-driven PMSG wind energy generation system," Electric Power Systems Research, vol. 143, pp. 197–205, 2017.

[47] Hashim, F. A., Hussain, K., Houssein, E. H., Mabrouk, M. S., & Al-Atabany, W., "Archimedes optimization algorithm: a new metaheuristic algorithm for solving optimization problems," *Applied Intelligence*, vol. 51, no. 3, pp. 1531–1551, 2021.

[48] Fathy, A., Alharbi, A. G., Alshammari, S., & Hasanien, H. M., "Archimedes optimization algorithm based maximum power point tracker for wind energy generation system," *Ain Shams Engineering Journal*, 2021.

Middle East Journal of Science

Research Article

ADVANCED SKIN CANCER DETECTION USING CONVOLUTIONAL NEURAL NETWORKS AND TRANSFER LEARNING

Emrah ASLAN [ID]*[1], *Yıldırım ÖZÜPAK* [ID][2]

[1]Silvan Vocational School, Dicle University, Diyarbakır, Turkey
[2]Silvan Vocational School, Dicle University, Diyarbakır, Turkey
*Corresponding author: emrah.aslan@dicle.edu.tr

Abstract: *This study investigates the effectiveness of MobileNetV2 transfer learning method and a deep learning based Convolutional Neural Network (CNN) model in the categorization of malignant and benign skin lesions in skin cancer diagnosis. Since skin cancer is a disease that can be cured with early detection but can be fatal if delayed, accurate diagnosis is of great importance. The model was trained with MobileNetV2 architecture and performed the classification task with high accuracy on images of skin lesions. Metrics such as accuracy, recall, precision and F1 score obtained during the training and validation processes support the high performance of the model. The accuracy of the model was 92.97%, Recall 92.71%, Precision 94.70% and F1 score 93.47%. The results show that the CNN-based MobileNetV2 model is a reliable and effective tool for skin cancer diagnosis, but small fluctuations in the validation phase require further data and hyperparameter optimization to further improve the generalization ability of the model. This study demonstrates that CNN-based models enhanced with MobileNetV2 transfer learning offer a powerful solution to medical image classification problems and have the potential to contribute to the development of early detection systems in the healthcare field.*

Keywords*: Skin cancer, CNN, Transfer learning, Classification, MobileNetV2*

1. Introduction

Skin cancer continues to be an important health problem in terms of both incidence and mortality rates worldwide. This disease, which develops under the influence of various environmental and genetic factors, can lead to fatal consequences if not diagnosed early. According to World Health Organization (WHO) statistics, millions of new cases of skin cancer are recorded each year. Skin cancer is mainly divided into two groups: benign lesions and malignant lesions. While benign lesions are usually not life-threatening, malignant lesions, especially aggressive types such as melanoma, can metastasize rapidly and can be fatal. However, the vast majority of skin cancer cases can be effectively treated and life expectancy significantly prolonged when detected early [1].

Traditional methods of skin cancer diagnosis are based on physical examinations by dermatologists and biopsy of suspicious lesions. Although biopsy is an accurate method, it is invasive and often time-consuming. Furthermore, its widespread use is impractical, especially in developing countries and areas with limited health resources. Furthermore, differences in assessment between dermatologists and the risk of human error can create significant variability in the diagnostic process. This clearly highlights the need for faster, cheaper and more objective technologies for skin cancer diagnosis [2].

The use of artificial intelligence and deep learning approaches in medical imaging has expedited efforts to build automated skin cancer diagnosis systems in recent years. Deep learning algorithms have attracted attention with their superior performance, especially in image processing and classification [3]. CNN stand out among deep learning methods and are used as a powerful tool for extracting complex features from medical images. Thanks to its layered structure, CNN can analyze data in detail, starting from low-level features to high-level abstractions. Thanks to these features, it is considered as a promising technology for solving medical problems such as skin cancer [4].

In this study, a CNN-based model is developed to classify benign and malignant skin lesions. The proposed model aims to distinguish between malignant and benign lesions with high accuracy by extracting detailed features from dermatologic images. An open access dermoscopic image dataset is used for training and evaluation of the model. In addition, data augmentation techniques were used to increase the generalization capacity of the model. The main goal of the study is to make skin cancer diagnosis faster and more reliable, as well as to strengthen the decision support processes of expert dermatologists by promoting the use of artificial intelligence in healthcare.

The use of automated systems in skin cancer diagnosis has the potential to increase access to healthcare, especially in low-resource areas. In this context, the proposed model aims to make a significant contribution to the existing literature in the field of dermatology. By evaluating the feasibility and effectiveness of AI-based methods in skin cancer diagnosis, the study provides results that can guide future research. The integration of technology in healthcare is critical for both improving patient outcomes and developing cost-effective solutions. Accordingly, the proposed work represents an innovative approach to skin cancer diagnosis.

2. Literature Review

Murugan et al. developed a computer vision-based system for skin cancer diagnosis. First, skin images were processed with median filter and segmented with Mean Shift segmentation. Features were extracted with GLCM, Moment Invariants and GLRLM methods, and then these features were classified with SVM, Probabilistic Neural Networks and Random Forest classifiers. The best results were obtained with SVM+RF, which is a combination of SVM and Random Forest [5]. Luu et al. proposed a hybrid framework consisting of Stokes-decomposition method and artificial intelligence models. Optical parameters were extracted from skin cancer samples and classification was performed with nine different artificial intelligence models. All models showed high accuracy. This framework provides an efficient and accurate approach for skin cancer classification [6]. Tembhurne et al. proposed a method that combines machine learning and deep learning techniques for skin cancer detection. The deep learning model uses neural networks to extract features from images, while the machine learning model processes these features. The proposed model achieved high accuracy for benign and malignant cancer types [7].

Monika et al. performed classification for early detection of skin cancer using machine learning and image processing methods. Dull razor, Gaussian and Median filters were applied on dermoscopic images and k-means clustering was performed for color analysis. ABCD and GLCM were used for feature extraction and high accuracy was achieved with multi-class SVM [8]. Osvin Nancy et al. evaluated machine learning and deep learning algorithms for early detection by studying the effect of UV rays on skin cancer. Random Forest achieved 58.57% accuracy and 87.32% accuracy with boosting. MobileNetv2 and combination models achieved 88.81% accuracy. The results show that these techniques are promising for clinical applications [9]. Mazhar et al. examined the role of machine learning in improving the diagnostic processes of dermatologists. The paper discusses the basics, limitations and concerns of ML-based applications for skin cancer detection. Deep learning applications are used for disease classification and measurement of skin diseases. In addition, the key elements

required for skin cancer detection and issues such as lesion tracking are emphasized [10]. Gomathi et al. proposed a double optimization based deep learning network (DODL net) for early detection of skin cancer. Dermoscopic images were collected from the MNIST HAM10000 dataset and noise was reduced with an adaptive median filter. After segmentation with U-Net, features were extracted with BFO and PSO and seven skin cancer classes were classified with CNN [11].

Ghosh et al. developed a hybrid model for early detection of skin cancer using deep learning methods with 3,000 images. Class weights were added and VGG16 and ResNet50 were combined to solve the overrepresentation problem. The results show that this model improves the classification performance [12]. Priyadharshini et al. propose a hybrid Extreme Learning Machine (ELM) and Teaching-Learning-Based Optimization (TLBO) algorithm for early detection of melanoma. ELM provides fast and accurate classification, while TLBO optimizes the network parameters. This method aims to improve melanoma detection accuracy by classifying skin lesions as benign or malignant [13]. Balaha and Hassan developed five U-Net models optimized by Sparow Search Algorithm (SpaSA) for early detection of skin cancer. The proposed method is compared with 13 related works [14]. Shah et al. developed automated techniques for early detection of skin cancer using Artificial Neural Networks (ANN) and CNN. The research demonstrates the success of these methods in efficiently detecting skin cancer, highlighting the potential for more effective diagnostic systems. These studies could have a significant impact on improving patient outcomes [15]. In their study, Pacal et al. aim to achieve more efficient and accurate results in skin cancer diagnosis by improving the Swin Transformer architecture. The new model provides faster training times, higher accuracy and better parameter efficiency compared to traditional methods, while outperforming previous deep learning models on the ISIC 2019 dataset [16].

3. Material and Method

CNNs are deep learning models known for their outstanding success in image recognition and classification. CNNs are particularly notable for their ability to extract and classify features from dermoscopic images, especially in the diagnosis and classification of dermatological diseases. CNNs learn low-level features (e.g., edge and texture patterns) from input images and transform these features into more complex and meaningful representations. In skin cancer diagnosis, CNN models can accurately distinguish between different skin conditions such as melanoma, basal cell carcinoma, and benign lesions, with performance comparable to expert dermatologists. This study aims to train CNN on a large dermoscopic dataset using transfer learning methods and to evaluate the performance of the model in terms of accuracy, sensitivity and specificity. In this context, the proposed approach aims to contribute to the development of a reliable and fast tool for automatic skin cancer diagnosis.

In this study, the dataset used for skin cancer diagnosis was obtained from Kaggle (https://www.kaggle.com/datasets/fanconic/skin-cancer-malignant-vs-benign/data), an open access resource. The dataset includes benign and malignant skin cancer types and healthy skin images. This diversity is intended to make the model perform more generally in real-world applications.

3.1. Dataset

The dataset used in this study (https://www.kaggle.com/datasets/fanconic/skin-cancer-malignant-vs-benign/data) contains a balanced set of images to classify benign and malignant skin lesions [17]. The dataset is organized into two separate folders, each containing 1800 images. The images are 224x224 pixels in size and high resolution and provide detailed visual information about benign and malignant skin lesions. The balanced structure of the dataset aims to ensure that the model is equally sensitive to both classes. This structure aims to increase the generalization capacity of the developed model by avoiding biases that may arise from class imbalances. This dataset provides a suitable basis

for the training and testing processes of artificial intelligence and deep learning-based algorithms used in skin cancer diagnosis. Some sample images in the dataset are given in Figure 1.
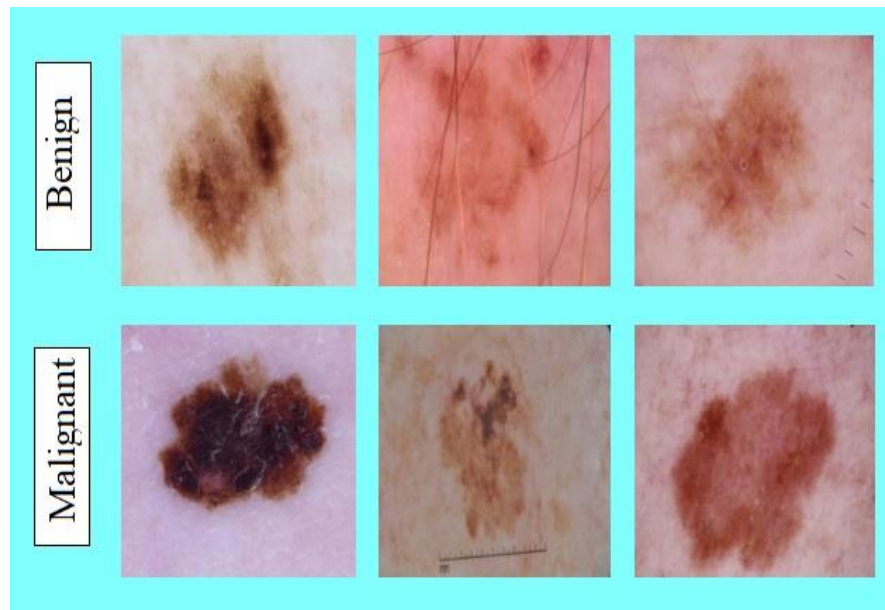
Figure 1. Some sample images from the dataset [17].

3.2. CNN Architecture

The architecture of the model is based on a CNN design optimized for skin cancer diagnosis. The model accepts RGB images of 224x224 pixels in the input layer and then passes through convolutional layers for feature extraction. In the first convolutional layer, 32 filters are used, and 64 and 128 filters are used in the subsequent layers, respectively [18, 19]. All convolutional layers include the ReLU activation function, while Max-Pooling of size 2x2 is applied after each layer to reduce the size of the feature maps. In order to prevent overlearning, the dropout technique was used and 25% of neurons were disabled in certain layers. After convolution, the feature maps were flattened and then transferred to a fully connected layer with 128 neurons. The final classification was carried out on an output layer using the Softmax activation function. For multi-class classification, the model was built employing a cross-entropy loss function and the Adam optimization algorithm, with accuracy serving as the evaluation metric [20, 21]. This architecture is designed to achieve high performance in the classification of skin cancer types by effectively extracting information from low-level features to abstract levels. The CNN structure used is presented in Figure 2.
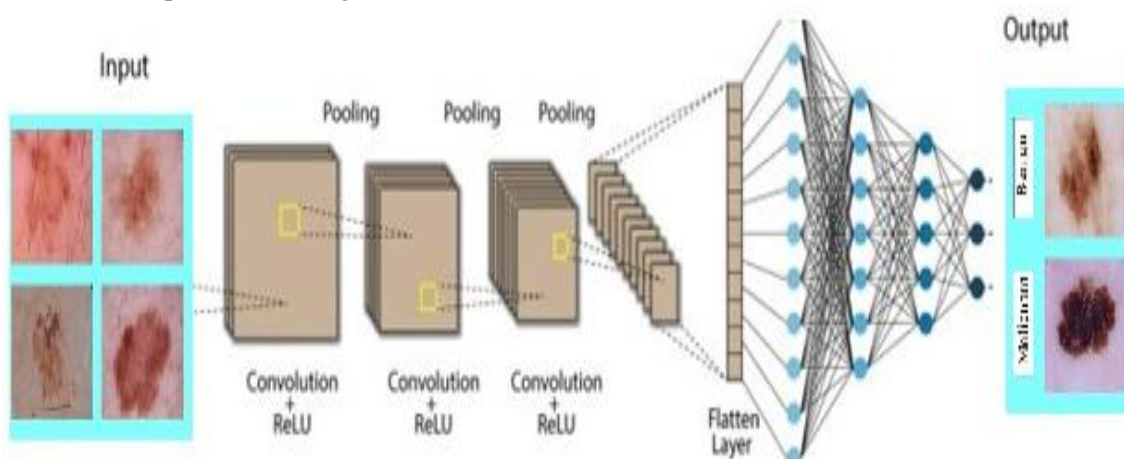
Figure 2. CNN architecture

3.3. Proposed Model

The model proposed in this paper for skin cancer classification is a MobileNetV2-based transfer learning approach that offers a lightweight and computationally efficient architecture. The MobileNetV2 model is a pre-trained deep learning model that can efficiently extract general features on limited datasets and is adapted to the classification task in this study. The input dimensions of the model are set to 160x160 to reduce the computational cost and to preserve the lightweight nature of the model.

In the proposed model, the generalization capability of the model is increased by using data augmentation methods. In the data augmentation phase, zoom, rotation, vertical shift, horizontal shift, and horizontal flip operations were applied on the images. These operations allowed to obtain more variation from a limited number of data sets and reduced the risk of overfitting the model. In the transfer learning process, the lower layers of the MobileNetV2 model (base model) were frozen and only the classifier part in the upper layers was retrained. In this part, a Global Average Pooling layer was added to the feature extractor part of the model, followed by a fully connected (dense) layer with 128 neurons and 40% Dropout to prevent overlearning. In the output layer, a single neuron with a sigmoid activation function was used for binary classification. During the training of the model, the learning rate was set as the learning rate and Binary Crossentropy was used as the loss function. Adam was chosen as the optimization algorithm due to its computational efficiency and fast convergence. Accuracy and validation accuracy metrics were used to measure the training and validation performance. In addition, the performance of the model was also evaluated with Training and Validation Loss (loss and val_loss).

In order to visualize and evaluate the model results, a graphical analysis of the accuracy and loss values was performed and the prediction performance of the model was detailed with a Confusion Matrix. These approaches provided an important tool to highlight the model's strengths and identify its shortcomings in the classification task. Despite its computationally lightweight nature, the proposed model was able to achieve high accuracy values and its performance on the dataset was found to be satisfactory. A visualization of the proposed model is given in Figure 3.

Figure 3. Architecture of the proposed model

3.4. Evaluation Metrics

In this study, the following metrics were used to evaluate the performance of the developed model:

Accuracy: It is a metric that assesses the model's overall success rate and is calculated as the ratio of correctly classified samples to total samples.

Precision: Measures the rate at which the model correctly predicts the positive class. It is particularly important for assessing the impact of false positives.
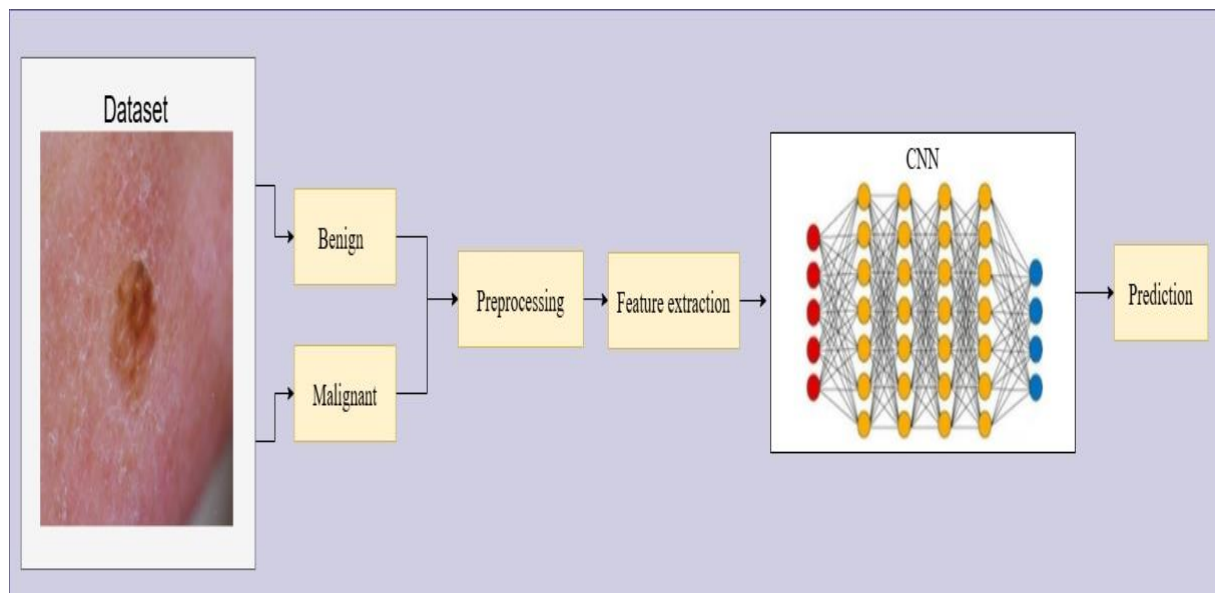
Recall or Detection Rate: Shows how much of the data belonging to the positive class can be correctly detected. It is a critical metric when false negatives are important. It is the harmonic mean showing the balance between precision and sensitivity. It is used to make a balanced assessment.

Confusion Matrix: Tabulates the model's true and false predictions for each class. This matrix provides a more detailed understanding of metrics such as accuracy, precision and sensitivity.

These metrics allow for a comprehensive analysis of both the model's classification success and its errors due to incorrect predictions. The results of the study are compared over different metrics to evaluate the generalization and classification success of the model [23]. The calculation equations for the metrics are given in (1) - (4). In the equation, TP stands for true positive, TN for true negative, FP for false positive and FN for false negative.

$$Accuracy = \frac{TP + TN}{TP + TN + FP + FN} \tag{1}$$

$$Recall = \frac{TN}{TP + FN} \tag{2}$$

$$Precision = \frac{TP}{TP + FP} \tag{3}$$

$$F1 = 2x \frac{Precision \; x \; Recall}{Precision + Recall} \tag{4}$$

4. Experimental Results

In this study, a deep learning-based CNN model was employed to conduct a thorough examination of skin cancer diagnosis. The model was highly accurate in classifying benign and malignant skin lesions and had a significant generalization capacity. In addition to analyzing the accuracy and loss values obtained in the training and validation phases, the classification performance of the model was measured using various evaluation metrics. In this context, metrics such as Accuracy, Recall, Precision and F1 score were calculated to evaluate the overall success and classification ability of the model. The results presented below clearly demonstrate the effectiveness of the model in skin cancer diagnosis.

Table 1. Performance metrics of the proposed model

Accuracy	Recall	Precision	F1 Score
0.9297	0.9271	0.9470	0.9347

Table 1 summarizes the accuracy, recall, precision and F1 score values of the proposed CNN model. The overall accuracy of the model was 92.97%, indicating that the model was able to correctly classify the majority of the data. Recall was 92.71%, reflecting the model's ability to correctly recognize malignant samples, while Precision was 94.70%, indicating a high proportion of true positives. The F1 score was 93.47%, indicating a balanced performance. These metrics clearly show that the model exhibits high accuracy and generalization success in skin cancer diagnosis.

Figure 4 shows the complexity matrix used to evaluate the classification performance of the proposed model. According to the matrix, the model correctly classified 267 benign skin lesions, but incorrectly predicted 21 benign lesions as malignant. Similarly, the model correctly detected 209 malignant lesions, but incorrectly classified 15 malignant lesions as benign. These results show that the model has a high accuracy rate in both benign and malignant classes. However, the presence of false negatives (6.7%) is a critical element that should be treated with caution, especially in the diagnosis of malignant lesions, as this can be life-threatening. The proportion of false positives (7.3%) suggests that the model may need improvement in the precision metrics, as this may lead to unnecessary biopsies or interventions. Overall, the model's correct classification rates are promising, indicating that it can be an effective tool for skin cancer diagnosis. However, considering the impact of misclassifications on health practices, further improvements are recommended to increase the recall and precision of the model.
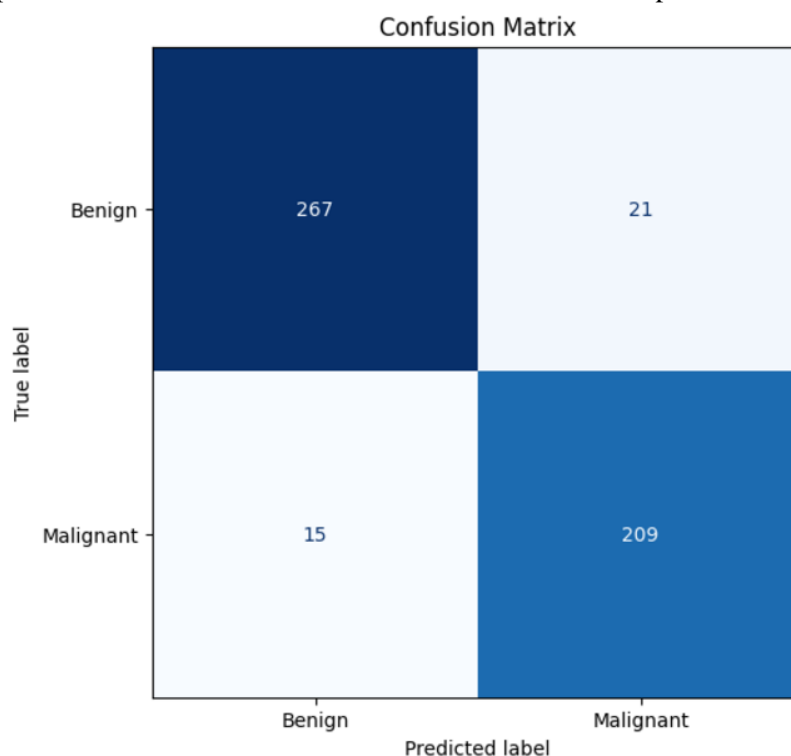
Figure 4. The proposed model's confusion matrix

Figure 5 and Figure 6 comprehensively show the changes in the accuracy and loss values of the model during the training and validation processes depending on the number of epochs. In Figure 5, it can be seen that the training accuracy shows a steady increase at each epoch and exceeds 95% at around epoch 30, reaching a very high accuracy of 99% at epoch 50. The validation accuracy curve follows a similar trend, showing a rapid increase at the beginning and reaching over 90% after the 20th epoch, proving that the generalization performance is strong. The parallel increase in the training and validation accuracy curves shows that the model is able to avoid the overfitting problem and performs a balanced learning.

Figure 6 shows the changes in the training and validation losses of the model. The training loss curve starts with a high value of 0.9 at the beginning but decreases steadily to 0.2 at the end of the 50th epoch. This clearly shows that the model learns correctly on the training data. The validation loss curve similarly decreased in parallel with the training loss and stabilized at around 0.3. This decrease in the validation loss indicates that the generalization ability of the model is strong. However, the small

fluctuations observed in the validation loss and accuracy curves may be due to variation in the validation data or the model's inability to fully adapt to the validation data across epochs.
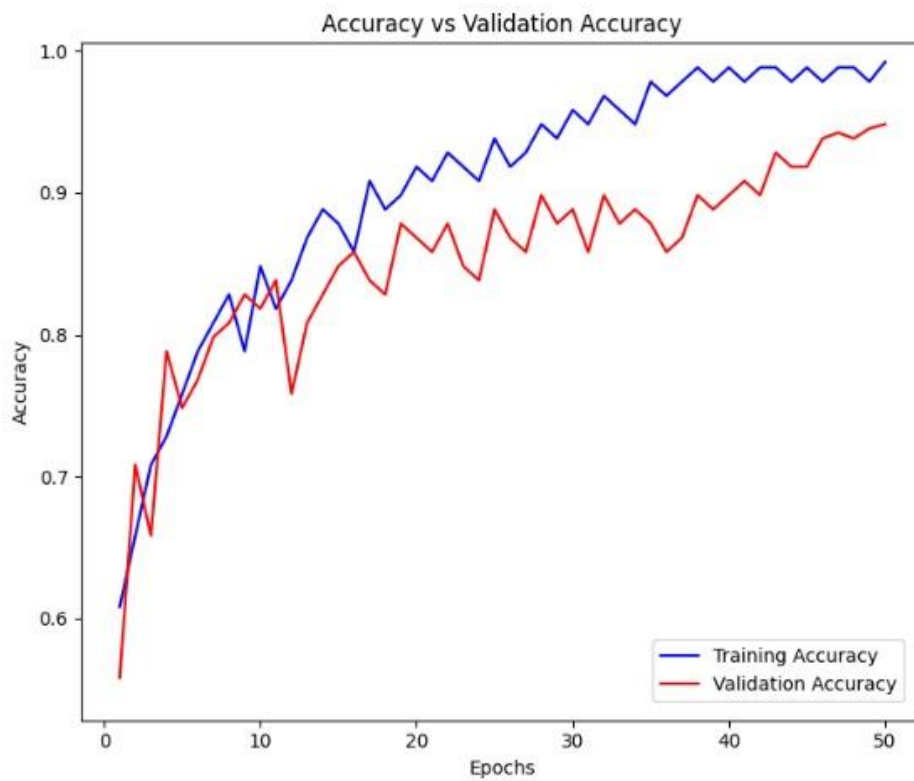
Figure 5. Validation and test accuracy of the model
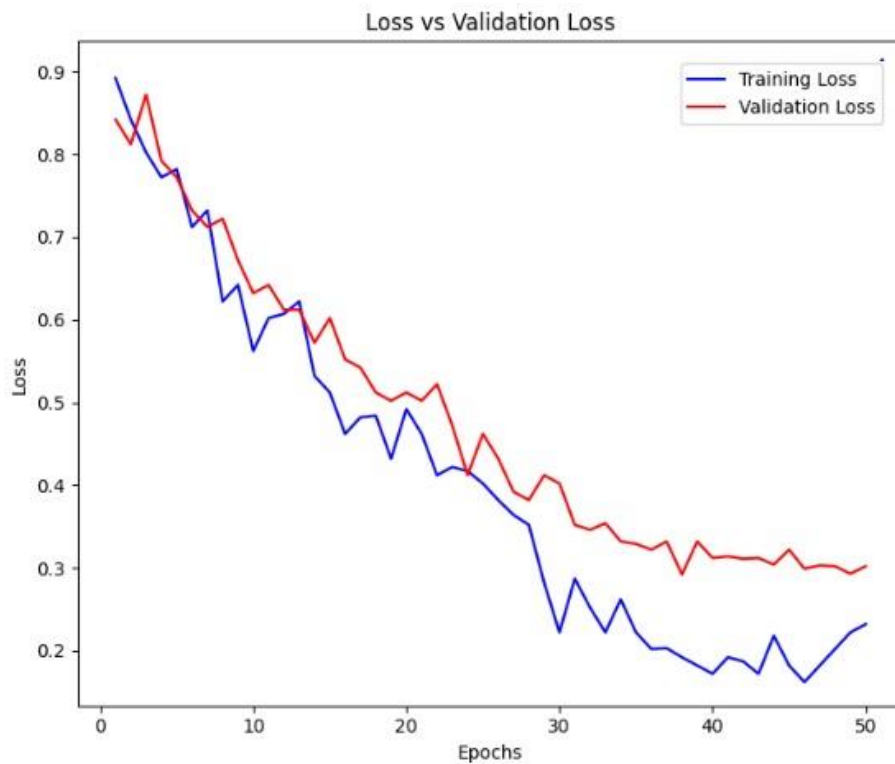
Figure 6. Loss curve of the model

In general, both the accuracy and loss curves are parallel and balanced, indicating that the model provides an effective result in terms of both learning and generalization performance. However, training with more data or applying hyperparameter optimization may be recommended to reduce the fluctuations in the validation loss and further improve the model performance. This analysis clearly demonstrates that the model can be used as a powerful and reliable classification tool for skin cancer diagnosis. In Table 2, the results obtained are compared with the results of some studies in the literature.

Table 2. Comparison of the results of the proposed model with the literature

Study	Classification	Model	Dataset	Accuracy (%)
[18]	Benign/malignant	CNN	ISIC	89.5
[19]	Benign/malignant	LightNet	ISIC	81.6
[20]	Malignant melanoma/SK	SVM	ISIC	90.69
[21]	Melanoma/SK	Deep multi-scale CNN	ISIC	90.3
[22]	Benign/malignant	CNN-DensNet169	ISIC	92.25
Proposed Model	Benign/malignant	CNN-MobileNetV2	ISIC	92.97

Table 2 presents the accuracy of the CNN-MobileNetV2 model proposed in this study in comparison with other models in the existing literature. The table shows in detail the methods, datasets and accuracy rates obtained in different studies. In [18], a CNN model was used on the ISIC dataset to classify benign and malignant lesions and achieved 89.5% accuracy. In [19], the LightNet model, a lighter architecture, was used, but the accuracy was limited to 81.6%. This shows that the generalization capacity of lighter architectures may be limited.

In [20], the SVM model was used to classify malignant melanoma and seborrheic keratosis with an accuracy of 90.69%. This result proves that machine learning-based methods can also show high performance. In [21], melanoma and SK classification was performed with the Deep Multi-Scale CNN model and an accuracy rate of 90.3% was obtained. This model was able to improve classification performance by working with deeper structures. In [22], benign and malignant lesions were classified with the CNN-DensNet169 model and an accuracy rate of 92.25% was obtained. This model demonstrated high performance by working with a more complex CNN architecture.

The proposed CNN-MobileNetV2 model showed the highest performance with an accuracy of 92.97% on the ISIC dataset. The model achieved better results by using an effective combination of transfer learning method and data augmentation strategies. Moreover, its lighter architecture reduced the computational cost and resulted in faster classification. The comparison in Table 2 clearly shows that the proposed model outperforms the methods in the existing literature and improves the classification success rate. These results show that the proposed model provides a powerful solution in terms of both accuracy and practicality.

The methods used in this study offer several advantages but also have some limitations. The proposed model achieved high metrics such as accuracy (92.97%) and F1 score (93.47%), indicating that malignant and benign lesions can be classified reliably. The MobileNetV2-based transfer learning method provided high performance with limited data and offered a fast solution with low hardware requirements. Moreover, the use of a balanced and diversified dataset enhanced the generalization capability of the model, which strengthens its application potential, especially in regions with limited health resources.

However, the small fluctuations observed during the validation phase and the 6.7% of false negative classifications reveal aspects of the model that need improvement. The generalizability of the model can be improved with larger and more diverse datasets. Moreover, the lack of hyperparameter optimization is another factor limiting the model performance. The fact that the dataset used does not

fully represent geographic and demographic diversity may also be a limiting factor in real-world applications.

In the future, hyperparameter optimization and the use of larger data sets are recommended to improve the performance of the model. In addition, developing hybrid models and testing the model in clinical settings can improve both the classification success and the practical application value. While this study proves to be an effective classification tool with its current results, it also has room for improvement.

5. Conclusion

In this study, a deep learning-based CNN model is used to classify malignant and benign types of skin cancer and the results are evaluated. The model successfully demonstrated both its learning and generalization capabilities by performing consistently in the training and validation processes. The experimental results show that the model is an effective classification tool for skin cancer diagnosis with 92.97% accuracy, 92.71% recall, 94.70% precision and 93.47% F1 score. These findings prove that CNN models offer a reliable approach to complex medical image classification problems and can support skin cancer diagnosis processes. However, the small fluctuations observed during the validation phase may require the use of larger and diverse datasets or hyperparameter optimization to further improve the performance of the model. In future studies, the application of transfer learning techniques, different data augmentation strategies and hybrid models can be evaluated to improve the performance of the model. These results show that the proposed model can be used not only in skin cancer diagnosis but also in other medical image classification applications. The proposed approach has the potential to make a significant impact in the healthcare sector by contributing to early diagnosis and treatment processes. CNNs are deep learning models known for their outstanding success in image recognition and classification.

Ethical statement

Our study does not cause any harm to the environment and does not involve the use of animal or human subjects. Therefore, it was not necessary to obtain an Ethics Committee Report.

Conflict of interest

The author declares no conflict of interest.

Authors' Contributions

E. A: Methodology, Software, Investigation, Writing - Original draft preparation (%50)
Y. Ö: Methodology, Resources, Investigation, Writing - Original draft preparation (%50).
All authors read and approved the final manuscript.

References

[1] Naqvi, M., Gilani, S. Q., Syed, T., Marques, O., Kim, H., "Skin Cancer Detection Using Deep Learning-A Review", *Diagnostics*, 13(11), 1911, 2022. doi: 10.3390/diagnostics13111911.

[2] Vidya, M., Karki, M. V., "Skin Cancer Detection using Machine Learning Techniques", in: *Proc. IEEE Int. Conf. Electronics, Computing and Communication Technologies (CONECCT)*, Bangalore, India, 2020, pp. 1-5. doi: 10.1109/CONECCT50063.2020.9198489.

[3]   Daghrir, J., Tlig, L., Bouchouicha, M., Sayadi, M., "Melanoma Skin Cancer Detection Using Deep Learning and Classical Machine Learning Techniques: A Hybrid Approach", in: *Proc. 5th Int. Conf. Advanced Technologies for Signal and Image Processing (ATSIP)*, Sousse, Tunisia, 2020, pp. 1-5. doi: 10.1109/ATSIP49331.2020.9231544.

[4] Bayram, M., Arserim, M. A., "Analysis of Epileptic iEEG Data by Applying Convolutional Neural Networks to Low-Frequency Scalograms," in IEEE Access, vol. 9, pp. 162520-162529, 2021. doi: 10.1109/ACCESS.2021.3132128.

[5] Murugan, A., Nair, S. A. H., Peace Preethi, A. A., Sanal Kumar, K. P., "Diagnosis of Skin Cancer Using Machine Learning Techniques", *Microprocessors and Microsystems*, 81, 103727, 2021. doi: 10.1016/j.micpro.2020.103727.

[6] Luu, T. N., Phan, Q. H., Le, T. H., Pham, T. T. H., "Classification of Human Skin Cancer Using Stokes-Mueller Decomposition Method and Artificial Intelligence Models", *Optik*, 249, 168239, 2022. doi: 10.1016/j.ijleo.2021.168239.

[7] Tembhurne, J. V., Hebbar, N., Patil, H. Y., et al., "Skin Cancer Detection Using Ensemble of Machine Learning and Deep Learning Techniques", *Multimedia Tools and Applications*, 82, 27501–27524, 2023. doi: 10.1007/s11042-023-14697-3.

[8] Monika, M. K., Vignesh, N. A., Kumari, C. U., Kumar, M. N. V. S. S., Lydia, E. L., "Skin Cancer Detection and Classification Using Machine Learning", *Materials Today: Proceedings*, 33(7), 4266-4270, 2020. doi: 10.1016/j.matpr.2020.07.366.

[9] Nancy, N. V. A. O., Prabhavathy, P., Arya, M. S., et al., "Comparative Study and Analysis on Skin Cancer Detection Using Machine Learning and Deep Learning Algorithms", *Multimedia Tools and Applications*, 82, 45913–45957, 2023. doi: 10.1007/s11042-023-16422-6.

[10] Mazhar, T., Haq, I., Ditta, A., Mohsan, S. A. H., Rehman, F., Zafar, I., Gansau, J. A., Goh, L. P. W., "The Role of Machine Learning and Deep Learning Approaches for the Detection of Skin Cancer", *Healthcare*, 11, 415, 2023. doi: 10.3390/healthcare11030415.

[11] Gomathi, E., Jayasheela, M., Thamarai, M., Geetha, M., "Skin Cancer Detection Using Dual Optimization-Based Deep Learning Network", *Biomedical Signal Processing and Control*, 84, 104968, 2023. doi: 10.1016/j.bspc.2023.104968.

[12] Ghosh, H., Rahat, I. S., Mohanty, S. N., Ravindra, J. V. R., Sobur, A., "A Study on the Application of Machine Learning and Deep Learning Techniques for Skin Cancer Detection", *Zenodo*, 2024. doi: 10.5281/zenodo.10525954.

[13] Priyadharshini, N., Selvanathan, S. N., Hemalatha, B., Sureshkumar, C., "A Novel Hybrid Extreme Learning Machine and Teaching–Learning-Based Optimization Algorithm for Skin Cancer Detection", *Healthcare Analytics*, 3, 100161, 2023. doi: 10.1016/j.health.2023.100161.

[14] Balaha, H. M., Hassan, A. E. S., "Skin Cancer Diagnosis Based on Deep Transfer Learning and Sparrow Search Algorithm", *Neural Computing and Applications*, 35, 815–853, 2023. doi: 10.1007/s00521-022-07762-9.

[15] Shah, A., Shah, M., Pandya, A., Sushra, R., Mehta, M., Patel, K., "A Comprehensive Study on Skin Cancer Detection Using Artificial Neural Network (ANN) and Convolutional Neural Network (CNN)", *Clinical eHealth*, 6, 76-84, 2023. doi: 10.1016/j.ceh.2023.08.002.

[16] Pacal, I., Alaftekin, M., Zengul, F. D., "Enhancing Skin Cancer Diagnosis Using Swin Transformer with Hybrid Shifted Window-Based Multi-Head Self-Attention and SwiGLU-Based MLP", *J Digit Imaging. Inform. Med.*, 37, 3174–3192, 2024. doi: 10.1007/s10278-024-01140-8.

[17] Kaggle, "Skin Cancer: Malignant vs Benign", *[Online]*, Available: https://www.kaggle.com/datasets/fanconic/skin-cancer-malignant-vs-benign/data.

[18] Erkan, E., Arserim, M. A., "Mobile Robot Application with Hierarchical Start Position DQN," in Computational Intelligence and Neuroscience, vol. 2022, Article ID 4115767, 21 pages, 2022. doi: 10.1155/2022/4115767.

[19] Pacal, I., "Improved Vision Transformer with Lion Optimizer for Lung Diseases Detection", *International Journal of Engineering Research and Development*, 16(2), 760-776, 2024. doi: 10.29137/umagd.1469472.

[20] Mahbod, M. A., Schaefer, G., Wang, C., Ecker, R., Ellinge, I., "Skin Lesion Classification Using Hybrid Deep Neural Networks", in: *Proc. ICASSP 2019–IEEE Int. Conf. Acoustics, Speech and Signal Processing*, Brighton, UK, May 12–17, 2019, pp. 1229–1233.

[21] DeVries, T., Ramachandram, D., "Skin Lesion Classification Using Deep Multi-Scale Convolutional Neural Networks", *arXiv*, 2017. Available: http://arxiv.org/abs/1703.01402.

[22] Kousis, I., Perikos, I., Hatzilygeroudis, I., Virvou, M., "Deep Learning Methods for Accurate Skin Cancer Recognition and Mobile Application", *Electronics*, 11(9), 1294, 2022. doi: 10.3390/electronics11091294.

[23] Pacal, I., "A Novel Swin Transformer Approach Utilizing Residual Multi-Layer Perceptron for Diagnosing Brain Tumors in MRI Images", *Int. J. Mach. Learn. & Cyber.*, 15, 3579–3597, 2024. doi: 10.1007/s13042-024-02110-w.

Middle East Journal of Science

Review

APPLICATION OF ARTIFICIAL INTELLIGENCE TECHNIQUES FOR DEFECT PREVENTION AND QUALITY CONTROL IN ARC WELDING PROCESSES: A COMPREHENSIVE REVIEW

Turgay Tugay BILGIN[1]*   *Musa Selman KUNDURACI [2]*   *Ahmet METİN[3]*
Merve PAYAR[4]   *Erdal NAYIR[5]*

[1] Bursa Technical University, Faculty of Engineering and Natural Sciences, Department of Computer Engineering, Türkiye
[2]Bursa Technical University, Faculty of Engineering and Natural Sciences, Department of Computer Engineering, Bursa, Turkiye
[3]Bursa Technical University, Faculty of Engineering and Natural Sciences, Department of Computer Engineering, Bursa, Turkiye
[4]Bursa Technical University, Faculty of Engineering and Natural Sciences, Department of Computer Engineering, Bursa, Turkiye
[5]Bursa Technical University, Faculty of Engineering and Natural Sciences, Department of Computer Engineering, Bursa, Turkiye
*Corresponding author: turgay.bilgin@btu.edu.tr

Abstract: *This study presents a comprehensive review of research applying artificial intelligence (AI) techniques to prevent defects in arc welding processes. Arc welding is essential across various industries, but numerous issues can arise, impacting weld quality and production efficiency. The review systematically analyzes relevant studies published since 2018, focusing on three key aspects: datasets used, methodologies and approaches adopted, and performance metrics reported. The findings reveal significant adoption of both machine learning and deep learning techniques, with the choice depending on factors like input data nature, welding process dynamics, and computational requirements. Deep learning models, particularly convolutional neural networks (CNNs) and long short-term memory (LSTM) networks, have demonstrated superior performance in image-based defect detection and time-series analysis for quality prediction. However, traditional machine learning algorithms have also been utilized, often coupled with dimensionality reduction or feature selection techniques. The review highlights the diverse range of performance metrics employed, such as accuracy, precision, recall, F1-score, mean squared error (MSE), and root mean squared error (RMSE). Metric selection depends on the specific task (classification or regression) and the desired trade-off between different performance aspects. While many studies reported promising results with accuracy rates frequently exceeding 90%, challenges remain in real-world industrial settings due to factors like noise, occlusions, and rapidly changing welding conditions. This review serves as a comprehensive guide for researchers and practitioners in AI-assisted defect prevention and quality control for arc welding processes, highlighting current trends, methodologies, and future research directions.*

Keywords*: arc welding, Deep Learning, Machine Learning, welding defect prevention*

1. Introduction

Welding techniques are among the most fundamental requirements of the industry. They are employed in a wide range of applications, from automotive to construction, and from aircraft and aviation technologies to the defense industry.

Arc welding encompasses various techniques that use an electric arc to join metals, each suited to different materials and applications.

1.1. Primary Types of Arc Welding

1.1.1   MIG/MAG welding

MIG/MAG welding techniques are gas metal arc welding methods. In gas metal arc welding, the necessary heat for welding is generated by an arc created between a continuously fed melting wire electrode and the workpiece, and by the resistance heating of the welding current passing through the electrode. Gas metal arc welding (GMAW), also called metal inert gas (MIG) welding, is an arc welding process in which the heat for melting the metal is generated by an electric arc between a consumable electrode and the metal. When welding is done under an active gas shield, it is called MAG welding [1].
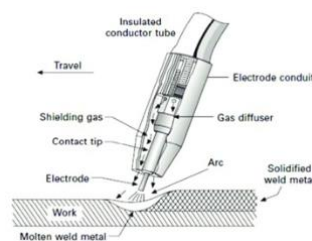
Figure 1. MIG/MAG Welding Technique [2].

For MIG welding, commonly used gases are pure argon and helium. In MAG welding, pure CO_2, argon, and O_2 are used. Schematic representation of MIG/MAG welding technique. General gases used for MIG welding include pure argon and helium, whereas pure CO_2, argon, and O_2 are used for MAG welding. Figure 1 is a schematic representation of the MIG/MAG welding technique. Gas metal arc welding, such as MIG/MAG, provides high welding speed and uses less filler metal. It is suitable for robotic welding applications [3].

There are different metal transfer modes in MIG/MAG welding:

- Short Circuit: Short circuit is the coolest form of MIG welding, utilizing low voltage. In this transfer method, the consumable electrode wire arcs and momentarily contacts the base material, causing a short circuit. This produces a small weld puddle that solidifies rapidly, often described as "fast freezing," as it drips into the joint to fuse the materials. It's ideal for welding thinner materials, though there is a risk of "cold lapping" when used on thicker metals. Additionally, this method tends to generate more spatter [4].

- Globular: Globular transfer method is very similar to the short circuit transfer method, which the consumable electrode wire arcs and touches the base material and shorts. The difference comes in how long the consumable electrode melts. In Globular method, the wire is heated longer and creates a large volume of weld metal that drips into the weld joint. It uses a high heat input and also risks less fusion because of large amounts of spatter disrupting the weld puddle. You are limited to flat and horizontal fillet welds with this method [4].

- Spray Arc: In the Spray Arc transfer method, small droplets of molten metal from the consumable electrode are sprayed into the weld joint. This is a pure CV (constant-voltage) process that sends a constant stream of weld metal across the arc to the base material. This method uses a high heat input and you risk burn-through on thinner materials and only allows for limited to flat and horizontal weld positions [4].

- Pulsed MIG: This Pulsed MIG transfer method is a modified form of the Spray Arc method, taking the best parts of all the transfer methods and minimizing their disadvantages. Pulse MIG

welding does require a special power source, which pulses the voltage many times per second. This allows one droplet of molten metal to form at the end of the consumable wire and the current, and then pushes the droplet across the arc into the weld puddle. A droplet is formed every pulse. Since the voltage drops on every pulse, this creates a longer cooling off period and may reduce the HAZ from the weld. Pulse MIG transfer minimizes spatter or the risk of cold lapping, and weld positioning is not as limited as the Globular and Spray methods [4].

During the welding process using MIG/MAG welding machines, adherence to certain parameters is imperative. These parameters constitute crucial factors that determine the quality of the weld being executed. As the thickness of the material subjected to the welding process increases, it becomes necessary to augment the intensity of the electrical current being applied.[5]. Analogously, the current value must be calibrated in accordance with the diameter of the wire being utilized. Voltage affects the arc length and the fluidity and width of the weld bead. Wire feed speed controls the amount of filler material supplied, while penetration is influenced by the current.

Defects can occur at excessive speeds, and if the wire feed speed is too low, it can result in a narrow, low-penetration, and sometimes convex weld area. Welding speed: A high welding speed results in a narrow weld area and insufficient penetration. Conversely, a slow welding speed causes an excessively wide weld area.

Additionally, the presence of shielding gas, gas flow rate, torch angle and ambient temperature also affect the quality of the weld. For optimal MIG/MAG welding, it should be performed in a closed environment to maintain the quality, as the shielding gas direction can change quickly in open air, reducing weld quality. This welding type is also sensitive to moisture and dust, so the environment must be considered carefully[6].

Aside from these factors, there are problems that can occur during welding[7]. Porosity occurs when gases present in the atmosphere are absorbed while the weld pool is still in liquid form. These gases become trapped as the metal solidifies, creating a weld filled with holes. The main causes are insufficient shielding gas or using the wrong type of shielding gas.

Undercut occurs when the weld metal expands too much and the base metal collapses towards the edges. Generally, this happens when the torch angle is too excessive in one direction, there is insufficient filler metal, or the current is too high. Burn-through, also known as a burn hole, is when the filler metal penetrates through the other side of the metal, creating a hole. The main causes are generally slow welding speed, high current, and heat being focused on one spot.

When the metals being welded do not sufficiently fuse with the weld, this is known as lack of fusion. Sometimes gaps around the edges of the weld can be observed as indicators.. The primary causes are welding too quickly, insufficient heat, an incorrect torch angle, or using electrodes or filler metal that are too small. Spatter refers to small metal droplets that surround the weld after welding. These metal particles are expelled from the torch or electrode during welding and accumulate around the weld once they solidify. While it does not damage the weld itself, it increases the time required for cleaning. Causes include low voltage, high wire feed speed, high current (amperage), and an excessively steep torch angle.

At the end of welding, craters are empty spaces. They may lead to cracks occasionally. This happens when there is not enough filler metal built up at the weld bead's end. These problems are closely related to MIG/MAG welding parameters. Therefore, before starting the welding process, attention should be paid to the welding parameters, and the correct parameters should be used.

1.1.2   TIG (Tungsten Inert Gas Welding) welding

TIG Welding (Tungsten Inert Gas Welding), also known as Gas Tungsten Arc Welding (GTAW), is a highly precise welding process that uses a non-consumable tungsten electrode to create an electric arc between the electrode and the workpiece. An inert shielding gas, typically argon or helium, protects the weld from atmospheric contamination, ensuring a clean and high-quality weld. This process can be used with or without filler metal, depending on the requirements of the job[8].
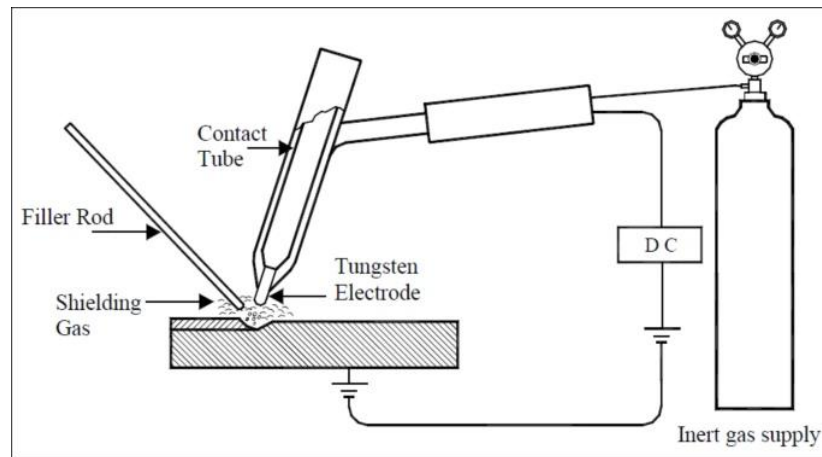
Figure 2. Schematic diagram of a TIG welding process [9].

One of the key advantages of TIG welding is the level of control it offers. The welder can manually adjust the heat input and filler material, making it ideal for welding thin materials and delicate applications. The result is a weld that is both strong and visually smooth, with minimal spatter or defects. TIG welding is versatile and can be applied to a wide range of metals, including stainless steel, aluminum, and titanium. This precision makes it widely used in industries like aerospace, automotive, and art fabrication[10].

However, TIG welding also has its challenges. It is a slower process compared to methods like MIG welding, and it requires a high level of skill and experience to master. Additionally, the equipment and labor costs are generally higher due to the manual nature of the process.

In summary, TIG welding is a method that excels in producing high-quality, clean welds with superior control over the welding process, making it an essential tool in industries requiring precision and reliability. Despite its slower pace and higher cost, the benefits it offers in terms of weld integrity and versatility make it a preferred choice for critical applications.

1.1.3   MMA (Manual Metal Arc Welding)

Manual Metal Arc Welding MMA welding, also known as Manual Metal Arc Welding or Shielded Metal Arc Welding (SMAW), is a manual welding process that uses a consumable electrode coated with flux to create the weld. In this method, an electric arc is generated between the electrode and the workpiece, producing the heat needed to melt both the electrode and the base metal. As the electrode melts, it forms a weld pool and deposits filler material, while the flux coating burns off to create a protective gas shield around the arc. This gas shield, along with the slag that forms on top of the weld, prevents the molten metal from being contaminated by the atmosphere [11].

One of the key advantages of MMA welding is its simplicity and portability. Since it doesn't require external shielding gas or complicated equipment, it is easy to transport and set up, making it ideal for outdoor and fieldwork applications. This welding method can be used on a wide range of metals, including carbon steel, stainless steel, cast iron, and some non-ferrous metals, making it highly

versatile. Additionally, MMA welding can be performed in various positions, such as horizontal, vertical, overhead, or flat, which further enhances its adaptability to different welding scenarios.

However, the process does require some skill and practice to master, as the welder must maintain the correct arc length and electrode position throughout the weld. Another challenge of MMA welding is the slag that forms from the flux coating, which must be removed after the weld cools. This adds an extra step to the process and requires more time for post-weld cleaning compared to other welding methods like MIG or TIG welding. Despite these limitations, MMA welding remains a widely used method in industries like construction, maintenance, shipbuilding, and general fabrication due to its reliability, ease of use, and flexibility in various working conditions.

Overall, while MMA welding may not be the fastest or most automated welding method, its ability to deliver strong, durable welds in a variety of settings ensures its continued relevance in many industrial applications.

1.1.4   Other Types of Arc Welding

Submerged Arc Welding (SAW) is a process where the weld is protected by a layer of granular flux. The flux not only shields the weld from contamination but also improves weld quality and allows for deep penetration. SAW is often used for welding thick materials in a horizontal position, and it is highly efficient for large-scale projects like shipbuilding or pipeline construction. The process can be automated, making it ideal for industries that require high productivity and consistency. However, SAW is typically limited to flat or horizontal welding positions due to the flow of the molten flux[11].

Flux-Cored Arc Welding (FCAW) is similar to MIG welding but uses a special flux-cored wire that provides its own shielding gas as it burns. This makes FCAW suitable for outdoor environments where wind may disrupt traditional gas shielding. It is particularly effective for welding thicker materials and for use in construction, shipbuilding, and heavy machinery fabrication. While FCAW can generate more spatter and requires post-weld cleaning, it offers the advantage of being able to weld in a variety of conditions [12].

Plasma Arc Welding (PAW) is a more advanced form of TIG welding that uses a highly concentrated plasma arc to achieve a precise and high-temperature weld. Plasma arc welding is known for its ability to produce very narrow and deep welds, making it ideal for precision work on thin materials or in applications that require high-quality, defect-free welds. The process is often used in aerospace, electronics, and medical device manufacturing due to its accuracy and control[13].

2. Approaches and techniques used in arc welding processes

In this section, the techniques and approaches used in the studies on arc welding processes that we examined are examined. Techniques and approaches other than those used in the studies are not examined.

2.1. Machine Learning

Machine Learning is defined as a way to use mathematical models to help a computer learn on its own without intervention. It is a subfield of Artificial Intelligence. Therefore, sometimes artificial intelligence and machine learning are used interchangeably. However, it is important to note that while all machine learning solutions are a form of artificial intelligence, not all artificial intelligence solutions involve machine learning.

Machine Learning is divided into two categories: Supervised and Unsupervised Learning. Supervised Learning is a type of machine learning where a model is built by training labeled data to make predictions. In supervised learning, the goal is for the model, trained with labeled input data, to correctly predict the outputs for new test data. Algorithms such as XGBoost, which is based on decision

trees and provide faster and more effective solutions by reducing the loss function [14], Naive Bayes for probabilistic classification, and SVM used for regression, classification, and outlier detection are examples of supervised learning algorithms [15].

Random Forest is a solution to the overfitting problem of decision trees by combining multiple decision trees. The dataset is randomly divided into smaller parts to create decision trees. The performance of the entire model is determined by averaging the results of each decision tree [16].

Unsupervised Learning, on the other hand, involves training a model to find similarities or patterns within unlabeled data. Since there is no labeled data in unsupervised learning, it learns on its own and is used to find relationships or clustering within data. Clustering algorithms like K-means, anomaly detection, and principal component analysis are examples of unsupervised learning [15].

2.2. Artificial Neural Network (ANN)

ANN (Artificial Neural Networks), namely Artificial Neural Networks, is an artificial intelligence model inspired by biological nervous systems. These networks perform tasks such as making predictions, classification, and decision-making by learning from data. ANNs are modeled with nerve cells (neurons) and the connections (weights) between them. ANN basic components; Input Layer, Hidden Layers, Output Layer, Neurons, Weights, and Activation Function. Data is transferred to the network in the Input Layer. Hidden Layers are processing layers inside the network. Inputs are processed in these layers and converted into more abstract representations with weights and activation functions (such as ReLU, sigmoid, and tanh). The layer where the final prediction or output of the model is formed is the output layer. ANNs are usually trained using the backpropagation algorithm to learn from data. This process calculates how much the model output differs from the expected result (error) and updates the weights to minimize this error. Errors are minimized using the gradient descent method together with the backpropagation algorithm [17].

2.2.1   Adaptive Neuro-Fuzzy Inference System (ANFIS)

ANFIS (Adaptive Neuro-Fuzzy Inference System) is a hybrid learning model that combines the strengths of artificial neural networks (ANN) and fuzzy logic systems. ANFIS integrates the adaptive learning capability of neural networks with the inference mechanism of fuzzy logic to create a powerful tool for complex decision-making and modeling non-linear systems.

ANFIS consists of 5 layers; Input Layer, Fuzzification Layer, Rule Layer, Output Layer, Summation Layer [18].

2.2.2   BP (Backpropagation) Neural Networks

Backpropagation Neural Networks are a type of Artificial Neural Network (ANN) that uses the backpropagation algorithm to train the network. The backpropagation algorithm is the foundation for learning in many neural networks, especially in supervised learning tasks.

Backpropagation Neural Networks (BP Neural Networks) are multilayered neural networks that adjust their weights through the backpropagation process. This algorithm works by propagating the error from the output layer back to the input layer, allowing the network to fine-tune its weights and improve performance on a given task [19].

2.3. Deep Learning

Deep Learning, a subset of Machine Learning, operates on artificial neural networks designed based on neural networks in the human brain. Typically trained with labeled data, deep learning can

create models capable of recognizing complex tasks and patterns. The created model can predict outputs or perform classification.

2.3.1   Convolutional Neural Network (CNN)

DNN (Deep Neural Network) is a type of artificial neural network with multiple layers between the input and output layers. The "deep" in DNN refers to the presence of multiple hidden layers, which enables the network to learn complex patterns and representations in data. Each layer in a DNN consists of neurons, or nodes, that are connected to neurons in the adjacent layers, and these connections are associated with adjustable weights.

2.3.2   Convolutional Neural Network (CNN)

Convolutional neural networks are a commonly used deep learning algorithm for analyzing images from large datasets. They use linear algebra, specifically matrix multiplication, to recognize images, bringing them into a format suitable for computer recognition and processing. The matrix format provides scalability in image classification and object detection applications.
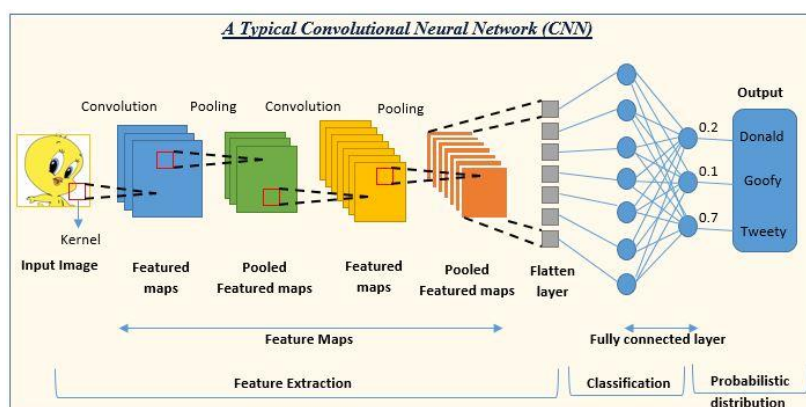
Figure 3. Convolutional Neural Network Layers [20]

Convolutional Neural Networks consist of several layers. Convolutional layer applies filters to the input images to produce feature outputs. Pooling layer reduces the data size by taking subsamples from the input data. Flatten Layer flattens the data coming in matrix form for transmission to the fully connected layer. The input data for the fully connected layer is created in this layer.

R-CNN, a region-based CNN, is used to identify the classes of objects and their bounding boxes in images. Mask R-CNN, an advanced version of R-CNN, can also predict masks for each object based on pixels, in addition to object detection or classification. It is commonly used in areas such as facial recognition and autonomous driving [21].

ResNET, one of the frequently used architectures of CNN, is designed to address the degradation problem and the vanishing gradient issue caused by the increased number of layers in deep neural networks. It facilitates training, enhances model performance, and provides higher accuracy rates [22].

2.3.3   Recurrent Neural Networks (RNN)

A Recurrent Neural Network (RNN) is a deep learning technology designed to handle time-series data. RNNs are applied and used in many research areas, including translation, document summarization, speech recognition, image recognition, disease prediction, click-through rate prediction, stock prediction, synthetic music, and e-commerce fraud detection.

In an RNN, feedback from the output variable is provided to the input. The feedback variable contains a time-delayed network. RNNs use directed cycles to solve problems in the context of input

nodes. They overcome the connection between the traditional neural network structure layer and the hidden layer. The transition between each layer node is no longer an input to a hidden layer. An RNN is a sequence-to-sequence model that can appropriately handle sequential data of any length.

The idea of RNN structure is to fully utilize the information from the previous sequence, which is common in traditional neural networks. It assumes that all inputs or outputs are independent of each other. An RNN is directly transformed into a convolutional neural network because different inputs pass through the same neural network, and the difference is hidden by the past state information of the hidden layer.
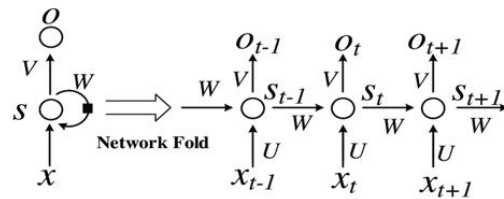
Figure 4. Basic Structure of a Recurrent Neural Network[23]

As seen in Figure 4, input data in an RNN structure is labeled as {x0, x1, x2, ..., xt+1}, while output units and hidden units are respectively labeled as {o0, o1, o2, ..., ot+1} and {s0, s1, s2, ..., st+1}. Hidden units do the most critical work. Information flows unidirectionally from inputs to hidden units and output units. Each output unit is sent to the hidden unit, performing backpropagation. Thus, the input data going to the hidden layers also include the past state information in the hidden layer.

2.3.4 Long Short-Term Memory (LSTM)

LSTM, or Long Short-Term Memory, is a neural network used in recurrent neural networks. It is particularly successful in learning long-term dependencies in sequence prediction problems.

A traditional RNN has a single hidden state transmitted over time, making it difficult for the network to learn long-term dependencies. LSTMs solve this problem by using a memory cell that can retain information for a long period. The memory cell is controlled by three gates: the input gate, the forget gate, and the output gate. These gates determine which information should be added to the memory cell, which should be removed, and which should be output from the memory cell [24].
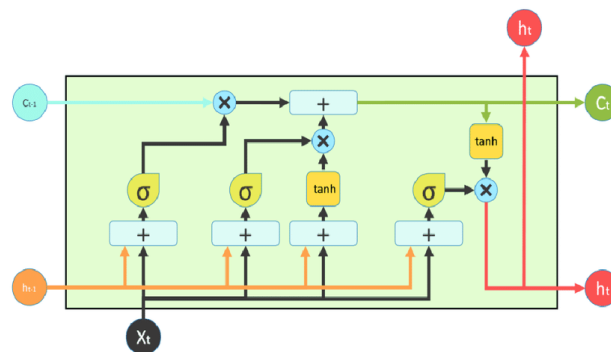
Figure 5. Long Short-Term Memory Neural Network (LSTM) Structure [24]

The input gate controls what information is added to the memory cell. The forget gate controls what information is removed from the memory cell. The output gate controls what information is output from the memory cell. This allows LSTM networks to selectively retain or discard information as it flows through the network, enabling them to learn long-term dependencies.

In LSTMs, the gates are composed of the sigmoid function. The sigmoid function produces values between 0 and 1. Due to its ability to produce positive values and definitive outputs (0 or 1), the sigmoid function is used in LSTM gates. If the value is zero, it means all information is blocked. Conversely, if the value is one, it means the information is allowed to pass.

BiLSTM-CTC is highly effective in sequence-to-sequence tasks, particularly in scenarios where alignment between inputs and outputs is uncertain, such as speech and handwriting recognition. The BiLSTM's ability to learn from both past and future context, combined with the CTC loss function's flexibility, makes this a powerful architecture for time-series and sequence problems.

2.3.5   1D Convolutional Neural Networks (1DCNN)

Deep learning models have made significant progress in automatically extracting distinctive features from time series data for classification tasks. The 1DCNN model utilizes channel attention mechanisms and residual connections to boost performance in detecting errors in signals. It shares core components with traditional CNNs like convolutional layers, ReLU activations, batch normalization, and global average pooling. A key innovation is the Squeeze and Excitation (SE) module, which models channel dependencies to emphasize important feature maps and suppress less useful ones. The residual connections enable effective reuse of features, reducing redundant computation. Collectively, the channel attention via SE and residual connections in 1DCNN allow for improved feature extraction and classification accuracy on time series data.

2.3.6   Genetic Algorithms

GAN (Generative Adversarial Networks) has provided an enhanced related dataset by using an architecture that employs two neural networks: a generative model and a discriminative model, which compete with each other to improve their predictions [25].

2.3.7   Hybrid Fuzzy Deep Learning (HFDL)

Hybrid Fuzzy Deep Learning (HFDL) refers to an advanced machine learning approach that combines elements of deep learning with fuzzy logic. This hybrid system is designed to leverage the strengths of both methodologies deep learning's capacity to model complex, hierarchical data and fuzzy logic's ability to handle uncertainty and approximate reasoning. By integrating these two, HFDL can effectively tackle problems involving ambiguous or imprecise data while still benefiting from deep learning's feature extraction and prediction capabilities[26].

3. Research Methodology

First, information on arc welding processes was collected. Subsequently, the defects and problems encountered in these processes were identified. After that, a literature review performed to explore the information technology solutions to fix these issues. Determining the right keywords was a crucial part of this research. The keywords used for the literature review are listed in Table 1.

Table 1. Keywords used in literature review

Keywords	Synonyms
Arc welding processes	Welding processes, mig/mag, tig
Deep Learning	CNN, LSTM, RNN
Machine Learning	kNN,
Welding deep learning	Tig welding
automotive	Auto, vehicle
Artificial intelligence	AI

The databases searched included Google Scholar, ACM Digital Library, Scopus, IEEE Xplore Digital Library, and arXiv.org. The search was filtered to include studies published from 2018 onwards containing the keywords listed in Table 1.

3.1. Purpose of the Review

Every review seeks to answer specific questions. The questions addressed in this review study are as follows:

- **Q1.** What approaches and techniques have been used in studies related to defect detection in arc welding processes?
- **Q2.** What datasets have been used in these studies?
- **Q3.** What performance metrics have been used in these studies?
- **Q4.** What are the performances of the studies according to these metrics?

Based on these research questions, a systematic literature review has been performed.

4. Review and Findings

In this section, a summary of the reviewed articles, dataset analysis, techniques and approach analysis, and performance analyses are provided.

4.1. Literature Summary

Recent studies on artificial intelligence in solving defects in arc welding processes, particularly in the automotive sector, have been reviewed. These studies employ different methods and approaches, resulting in varying performance metrics and datasets. This review analyzes both the differences and similarities in these studies. Additionally, the commonalities among the reviewed studies are identified to show the direction of the research.

Welding evaluation processes are generally performed post-welding, identifying defects after the welding is completed, which often leads to the disposal of expensive materials or lengthy repair processes. Even for automatic welding machines, quality inspections are typically conducted manually by humans. The studies reviewed aim to enable control by an auxiliary support mechanism. These support mechanisms demonstrate that deep learning methods perform better than general machine learning methods for time series quality classification prediction and diagnosis in various processes and systems. To address this issue in machine learning, a parallel strategy has been adopted where the overall dataset is classified, and each classified data subset is further divided into different subgroups, with a machine learning model applied to each subgroup. However, deep learning models using the LSTM structure have now dominated these efforts.

In the study by Kaiser Asif et al., an acoustic emission monitoring method for gas metal arc welding in real-time is introduced. The acoustic emission system is designed to cover a wide frequency range from 5 to 400 kHz. Various features extracted from the acoustic emission and welding parameters are fed into a machine learning algorithm. Additionally, welding parameters (current, voltage, gas flow rate, and heat input) are recorded simultaneously with the acoustic emission. Adversarial Sequence Tagging and Logistic Regression methods are applied to predict the presence of four welding conditions: good, over-penetration, burn-through, porosity, and spatter-over-penetration[27].

Due to the complexity of the resistance spot welding process, accurately knowing the operational state of the welding robot under current parameter settings and evaluating the quality of electrode caps under different sheet metal types in real-time remains a challenge. To address this issue, Geng Chen et

al. (Chen et al., 2022) propose a parallel strategy for predicting the quality of welding connections using machine learning for subsets of data with different distribution models. First, PCA (Principal Component Analysis) dimensionality reduction model was used to reduce the dimensionality of welding process feature values and the classification difficulty of data subgroups. Based on the dimension reduction data, the k-means model was applied to complete the classification of sub-data sets. The elbow method was used to adjust the number of clustering centers. Finally, the feature parameters of each sub-data set were used as inputs for machine learning, and a parallel prediction strategy for welding connection quality was developed based on the data distribution characteristics of each sub-data set. The parallel strategy adapted to the characteristics of the data population works well with more complexly distributed large welding data [28].

In the welding process of zinc-coated steel, zinc vapor causes serious porosity defects. Porosity is a significant indicator of weld quality and reduces the durability and productivity of the weld. Therefore, Seungmin Shin et al. propose a method based on a deep neural network (DNN) that can detect and predict porosity defects in real-time without the need for an additional device based on the welding voltage signal in the GMAW process. The welding current and arc voltage signals produced in the GMAW process are measured in real-time. Then, data preprocessing is performed at 0.1-second intervals to extract feature variables from the welding voltage signal. Meaningful feature variables were selected through correlation analysis between the feature variables and porosity defects, and classification models based on artificial neural networks and deep neural networks were developed. The proposed DNN-based model showed a 15% improvement in performance over the artificial neural network model. [29]

Monitoring the quality of welded joints is an important issue in cold metal transfer (CMT) overlay welding. In the CMT welding process, there are usually some abnormal problems in actual production. For example, welding gas leak, caused by excessive assembly gaps and insufficient shielding gas directly affects weld quality. In this study, Liang Liu et al. conducted an experiment on the CMT overlay welding of low-carbon steel sheets and examined the sound characteristics of CMT. In different operating modes of CMT, short-term comparisons were made of welding voltage, welding current, and arc sound. It was found that the faster the arc changes, the higher the corresponding sound pressure value. Additionally, under two abnormal welding conditions, insufficient gas supply and welding wear defect, the analysis of welding electrical parameters and welding sound signals using feature extraction and fusion methods was examined. The BiLSTM-CTC model was proposed to detect insufficient gas supply and welding wear in the welding process [30].

Kevin Meyer and Vladimir Mahalec, in their 2022 paper "Anomaly detection methods for infrequent failures in resistive steel welding" [31], attempted to detect defects in the seam resistance welding machine using a single-class neural network autoencoder and PCA (principal component analysis). The models were trained with only normal welding process data without faulty welding data, and defect detection was performed with these trained models [31].

In the paper entitled "Development of anomaly detection model for welding classification using arc sound," Phongsin Jirapipattanaporn and colleagues tried to detect the type of welding process result by using the arc sound of gas metal arc welding, commonly used in the industry, with artificial intelligence. Recurrent neural networks (RNN), long short-term memory (LSTM), and support vector machines (SVM) were used as artificial intelligence algorithms for defect detection in this project [32]. In a similar study titled "Detection of defective welds made by gas metal arc welding through analysis of sound signals," the sound signals of gas metal arc welding and the current signals drawn by the machine were used to detect problematic welds. After collecting the necessary signals and sounds, signals in the time domain were analyzed using the principal component analysis (PCA) method. These

analyzed data were used with artificial neural networks, support vector machines, decision trees, and nearest neighbor approaches to try to detect defects [33].

The University of Birmingham's Metallurgy and Materials Engineering department designed a system to monitor the TIG welding process using an HDR camera capturing images of the weld pool and surrounding area and a training system based on neural networks to identify welding defects. Unlike previous studies, the camera filters the strong light emitted by the arc, and the system adapts without needing to identify the welding direction [34]. In a similar study, seam inspection based on image processing and deep learning was conducted. This study, which aimed to achieve a 97% accuracy rate on defective reference parts, compared a standard deep learning algorithm applied to raw data with data augmentation approaches [35].

In a study conducted in China, four parameters were identified as having a greater impact on welding quality, and two main welding parameters that could determine other parameters were obtained based on correlation analysis. The study concluded that welding current and welding speed could impact welding quality by 85%. ELM-based algorithms were found to be more effective and efficient in predicting the optimal welding voltage range [36].

Another study conducted in China investigated factors affecting welding quality. Lin et al. developed a deep learning-based model for welding quality analysis and prediction to address the challenges posed by the high nonlinearity of the welding process and the complex interaction of multiple factors. Utilizing data accumulated from an automotive production line, the study proposed a Residual Neural Network (ResNet) model to predict welding quality. The model incorporated key input parameters such as the characteristic point at the end of the metal bonding process, maximum voltage, and the wear state of the electrode cap. Their results demonstrated an accuracy rate of 88.9%, offering a foundation for the automated control of welding quality [37].

Ma et al. developed an intelligent welding robot system utilizing deep learning and machine vision. Their approach involved a calibrated binocular vision system, where 1000 images were captured, and the weld positions were labeled using LabelImg software. The dataset was split into training and validation sets in a 3:1 ratio, and a convolutional neural network was trained until convergence. The TensorFlow model was optimized and deployed to a Raspberry Pi 3B+ using Intel's NCS2 edge computing stick to identify weld locations in images. By matching left and right images, the system calculated weld depth through parallax. Finally, the UR3 robot was controlled via Ethernet for automated welding [38].

Jin et al. proposed a welding seam recognition model based on the Mask R-CNN network to address challenges in vision-guided welding systems, particularly in recognizing complex welding seams. Traditionally, stereo vision systems are used to correct welding seam position defects caused by local overheating or positional deviations, but they struggle with accurately guiding laser sensors along curves with gradually changing curvatures. By employing transfer learning, Jin et al.'s model effectively identifies welding seams and segments instances in images, improving the accuracy of solder joint positioning. This approach enhances the precision of industrial robots in welding processes [39].

Charbel El Hachem worked on the automation of quality control and the reduction of nonconformity using machine learning techniques at Faurecia Clean Mobility. The thesis mentions five different contributions to the literature. The first contribution is automated quality control. The second focuses on the automation of quality control for weld seams that cover external aspects of weld defects and cannot be reached by leak tests, using deep learning methods. The third contribution combines deep learning model explain ability with weld seam classification accuracy. A hybrid approach of CNN-Machine Learning classifier was proposed to increase the accuracy achieved in the second contribution. This study presents a new model-driven optimization that achieved over 98% accuracy when applied to a weld seam dataset. The fourth contribution examines the location and relative fractures of the ceramic

monolith. Quality control of these monoliths should be carried out during the production of exhaust pipes. A comparison of image processing filters for straight line detection is presented. Tests were performed by rotating the ceramic in 5-degree increments. In 2021, Hachem et al. conducted a paper study based on the doctoral thesis. In this study, ResNet-50 and MobileNet were used. Classification of weld seams was performed using XGBoost, Decision Tree, SVM Linear, and SVM Poly5, and accuracy rates were measured [40]. In another study, Hachem et al. worked on the classification of weld seams in the automotive industry using deep learning algorithms. The welds created in this study were classified into six categories. MobileNet was used as the CNN algorithm. Data augmentation methods were used to increase the number of images used in training [35].

Martin Appiah Kesse's doctoral dissertation addresses this topic. In his study, Kesse presented a modern approach using artificial intelligence to improve efficiency and welding quality in TIG welding. This doctoral thesis aims to contribute to the state of the art in terms of the applicability of AI in welding technology by developing an AI framework using an ANFIS and a fuzzy deep neural network. The study used an ANFIS fuzzy logic model and a DNN model. After taking the necessary features for the welding process as input data, the required data is provided to the automatic welding system using a fuzzy-driven deep network model [41].

In another study that forms the basis for Kesse's doctoral thesis, Kesse et al. modeled an artificial intelligence system to predict the structural integrity in robotic GMAW of UHSS corner-welded joints [42].

Nogay and Akıncı conducted a study focused on the classification and determination of operating zones in MAG electric arc welding machines using deep learning techniques. The study analyzed the welding current graphs over a 5-second operation period. To classify the operating zones, they utilized five deep convolutional neural networks, four of which were pre-trained models through the concept of transfer learning. Their results showed that the designed model achieved 93.5% accuracy in estimating the operating range of the welding machine, while the pre-trained models achieved accuracy rates between 95% and 100% [43].

Wang et al. proposed a hybrid model that utilizes multi-source information fusion to enhance defect recognition in MIG lap welding processes. To address the limitations of single-sensor recognition methods, the model integrates molten pool images and voltage signals to detect defects such as burn-through, weld bias, and uneven width. Using a synchronized trigger device, molten pool images and weld voltage data were collected, and the Short-Time Fourier Transform (STFT) was applied to analyze the frequency variations in the voltage data. The molten pool images and time spectrograms were then fed into a hybrid CNN model for real-time defect detection. The results demonstrated that the hybrid model achieved an accuracy of 98.87%, outperforming other single-sensor-based models. The confusion matrix and Grad-CAM visualizations showed that the hybrid model effectively detects transition states in welding, offering a more accurate and balanced recognition across the entire process[44].

El Houd et al. focused on addressing the limitations of manual visual inspection in welding seam classification, which remains subjective and costly in many industries. They explored the integration of deep learning methods to enhance the accuracy and reliability of welding seam classification, particularly in the automotive sector. The study proposed a novel hybrid approach, combining model prediction scores with visual explanation heatmaps to improve defect classification. Their results demonstrated that the hybrid model outperformed target metrics, increasing classification accuracy by at least 18%, highlighting the importance of deep learning model explainability and interpretability in industrial applications[45].

Pernambuco et al. proposed a low-cost system for monitoring the stability and transfer mode of the MIG/MAG welding process by analyzing the sound signal produced by the electric arc. Recognizing the challenges of instability in welding caused by electrical variables, the authors introduced a non-

intrusive, real-time solution using an Artificial Neural Network (ANN) to detect discontinuities in the welding process. A sound signal dataset was developed through experiments simulating real-world welding conditions, including processes with adequate welds and those with two types of discontinuities. The methodology was validated using classification accuracy and a confusion matrix, demonstrating that discontinuities can be identified solely by analyzing the sound generated during welding [46].

Weld defect detection is an important task in the welding process. Although there are many excellent weld defect detection models, there is still much room for improvement in stability and accuracy. In this study, a lightweight deep learning model called WeldNet is proposed to improve the existing weld defect recognition network for its poor generalization performance, overfitting, and large memory occupation, using a design with a small number of parameters but with better performance. We also proposed an ensemble-distillation strategy in the training process, which effectively improved the accuracy rate and proposed an improved model ensemble scheme. The experimental results show that the final designed WeldNet model performs well in detecting weld defects and achieves state-of-the-art performance. Its number of parameters is only 26.8% of that of ResNet18, but the accuracy is 8.9% higher, while achieving a 24.2 ms inference time on CPU to meet the demand of real-time operation. The study is of guiding significance for solving practical problems in weld defect detection, and provides new ideas for the application of deep learning in industry[47].

Li et al. developed a vision-based monitoring system for automatic tungsten inert gas (TIG) welding of thin plates with a reserved gap, focusing on weld pool shape and fusion hole size as key factors for weld quality. To accurately detect the unstable location of the fusion hole, they proposed an improved YOLOv3 network with ResNet-d as the backbone. The optimized YOLOv3 achieved 95.03% mAP50 accuracy and a prediction speed of 49.43 frames per second (FPS). Additionally, a region-growing image processing algorithm was designed to extract clear edges and the width of the fusion hole, with the algorithm's accuracy verified through comparison with simultaneous backside images[48].

Wang et al. developed a visual sensing system for tungsten inert gas (TIG) welding, focusing on molten pool contour extraction, a key aspect of online welding quality monitoring. They designed a multi-scale feature fusion semantic segmentation network, Res-Seg, based on a residual network to improve target segmentation. To enhance the generalization ability of the model, deep convolutional generative adversarial networks (DCGAN) were used to augment the molten pool dataset, followed by color and morphological data enhancement. The proposed method was compared with traditional edge detection algorithms and other segmentation networks, demonstrating superior accuracy and robustness in real welding environments. Additionally, a back propagation (BP) neural network was used to predict weld width, with the system achieving an average defect of less than 0.2 mm, meeting welding accuracy requirements [49].

Zhang et al. proposed a deep learning-based approach for real-time defect detection in keyhole tungsten inert gas (TIG) welding, leveraging a multi-layer deep neural network trained on a large welding image dataset. Unlike support vector machines (SVMs), which are limited by manual kernel selection and perform poorly in recognizing complex weld defects such as burn-through, the neural network excels in capturing deep feature maps of molten pools and distinguishing between various weld states. The study employed a four-class classification task, identifying good welds, burn-through, partial penetration, and undercut with high accuracy and real-time performance. The method's effectiveness was supported by a comprehensive dataset, enhanced through preprocessing and data augmentation, offering a robust solution for quality control and defect prevention in keyhole TIG welding [50].

Xia et al. developed a visual monitoring system for keyhole Tungsten Inert Gas (TIG) welding, aimed at improving manufacturing quality and automation through real-time process monitoring. Using an HDR welding camera, the system monitored the weld pool and keyhole during the welding process.

A ResNet-based convolutional neural network was implemented to classify various welding states, including good weld, incomplete penetration, burn-through, misalignment, and undercut. To enhance the training dataset's diversity, image augmentation was applied, and the training process was optimized using a center loss metric learning strategy. Visualization techniques such as guided Grad-CAM, feature maps, and t-SNE were used to explain the deep learning process, providing insights into the network's effectiveness. This research lays the groundwork for developing an online monitoring system for keyhole TIG welding [51].

4.2. Input-Output Characteristics and Data Analysis

In this section, we aim to address the answer to research question Q2. During the data analysis of the studies, input data, storage method, dataset used, and output data were examined. The status of each study in these areas is shown in Table 2.

The principal objective of evaluating the methodologies and approaches employed in the research is to comprehend the ways in which artificial intelligence addresses issues in Arc welding procedures. Table 2 provides a summary of our analysis. Table 2 makes it clear that deep learning and machine learning techniques are used most often. Studies using machine learning have applied techniques such as classification, feature selection, prediction, correlation analysis, and regression. Algorithms such as XGBoost, K-means, and BP Neural Network have been utilized in these studies. A common characteristic of studies employing machine learning is that the incoming data is generally numerical.

Table 2. Data analysis of studies

Reference	Input Data	Storage Method	Dataset Used	Output Data
[27]	Welding Parameters (welding current, voltage, gas flow rate and heat input), acoustic emission	Local	Own dataset	Weld Quality (good (G), excessive penetration (Pn), burn-through (B), porosity (Pr) and porosity-excessive penetration (Pr + Pn))
[28]	Welding Parameters	Local	Own dataset	Welding quality prediction
[29]	Standard deviation of voltage, Standard deviation of instantaneous short circuit voltage, Average electrical arc (Arc) time, Number of short circuit periods, Standard deviation of short circuit duration, Standard deviation of voltage during electrical arc (Arc) period	Local	Own dataset	Porosity detection and estimation in welds
[30]	Welding Current, Welding voltage, Electrical arc sound pressure, Welding heat input electrode voltage, welding current	Local	Own dataset	insufficient gas supply and weld wear defect detection

Table 2. Continued.

Reference	Input Data	Storage Method	Dataset Used	Output Data
[31]	Welding Parameters (Temperature, current, voltage, clamping forces, carrier position, centering position)	Local	Own Dataset	Anomaly Detection
[32]	Welding Sound	Local with Raspberry Pi		weld bead type
[33]	Current and Audio Signals	WaveSCAN 2.0	Own Dataset	Online Weld Fault Detection with current signals
[34]	Welding images taken from the camera reading 55 fps are 1280x1024 pixels	Local	Own dataset	Welding quality prediction
[35]	Welding images	Local	Own dataset	Classification of source image
[36]	Oxygen Pressure, Pulse Width, Pulse Frequency, Cutting Speed, Welding Speed, Welding Current, Gas Pressure	No information	Own dataset	Welding Quality
[37]	maximum voltage, Wear status of the electrode cover	Local	Own dataset	Weld quality estimation
[39]	Welding Images	Local	Weld seam images	Irregularity of Weld Seam
[40]	Images taken from 18Mp camera	Local	Images of Faurecia Clean Mobility company	Weld seams classification
[41]	Flow, Electrical jump (Arc) length, welding speed, Weld bead width, penetration width, Depth of the heat affected zone, Width of heat affected zone	Local	Own dataset	Tensile Strength and yield strength estimation
[42]	Electrical surge (Arc) current, Electrical surge (Arc) voltage, welding speed, gas flow rate, electrode extension, Electrical jump (Arc) length, wire feeding speed, wire diameter, welding torch position, Welding torch movement angle	Local	Own dataset	Estimation of resource properties
[43]	Welding current graph,	Local	Own dataset	Classification of operation cases in electric arc welding machine

Table 2. Continued.

Reference	Input Data	Storage Method	Dataset Used	Output Data
[45]	Welding Images	Local	Own dataset	Classification of Weld Defective and Perfect
[46]	Welding audio signals	Local	Own dataset	Welding defect detection
[47]	Welding Images	Local	TIG Al5083 [34]	Weld defect detection
[48]	Welding images	Local	Own dataset	Detect fusion hole state and size during TIG welding
[49]	Welding Images	Local	Own dataset	Extract the contour of the molten pool in TIG stainless steel welding
[50]	Welding images	Local	Own dataset	Classification of weld quality
[51]	Weld images, Grad-CAM Images Guided Backprop	Local	Own dataset	Classification of weld quality

Deep learning studies have used techniques such as classification and object detection. Studies focused on classification have categorized the quality of MIG/MAG welds based on images, classifying them as either defective or non-defective. Object detection techniques have been used alongside classification to identify defects in welds. Deep learning studies have employed network models and algorithms such as ResNet, LSTM, and MobileNet. These models and algorithms may have been preferred due to their speed and low error rates.

In summary, upon reviewing recent studies in this field, it is observed that both machine learning and deep learning are utilized in nearly all studies. In this domain, only image processing or signal processing techniques are not solely used. Researchers should determine their approach and method based on the type of incoming data (image, numerical data), and choose algorithms and models according to time, speed, and hardware requirements.

4.3. Analysis of Methods and Techniques Used

In this section, the approaches and techniques used in the studies are analyzed. Additionally, for approaches utilizing deep learning, any CNN models and libraries employed are identified.

Table 3. Method and Technical Analysis of Studies.

Reference	Approach	Techniques Used	Network Model or Algorithm
[27]	Machine Learning NLP	Classification Attribute Selection	Logistic Regression - Adversarial Sequence Tagging (AST)
[28]	Machine Learning	Classification Classification	BP Neural Networks / PKB (PCA-K-means-BP)
[29]	Machine Learning	Classification, Correlation analysis	Deep neural networks (DNN), Artificial neural network (ANN)
[30]	Deep Learning, Audio and Signal Processing, Time series	Classification, normalization	BiLSTM-CTC LSTM
[31]	Machine Learning Signal Processing	Classification	PCA, Autoencoder, SUM-PCA, DUM-autoencoder
[32]	Machine Learning	Classification	RNN, SVM, LSTM
[33]	Machine Learning Signal Processing	Classification	PCA, Naive Bayes C. SVM, Decision Trees, Boosted Trees, Random Forest, ANN, Nearest Neighbor, KNN

Table 3 Continued.

Reference	Approach	Techniques Used	Network Model or Algorithm
[34]	Deep Learning	Binary image classification, Multi image classification	Conv6, Conv2, FullyCon6, FullyCon2
[35]	Deep Learning, Image processing,	Binary classification, Data augmentation,	CNN, MobileNet
[36]	Machine Learning	Regression, Correlation analysis,	Back Propagation Neural Network, Extreme Learning Machine, Support vector machine
[37]	Deep Learning	Normalization, Regression, Residual connection	ResNet18
[39]	Deep Learning Image processing	Classification Object Detection – object identification	Mask R-CNN / ResNet - RoIAlign(a method used to extract a small feature map from each RoI)
[40]	Image processing, Deep Learning,	Data augmentation, Image classification, Imbalanced data,	ResNet50, MobileNet-XGboost classifier, MobileNet-SVM Poly5 kernel, GradCAM, Support Vector Machine Classifier, Decision Tree Classifier, canny filter, Laplacian edge detector, Hough lines
[41]	Machine Learning	Regression, Data augmentation	Adaptive Neuro-fuzzy Inference System (ANFIS), DNN
[42]	Machine Learning	Regression	Artificial neural network with back propagation, Artificial neural networks with Levenberg-Marquardt
[43]	Deep Learning	Classification	DCNN
	Deep Learning	Detection	ResNet
[45]	Machine Learning	Classification	MobileNet – XGBoost MobileNet-SVM
[46]	Machine Learning	Prediction, Classification	Neural Network(ANN)
[47]	Deep Learning	Classification	CNN, FCN, Own model similar Resnet18
[48]	Deep Learning	Classification	CNN, YOLOv3
[49]	Deep Learning	Segmentation, Data augmentation	Res-Seg, DCGAN
[50]	Deep Learning	Classification	CNN, ResNet
[51]	Deep Learning Machine Learning	Classification	CNN, Center-loss ResNet, ResNet, SVM,

4.4. Performance Metrics

Performance metrics are used in academic research to measure the performance of an approach. Evaluating the efficiency and accuracy of machine learning models, particularly deep learning models, relies heavily on performance measurements. There are several performance metrics designed to capture different aspects of model performance for each algorithm. This performance is typically measured by comparing the model's predictions or classifications with the ground-truth values obtained from labeled data.

4.4.1   Classification Metrics

Confusion Matrix is a comparison of model predictions and ground-truth labels in tabular form. When the output can include two or more different types of classes, it is the simplest approach to measure how well a classification task performs. The confusion matrix serves as a basis for evaluating results rather than serving as a performance metric on its own. Accuracy is the percentage of examples that the algorithm correctly classifies out of all examples. It is useful when all classes are equally important.

Precision represents the ratio of true positive results to the number of all positive results predicted by the model. Precision indicates the probability of a positive result being correct. When dealing with imbalanced distributions of classes, classification accuracy is not an ideal measure to evaluate how well a model works. We need a precision measure that is produced by dividing true positives by the sum of true positives and false positives to address a specific issue for a certain class [52]. Precision indicates the percentage of positive predictions that are actually correct. Recall, also known as Sensitivity, is a measure of how many of the actual positive instances were correctly predicted. Specificity measures the performance in categorizing negative examples. It represents the percentage of true negatives correctly identified among all negative examples. F1 Score is the harmonic mean of precision and recall and is used to evaluate the accuracy of a test. It can range from a minimum of 0 to a maximum of 1. The model's robustness and sensitivity are generally measured with it. It is difficult to evaluate two models with high recall but low precision. To compare them, we use the F1 score. The F1 score is the harmonic mean of two numbers, one small and one large, both of which are precision and recall.

The performance of a classification problem at various threshold values is measured using the AUC-ROC curve. ROC is a probability curve, the area under ROC is known as AUC, which is calculated by taking the integral. It speaks of the ability to distinguish different model types. The higher the AUC, the more accurate the model is expected to predict. Thresholds are values that need to be determined depending on the problem.

In computer vision and object detection tasks, Intersection over Union (IoU) metrics are often used to evaluate the accuracy of an object's position. IoU is a frequently used evaluation metric that assesses how accurately an object's location is predicted. The actual location of the object is indicated by the ground truth bounding box. The first step in calculating IoU is to find the intersection area of the predicted bounding box and the ground truth bounding box. If there is no overlap, there is no intersection area. The area created by both boxes together, including the intersection area, is called the union area. IoU measures how much of the predicted bounding box overlaps with the ground truth bounding box. To calculate IoU, the intersection area is divided by the union area:

$$IoU \ = \ Intersection \ Area \ / \ Union \ Area \qquad (1)$$

An Intersection over Union (IoU) value of 1 indicates a perfect match, where the predicted and ground truth bounding boxes completely overlap; whereas a value of 0 signifies no overlap. It offers a single scalar value indicating the accuracy in determining object locations, facilitating comparison across various detection techniques or models.

Another popular evaluation statistic in the field of computer vision is the mean Average Precision (mAP), which provides a comprehensive assessment of the performance and accuracy of an algorithm or model across multiple object categories. The Average Precision (AP) score for each object category is determined individually, and the average of these individual AP scores is then used to form the mAP. The general method for calculating mAP is as follows:
- Generate a Precision-Recall (PR) curve. The algorithm or model ranks discovered objects based on confidence scores for each object category. Plotting Precision (y-axis) against Recall (x-axis) as the detection threshold varies results in the PR curve. Precision represents the ratio of true positives

to all positive detections, while Recall represents the ratio of true positives to all ground truth objects.

- Calculate the area under the PR curve to obtain the Average Precision (AP) score. Computing the integral of precision values at various recall levels yields this area. For a specific object category, the model's precision-recall performance is summarized by the AP score.

- Compute the mAP: After determining the AP scores for all object categories, the mAP is calculated by taking the average of each category's AP scores. (2).

The Mean Average Precision (MAP) metric is useful because it provides a comprehensive evaluation of the model's detection capabilities by assessing its performance across multiple object categories. By offering a single scalar value that represents the model's average performance, MAP facilitates the comparison of various algorithms or models.

$$mAP \ = \ \frac{1}{N}\sum_{i=1}^{N} AP_i \tag{2}$$

The False Discovery Rate (FDR) is a measure of accuracy used in multiple hypothesis testing when several measurements or changes are observed in a single experiment, which accounts for multiple hypotheses being simultaneously investigated. The FDR regulates the percentage of false discoveries (also known as false positives) among the rejected hypotheses. As the number of tests conducted increases, so does the probability of false positive findings. The estimated ratio of false discoveries (false positives) to all discoveries (rejected hypotheses) is known as the False Discovery Rate. Since it is dependent on unforeseen outcomes, controlling the FDR is more challenging.

4.4.2   Regression Metrics

Mean Squared Error (MSE) is the average of the squared differences between the target value and the value predicted by the regression model. Essentially, it measures what has been discovered. MSE provides a measure of model accuracy by considering both the size and direction of errors.

Root Mean Squared Error (RMSE) is the square root of the average of the squared differences between the value predicted by the regression model and the target value. A larger RMSE indicates larger prediction errors, while a lower RMSE indicates better prediction accuracy. Mean Absolute Error (MAE) is the average of the absolute differences between the actual values and the predicted values across all observations in the dataset. Better accuracy is indicated by a lower value. This metric does not consider the direction of errors because taking the absolute value guarantees the differences are positive. Unlike MSE, which is differentiable, MAE is not differentiable. It provides a measure of how far the model's predictions are from the actual results. Unlike MSE and RMSE, MAE does not square the errors, making it more robust to outliers. The R-squared metric gives a measure of how well a set of predicted output values matches the actual output values and is often used for explanatory purposes. R-squared is not a reliable indicator of how well a regression model fits your data. A good model might have a low R-squared value, and conversely, a biased model might have a high R-squared value. The model's performance can be evaluated by comparing the R-squared metric against a fixed baseline. The fixed baseline is selected by taking the average of the data and placing the line at the mean.

A model performing at the fixed baseline will have an R-squared value equal to 0. Higher R-squared values indicate better models, with the best model giving an R-squared of 1, indicating all correct predictions. The R-squared value increases as new features are added to the model. We can calculate R-squared as follows:

$$R^2 = 1 - \frac{MSE(Model)}{MSE(Baseline)} \qquad (3)$$

$$\frac{MSE(Model)}{MSE(Baseline)} = \sum_{i=1}^{N}(y_i - \hat{y})^2 / (\overline{y_i} - \hat{y}_i)^2 \qquad (4)$$

- MSE (Model): Average squared error of predictions compared to the actual values.
- MSE (Baseline): Average squared error of average predictions compared to the actual values.

As more independent variables are included, the R-squared value of a model always increases. As independent variables come into play, the model becomes more complex, and as the model becomes more complex, it tends to overfit. Thus, when features that do not improve the model are added, the R-squared value increases, and R-squared does not penalize them. To address these issues, it is necessary to use adjusted R-squared. Each independent variable is considered by adjusted R-squared only when it significantly improves the variable model. Adjusted R-squared is used to address the problem of R-squared, but it will always show a lower number than R-squared.

4.4.3   Other Metrics

Mean Square Reconstruction Error (MSRE) is commonly used to assess the accuracy of reconstruction in various signal processing and data compression applications, especially when it comes to autoencoders and other unsupervised learning methods. MSRE calculates the mean squared difference between the original and reconstructed forms of input data. The goal when expressing and reconstructing data is typically to minimize distortion or reconstruction error. MSRE provides a quantitative evaluation of a model's or algorithm's ability to reconstruct the original input data. By squaring the inconsistencies between original and reconstructed data, it penalizes larger errors more severely than smaller ones, emphasizing the value of capturing the features and patterns of input data accurately. Lower MSRE levels indicate more accurate reconstruction, as they suggest that the recovered data closely resembles the original input. Conversely, higher values indicate greater discrepancies between original and reconstructed data.

When alignment between inputs and target labels is unknown, Connectionist Temporal Classification (CTC) is used to solve sequence labeling problems, especially for temporal classification tasks. Machine learning, particularly deep learning, employs the CTC method for sequence labeling problems. First proposed by Alex Graves in 2006, it has since been widely used for various applications, including speech recognition, handwriting recognition, and machine translation.

The choice of metric depends on the task at hand, and often requires customization to meet specific requirements and prioritize different objectives. Performance metrics contribute to improving machine learning models by providing useful information about the advantages and disadvantages of various models.

Prediction Interval (PI) provides a measure of uncertainty for predictions in regression problems. For example, a 95% prediction interval indicates that out of 100 samples, the actual value will be between the lower and upper bounds of the interval 95 times. There are several performance evaluation metrics that can be used accordingly.

Coverage Ratio (CR) represents the degree to which actual data is covered by the prediction interval. As this value increases, the accuracy of the model in classifying actual data increases.

Performance analyses of the studies have been conducted and summarized in Table 4. As seen in Table 4, in many studies, since classification is involved, Accuracy has been used as the performance metric to measure classification success. The choice of performance metric varies depending on the desired outcome and the technique used. When making a classification using Deep Learning or Machine Learning, metrics such as Recall, Precision, and F1 score are used. However,

when performing object detection with Deep Learning, the IoU metric is used. If the desired output is regression, metrics such as MSE, RMSE, MAE have been used [28].

Table 4. Method and Technical Analysis of Studies

Reference	Performance Metrics	Results
[27]	Accuracy	91.18% accuracy for Adverserial Sequence Tagging
[28]	R^2 , MSE, MAE, MRE	BP: 0.4-0.5 / PBP: 0.81-0.96 Best results in order: 18.4223, 3.7143, 0.0500, 0.9600(96% success)
[29]	Prediction Accuracy	ANN: 0.659(dataset 1), 0.790(dataset 2) DNN: 0.858(dataset 1), 0.895(dataset 2)
[30]	Classification Error Rate	0.295
[31]	MSRE	Mean 0.0267
[32]	Accuracy	RNN Model Test Accuracy: 89.67% LSTM Model Test Accuracy: 78.57%
[33]	Accuracy	Decision Tree model accuracy: 80%
[34]	Accuracy, Precision, Recall, F-score	Fully-conv6: Accuracy: 69% F-score: 0.56 Conv6: Accuracy: 93.4% F-score: 0.78 Fully-conv2 Accuracy: 89.5% F-score: 0.89 Conv2: Accuracy: 75.5% F-score: 0.75
[35]	Accuracy	Overall accuracy: 97 %
[36]	CR, AIW	BPNN Model - CR Average: 0.8516 AIW Average: 1.5084 ELM Model - CR Average: 0.9297 AIW Average: 1.4536 SVM Model - CR Average: 0.9041 AIW Average: 1.4358
[37]	Accuracy	Accuracy: 88.9%
[39]	mAP - Recall	mAP:95% – Recall: 76%
[40]	R^2 Accuracy per Classifier	R^2 Laplacian-Hough lines: 0,8291 R^2 Canny-Hough lines: 0,9969 XG-Boost Accuracy: 99.3% (Weld2) , 98.7% (Weld3) Decision Tree Accuracy: 98.1% (Weld2) , 97.2% (Weld3) SVM Linear Accuracy: 98.8% (Weld2) , 98.1% (Weld3) SVM Poly5 Accuracy: 98.8% (Weld2) , 98.7% (Weld3)
[41]	RMSE	Tensile strength: 2.392 Yield strength: 12,546
[42]	RMSE	0.0000845
[43]	Accuracy	Accuracy : 93.5 %
[45]	Accuracy	MobileNet Model Average Accuracy: 98% ResNet50 Model Average Accuracy: 97%
[46]	Accuracy	Accuracy: 80.61%
[47]	Accuracy Precision Recall F1-score	Accuracy: 83.5% Precision: 75.1% Recall: 78.4% F1-score: 74.9%
[48]	mAP50, FPS	mAP50 Mean: 95.11% FPS: 49.71

Table 4 Continued.

Reference	Performance Metrics	Results
[49]	Segmentation accuracy	Molten pool(M),Background(B) Res-Seg (Based on ResNet-34) M: 91.94% B: 99.33% Res-Seg (Based on ResNet-50) M: 93.71% B: 99.28% Res-Seg (Based on ResNet-101) M: 93.80% B: 99.21% Res-Seg (Based on ResNet-50) + DCGAN M: 94.77% B: 99.32%
[50]	Accuracy, Precision	SVM based model accuracy:
[51]	Accuracy, Precision	Center-loss Resnet Model: Average Precision value: 0.984 Average Accuracy value: 0.984 Resnet: Average Precision value: 0.978 Average Accuracy value: 0. 978 SVM: Average Precision value: 0.90 Average Accuracy value: 0.846

5. Discussion

This study examines the use of artificial intelligence (AI) techniques for defect prevention and quality control in Arc welding processes. The reviewed studies generally cover AI applications such as image processing and time-series analysis, with deep learning methods demonstrating superior performance, particularly in image-based defect detection and time-series analysis. Although deep learning algorithms have achieved higher accuracy rates compared to traditional machine learning methods, these techniques face challenges in industrial environments due to noise, obstructions, and varying welding conditions.

While many studies reported accuracy rates exceeding 90%, it was concluded that further research is needed to improve the performance of these systems in real-world industrial applications. Additionally, AI-assisted error prevention systems are expected to significantly contribute to reducing costs and speeding up quality control processes in manufacturing.

In this context, future research should focus on improving the real-time performance of these systems and enhancing the generalizability of AI models. This review provides a broad overview of the current state of AI techniques for error prevention and quality control in Arc welding processes and aims to guide future research in this field.

Method, dataset and performance analyses of artificial intelligence studies to detect errors in Arc welding processes have been conducted. Many different data types, methods and performance metrics were used in the studies.

The techniques and approaches used in the study vary according to the problems and objectives of the studies. For example, while Deep Learning approaches and techniques are used in a study that classifies the quality of the source from the source image, machine learning techniques are used in a study that classifies the source from the data obtained from various sensors during the process.

Each technique has its specific strengths depending on the task (e.g., classification, time series prediction, anomaly detection). Deep learning models like DNNs and CNNs offer powerful pattern recognition but require significant data and computational power. Traditional machine learning models like SVM and decision trees are easier to implement and interpret but may not perform as well on

highly complex data. Hybrid methods like PCA-K-means-BP and BiLSTM-CTC combine multiple approaches to improve performance in specific use cases.

This review has some limitations. These are as follows:

The use of different and non-standard data collection forms in studies reviewed, experiencing difficulties with interpretation of data arc welding processes.

The limitations of the study are as follows:

The lack of standardization in data collection methods across the reviewed studies has created challenges for comparative analysis. Some studies utilized custom datasets, but the lack of access to these datasets limits the generalizability of the findings.

The reviewed studies employed different types of data (images, audio signals, current/voltage data) and data sizes, making it difficult to compare techniques. Some studies focused solely on image data, while others relied on sensor data, leading to inconsistencies in the comparison of results.

While AI models have achieved high accuracy rates in controlled environments, their performance in real-world industrial settings is limited by factors such as noise, environmental variability, and rapidly changing conditions. Many challenges remain for real-time applications in these environments.

Most studies provided solutions tailored to specific problems using customized datasets. However, there is limited information on whether these solutions can be generalized to different welding processes, materials, or industrial environments.

Many studies relied on proprietary datasets created by researchers. The lack of publicly available datasets makes it difficult for other researchers to replicate experiments or compare results.

AI techniques, particularly deep learning models, require large datasets and significant computational power to achieve high accuracy. This can lead to delays and performance issues in certain applications. In welding processes that require real-time decision-making, hardware limitations may hinder the models' effectiveness.

These limitations affect the scope of the study and the generalizability of the findings.

6. Conclusions

This review paper has presented a comprehensive analysis of recent studies employing artificial intelligence techniques to prevent defects in Arc welding processes. The analysis covered three key aspects: datasets utilized, methodologies and approaches adopted, and performance metrics reported.

Several notable conclusions can be drawn from this study:

Most researchers have relied on their own custom datasets tailored to the specific welding defects or applications under investigation, given the unique challenges and solutions involved in each study.

For classification tasks, deep learning models like convolutional neural networks (CNNs) and long short-term memory (LSTM) networks have demonstrated superior performance compared to traditional machine learning algorithms, particularly when dealing with image or time-series data.

A diverse range of performance metrics have been employed, including accuracy, precision, recall, F1-score, mean squared error (MSE), and root mean squared error (RMSE), with the selection of metric contingent upon the specific task (classification or regression) and the desired trade-off between different performance aspects.

While many studies have reported promising results, with accuracy rates frequently exceeding 90%, there remains room for improvement, especially in real-world industrial settings where factors such as noise, occlusions, and rapidly changing welding conditions can pose significant challenges.

Overall, this review highlights the growing adoption of artificial intelligence techniques, particularly deep learning, in the domain of error prevention and quality control for Arc welding

processes. As the field continues to evolve, further research is warranted to enhance the robustness, generalizability, and real-time applicability of these methods across.

Ethical statement

Acknowledgment

Conflict of interest

All authors have none to declare.

Authors' Contributions

All authors mentioned in the paper must have significantly contributed to the research. The contributions of the authors are listed below.
TTB: Conceptualization, Methodology, Formal analysis, Investigation
MSK: Formal analysis, Resources, Writing - Original draft preparation
AM: Formal analysis, Resources, Writing
MP: Resources, Investigation
EN: Investigation

References

[1] K. Weman and G. Lindén, *MIG welding guide*. Woodhead Publishing, 2006.

[2] J. Norrish, *Advanced Welding Processes*. Institute of physics Publishing, 1992.

[3] "What is MIG/MAG Welding?" [Online]. Available: https://www.fronius.com/en/welding-technology/world-of-welding/mig-mag-welding

[4] D. Young, "MIG Welding Transfer Methods - A.E.D. Motorsport Products," *A.E.D. Motorsport Products*. [Online]. Available: https://www.aedmetals.com/news/mig-welding-transfer-methods

[5] Miller, "MIG Welding: Setting the Correct Parameters," Miller.

[6] S. C. A. Alfaro and P. Drews, "Intelligent Systems for Welding Process Automation," *J. of the Braz. Soc. of Mech. Sci. & Eng.*, vol. XXVIII, no. 1, pp. 25–29, 2006.

[7] Unimig, "Troubleshooting Your Weld – The 12 Most Common Problems & How to Fix Them," Unimig.

[8] R. Singh, *Arc welding processes handbook*. John Wiley & Sons, 2021.

[9] A. B. Short, "Gas tungsten arc welding of α + β titanium alloys: A review," *Materials Science and Technology*, vol. 25, no. 3, pp. 309–324, Mar. 2009, doi: 10.1179/174328408X389463.

[10] K. Weman, *Welding processes handbook*. Elsevier, 2011.

[11] L. F. Jeffus, H. V Johnson, and A. Lesnewich, *Welding: principles and applications*. Delmar Publishers New York, 1999.

[12] P. Kah, R. Suoranta, and J. Martikainen, "Advanced gas metal arc welding processes," *The International Journal of Advanced Manufacturing Technology*, vol. 67, pp. 655–674, 2013.

[13] F. Khoshnaw, I. Krivtsun, and V. Korzhyk, "Arc welding methods," in *Welding of Metallic Materials*, Elsevier, 2023, pp. 37–71.

[14] T. Chen *et al.*, "Xgboost: extreme gradient boosting," *R package version 0.4-2*, vol. 1, no. 4, pp. 1–4, 2015.

[15] T. M. Mitchell and T. M. Mitchell, *Machine learning*, vol. 1, no. 9. McGraw-hill New York, 1997.

[16] L. Breiman, "Random forests," *Mach Learn*, vol. 45, no. 1, pp. 5–32, 2001.

[17] B. Yegnanarayana, *Artificial neural networks*. PHI Learning Pvt. Ltd., 2009.

[18] J.-S. Jang, "ANFIS: adaptive-network-based fuzzy inference system," *IEEE Trans Syst Man Cybern*, vol. 23, no. 3, pp. 665–685, 1993.

[19] R. Hecht-Nielsen, "Theory of the backpropagation neural network," in *Neural networks for perception*, Elsevier, 1992, pp. 65–93.

[20] E. Eze and J. Eze, "Artificial Intelligence Support For 5g/6g-Enabled Internet of Vehicles Networks: An Overview." [Online]. Available: https://www.itu.int/en/journal/j-fet/Pages/default.aspx

[21] K. He, G. Gkioxari, P. Dollár, and R. Girshick, "Mask R-CNN," Mar. 2017, [Online]. Available: http://arxiv.org/abs/1703.06870

[22] K. He, X. Zhang, S. Ren, and J. Sun, "Deep Residual Learning for Image Recognition," Dec. 2015, [Online]. Available: http://arxiv.org/abs/1512.03385

[23] L. R. Medsker and L. C. Jain, "Recurrent neural networks," *Design and Applications*, vol. 5, pp. 64–67, 2001.

[24] S. Hochreiter and J. Schmidhuber, "Long short-term memory," *Neural Comput*, vol. 9, no. 8, pp. 1735–1780, 1997.

[25] I. Goodfellow *et al.*, "Generative adversarial networks," *Commun ACM*, vol. 63, no. 11, pp. 139–144, 2020, doi: 10.1145/3422622.

[26] Y. Zheng, Z. Xu, and X. Wang, "The fusion of deep learning and fuzzy systems: A state-of-the-art survey," *IEEE Transactions on Fuzzy Systems*, vol. 30, no. 8, pp. 2783–2799, 2021.

[27] K. Asif, L. Zhang, S. Derrible, J. E. Indacochea, D. Ozevin, and B. Ziebart, "Machine learning model to predict welding quality using air-coupled acoustic emission and weld inputs," *J Intell Manuf*, vol. 33, no. 3, pp. 881–895, Mar. 2022, doi: 10.1007/s10845-020-01667-x.

[28] G. Chen, B. Sheng, R. Luo, and P. Jia, "A parallel strategy for predicting the quality of welded joints in automotive bodies based on machine learning," *J Manuf Syst*, vol. 62, pp. 636–649, Jan. 2022, doi: 10.1016/j.jmsy.2022.01.011.

[29] S. Shin, C. Jin, J. Yu, and S. Rhee, "Real-time detection of weld defects for automated welding process base on deep neural network," *Metals (Basel)*, vol. 10, no. 3, Mar. 2020, doi: 10.3390/met10030389.

[30] L. Liu, H. Chen, and S. Chen, "Quality analysis of CMT lap welding based on welding electronic parameters and welding sound," *J Manuf Process*, vol. 74, pp. 1–13, Feb. 2022, doi: 10.1016/j.jmapro.2021.11.055.

[31] K. Meyer and V. Mahalec, "Anomaly detection methods for infrequent failures in resistive steel welding," *J Manuf Process*, vol. 75, pp. 497–513, Mar. 2022, doi: 10.1016/j.jmapro.2021.12.003.

[32] P. Jirapipattanaporn and W. Lawanont, "Development of Anomaly Detection Model for Welding Classification Using Arc Sound," in *KST 2022 - 2022 14th International Conference on Knowledge and Smart Technology*, Institute of Electrical and Electronics Engineers Inc., 2022, pp. 57–62. doi: 10.1109/KST53302.2022.9729058.

[33] S. F. Laving, "Gas Metal Arc Welding Defect Detection using Sound signals," Master Thesis, Seljuk University Institute of Science, Konya, 2019.

[34] D. Bacioiu, G. Melton, M. Papaelias, and R. Shaw, "Automated defect classification of SS304 TIG welding process using visible spectrum camera and machine learning," *NDT and E International*, vol. 107, Oct. 2019, doi: 10.1016/j.ndteint.2019.102139.

[35] C. El Hachem, G. Perrot, L. Painvin, J. B. Ernst-Desmulier, and R. Couturier, "Welding Seam Classification in the Automotive Industry using Deep Learning Algorithms," in *Proceedings - 2021 IEEE International Conference on Industry 4.0, Artificial Intelligence, and Communications Technology, IAICT 2021*, Institute of Electrical and Electronics Engineers Inc., Jul. 2021, pp. 235–240. doi: 10.1109/IAICT52856.2021.9532569.

[36] H. Guo, L. Lin, Y. Lv, J. Liu, and C. Tong, "Machine Learning for Determining Key Parameters in Welding Process of Underground Engineering Equipment," in *Proceedings of 2021 IEEE International Conference on Sensing, Diagnostics, Prognostics, and Control, SDPC 2021*, Institute of Electrical and Electronics Engineers Inc., 2021, pp. 33–41. doi: 10.1109/SDPC52933.2021.9563365.

[37] J. Lin, J. Lu, J. Xu, and D. Li, "Welding quality analysis and prediction based on deep learning," in *Proceedings - 2021 4th World Conference on Mechanical Engineering and Intelligent Manufacturing, WCMEIM 2021*, Institute of Electrical and Electronics Engineers Inc., 2021, pp. 173–177. doi: 10.1109/WCMEIM54377.2021.00045.

[38] X. Ma, S. Pan, Y. Li, C. Feng, and A. Wang, "Intelligent welding robot system based on deep learning," *Proceedings - 2019 Chinese Automation Congress, CAC 2019*, pp. 2944–2949, 2019, doi: 10.1109/CAC48633.2019.8997310.

[39] X. Jin, L. Lv, C. Chen, F. Yang, and T. Chen, "A New Welding Seam Recognition Methodology Based on Deep Learning Model MRCNN," in *2020 7th International Conference on Information, Cybernetics, and Computational Social Systems, ICCSS 2020*, Institute of Electrical and Electronics Engineers Inc., Nov. 2020, pp. 767–771. doi: 10.1109/ICCSS52145.2020.9336927.

[40] C. El Hachem, "Automation of quality control and reduction of non-compliance using machine learning techniques at Faurecia Clean Mobility." [Online]. Available: https://theses.hal.science/tel-03775370

[41] M. A. Kesse, "Artificial intelligence: A modern approach to increasing productivity and improving weld quality in TIG welding," Doctoral Thesis, Lappeenranta-Lahti University of Technology LUT, Lappeenranta, 2021.

[42] E. A. Gyasi, P. Kah, H. Wu, and M. A. Kesse, "Modeling of an artificial intelligence system to predict structural integrity in robotic GMAW of UHSS fillet welded joints," *International Journal of Advanced Manufacturing Technology*, vol. 93, no. 1–4, pp. 1139–1155, Oct. 2017, doi: 10.1007/s00170-017-0554-0.

[43] H. S. Nogay and T. C. Akinci, "Classification of operation cases in electric arc welding wachine by using deep convolutional neural networks," *Neural Comput Appl*, vol. 33, no. 12, pp. 6657–6670, Jun. 2021, doi: 10.1007/s00521-020-05436-y.

[44] J. Wang *et al.*, "On-line defect recognition of MIG lap welding for stainless steel sheet based on weld image and CMT voltage: Feature fusion and attention weights visualization," *J Manuf Process*, vol. 108, pp. 430–444, Dec. 2023, doi: 10.1016/j.jmapro.2023.10.081.

[45] A. El Houd, C. El Hachem, and L. Painvin, "Deep Learning Model Explainability for Inspection Accuracy Improvement in the Automotive Industry," Oct. 2021, [Online]. Available: http://arxiv.org/abs/2110.03384

[46] B. S. G. Pernambuco, C. R. Steffens, J. R. Pereira, A. V. Werhli, R. Z. Azzolin, and E. Da Silva Diaz Estrada, "Online sound based arc-welding defect detection using artificial neural networks," in *Proceedings - 2019 Latin American Robotics Symposium, 2019 Brazilian Symposium on Robotics and 2019 Workshop on Robotics in Education, LARS/SBR/WRE 2019*, Institute of Electrical and Electronics Engineers Inc., Oct. 2019, pp. 263–268. doi: 10.1109/LARS-SBR-WRE48964.2019.00053.

[47] R. Wang, H. Wang, Z. He, J. Zhu, and H. Zuo, "WeldNet: a lightweight deep learning model for welding defect recognition," *Welding in the World*, 2024, doi: 10.1007/s40194-024-01759-9.

[48] S. Li, J. Gao, E. Zhou, Q. Pan, and X. Wang, "Deep learning-based fusion hole state recognition and width extraction for thin plate TIG welding," *Welding in the World*, vol. 66, no. 7, pp. 1329–1347, Jul. 2022, doi: 10.1007/s40194-022-01287-4.

[49] Y. Wang, J. Han, J. Lu, L. Bai, and Z. Zhao, "TIG stainless steel molten pool contour detection and weld width prediction based on Res-Seg," *Metals (Basel)*, vol. 10, no. 11, pp. 1–15, Nov. 2020, doi: 10.3390/met10111495.

[50] X. Zhang, S. Zhao, and M. Wang, "Deep Learning-Based Defects Detection in Keyhole TIG Welding with Enhanced Vision," *Materials*, vol. 17, no. 15, Aug. 2024, doi: 10.3390/ma17153871.

[51] C. Xia, Z. Pan, Z. Fei, S. Zhang, and H. Li, "Vision based defects detection for Keyhole TIG welding using deep learning T with visual explanation," *J Manuf Process*, vol. 56, pp. 845–855, Aug. 2020, doi: 10.1016/j.jmapro.2020.05.033.

[52] Y. Liu, Y. Zhou, S. Wen, and C. Tang, "A strategy on selecting performance metrics for classifier evaluation," *International Journal of Mobile Computing and Multimedia Communications (IJMCMC)*, vol. 6, no. 4, pp. 20–35, 2014.